

Quarterly Report for  
**April - June 2001**  
**Stanford Geothermal Program**  
DE-FG07-99ID13763



## Table of Contents

<b>1. MEASUREMENTS OF STEAM-WATER RELATIVE PERMEABILITY</b>	<b>1</b>
1.1 BACKGROUND	1
1.2 EXPERIMENTAL PROCEDURE	9
1.3 EXPERIMENTAL RESULTS AND DISCUSSION	10
1.4 CONCLUSIONS	23
<b>2. STEAM-WATER CAPILLARY PRESSURE</b>	<b>25</b>
2.1 SUMMARY	25
2.2 INTRODUCTION	25
2.3 THEORY	25
2.4 EXPERIMENTS	26
2.5 RESULTS	28
2.6 CONCLUSIONS	30
<b>3. SCALING OF WATER IMBIBITION DATA</b>	<b>31</b>
3.1 SUMMARY	31
3.2 INTRODUCTION	31
3.3 THEORY	32
3.4 EXPERIMENTS	34
3.5 RESULTS	35
3.6 CONCLUSIONS	37
<b>4. FRACTURED ROCK RELATIVE PERMEABILITY</b>	<b>39</b>
4.1 BACKGROUND	39
4.2 EXPERIMENTAL METHODOLOGY	39
4.3 PARTIAL RESULTS AND DISCUSSION	41
4.4 CONTINUING AND FUTURE WORK	42
<b>5. THE MEASUREMENT OF STEAM-WATER CAPILLARY PRESSURE</b>	<b>45</b>

<b>5.1 BACKGROUND</b>	<b>45</b>
<b>5.2 NEW APPARATUS</b>	<b>46</b>
<b>5.3 PROCEDURES</b>	<b>47</b>
<b>5.4 PARTIAL RESULT AND DISCUSSION</b>	<b>50</b>
<b>5.5 FUTURE WORK</b>	<b>53</b>
<b>6. EXPERIMENTAL INVESTIGATION OF RELATIVE PERMEABILITY IN FRACTURES</b>	<b>55</b>
<b>6.1 THEORETICAL BACKGROUND</b>	<b>55</b>
<b>6.2 LITERATURE REVIEW</b>	<b>57</b>
<b>6.3 EXPERIMENTAL APPARATUS AND MEASUREMENT TECHNIQUES</b>	<b>58</b>
<b>6.4 RESULTS AND DISCUSSION</b>	<b>64</b>
<b>6.5 CONCLUSIONS AND RECOMMENDATIONS</b>	<b>86</b>
<b>7. REFERENCES</b>	<b>89</b>

# **1. MEASUREMENTS OF STEAM-WATER RELATIVE PERMEABILITY**

This research project is being conducted by Research Assistant Peter O'Connor and Professor Roland Horne. The aim is to measure relative permeability relations for steam and water flowing simultaneously in rock and to examine the effects of temperature. The project was completed during the quarter, and a technical report prepared.

## **1.1 BACKGROUND**

Single-phase fluid flow through porous media is normally modeled by Darcy's Law. To apply Darcy's Law to multiphase flow requires the addition of the concept of relative permeability, which accounts for effects on the flow behavior of one fluid or phase caused by the presence of another fluid or phase. Relative permeability is believed to depend primarily on the volume occupied by a phase and so is expressed as a function of saturation. Potentially reducing effective permeability by an order of magnitude in some cases, relative permeability can have a dramatic effect on fluid flow and thus is an important parameter to determine in reservoir engineering. The relative permeability relations involving oil, water, and gas are well known and have been established in laboratory experiments. These curves have been used successfully in flow modeling for petroleum reservoir engineering.

Geothermal reservoirs engineers are necessarily concerned with the flow of steam and water; steam-water relative permeability curves have been difficult to produce due to the inherent phase changes between the fluids and the uncertainty of determining water saturation. A series of experiments conducted by the Stanford Geothermal Program have sought to establish steam-water relative permeability relations; these experiments have maintained near-adiabatic steady-state conditions, determined saturation through X-ray computer tomography, and accounted for slip factor and capillary end effects.

The current work followed on results obtained previously. The objective was to remove any potential effect of temperature on relative permeability by maintaining a constant pressure and temperature gradient for every stage of the experiment. Further, the high pressure gradient should give more reliable and reproducible results with less error than a low pressure gradient. The results were compiled and analyzed by several methods, presenting a comprehensive data set.

Relative permeability describes the effect of one fluid or phase on the flow behavior or another fluid or phase. Fluids interfere with each other by occupying pore volume, limiting connectivity, and causing effects of interfacial tension. These effects can be measured quantitatively and determined by including a relative permeability parameter, which is the permeability to a given fluid of a porous medium partially saturated with another fluid. Relative permeability is expressed as a ratio of this permeability over the medium's measured absolute permeability, and so generally is a number between 0 and 1. Relative permeability is primarily a function of saturation but could also have some dependence on temperature, pressure, or flow rate. For multiphase flow of steam and water the mass flux for each phase is not constant since one phase can be readily

transformed to the other. The current experiment has been designed to minimize phase changes by maintaining adiabatic conditions.

Relative permeability relations for oil, gas, and water have been used extensively in petroleum reservoir engineering, but steam-water curves are not as well established. The curves developed by Corey (1954) for gas-oil relative permeability, and the simpler linear relations (“X-curves”), are the most commonly used forms of relative permeability relations.

The Stanford Geothermal Program has conducted many experiments to determine steam-water relative permeability relations. The experimental procedure has been developed and enhanced over time to ensure greater accuracy and more rigid experimental controls. These experiments have found linear curves in some cases and Corey-type curves in others. Steam relative permeability has been seen to be a more linear function of saturation than is water relative permeability, though the apparent magnitude of this difference has varied.

Single-phase flow in a porous medium is typically governed by Darcy’s law relating the fluid velocity,  $u$ , to the pressure drop,  $\Delta P$ , over the distance,  $\Delta L$ ; the viscosity,  $\mu$ , and; the absolute permeability,  $k$ , of the medium as in Equation 1.1.

$$u = \frac{k \Delta P}{\mu \Delta L} \quad (1.1)$$

In the case of two-phase flow, we introduce the relative permeability  $k_r$  as in Equation 1.2:

$$u = \frac{k_r k \Delta P}{\mu \Delta L} \quad (1.2)$$

To determine permeability from a mass flow rate  $m$ , and considering multiphase flow of steam and water, we use Equation 1.3. The cross-sectional area of the porous medium is  $A$ , and the density of water and steam are  $\rho_w$  and  $\rho_s$ , respectively:

$$m_w = \frac{k_{rw} k A \rho_w \Delta P}{\mu_w \Delta L} \quad (1.3a)$$

$$m_s = \frac{k_{rs} k A \rho_s \Delta P}{\mu_s \Delta L} \quad (1.3b)$$

The total mass flow rate is  $m_t$ , and the steam quality is  $x$ . Then we can rearrange the equations to solve for  $k_{rw}$  and  $k_{rs}$  as follows:

$$k_{rw} = \frac{(1-x)m_t \mu_w \Delta L}{k A \rho_w \Delta P} \quad (1.4a)$$

$$k_{rs} = \frac{x m_t \mu_s \Delta L}{k A \rho_s \Delta P} \quad (1.4b)$$

Saturation, the fraction of pore volume occupied by a given phase, was determined in this experiment by use of X-ray computer tomography (CT). This has made determination of in-situ steam saturation considerably easier than was the case for previous experiments. The CT number is directly related to the density of the material being scanned, with a

higher value indicating a denser composition. Therefore, steam-saturated porous media show a lower CT value than water-saturated porous media.

First, a porosity distribution can be calculated by scanning the rock once when it is dry and again when it is saturated with cold water, determining  $CT_{dry}$  and  $CT_{wet}$ . Using the known values  $CT_{water} = 0$  and  $CT_{air}$  and -1000, we apply Equation 1.5 to determine the porosity distribution:

$$\phi = \frac{CT_{wet} - CT_{dry}}{CT_{water} - CT_{air}} \quad (1.5)$$

Then, we establish reference values of the CT values along the core for complete steam saturation and for complete hot water saturation. From this point, at any later measurement where we have a CT value for two-phase flow, it is a simple interpolation to determine the exact saturation, by Equation 1.6. Note that it is important to use the CT value for hot water rather than that for cold water, since there is a density change between the two. In this case, the initial imbibition step involved flowing superheated steam into an evacuated core. This served as the first flow test as well as fixing the steam saturation values.

$$S_{st} = \frac{CT_{hw} - CT_{meas}}{CT_{hw} - CT_{steam}} \quad (1.6a)$$

$$S_w = 1 - S_{st} \quad (1.6b)$$

Gases flowing under pressure experience a higher effective permeability than liquids do; the permeability of a porous medium measured by flowing single phase gas varies with the average pressure in the medium. This effect is known as Klinkenberg effect, and it is accounted for by correcting gas relative permeability with a slip factor. The correction is shown in Equation 1.7, where  $b$  is a value of 6.58 psia as determined by Li and Horne (1999).

$$k_{rs(corrected)} = \frac{k_{rs}}{(1 + b/p_m)} \quad (1.7)$$

As mentioned, relative permeability experiments at Stanford have been progressing for several years with successive improvements to the apparatus and procedure. The effectiveness of the experimental procedure was greatly increased with the employment of a CT scanner to determine steam saturation (Clossman and Vinegar, 1988). The recent experiments most carefully considered were those of Ambusso (1996), Satik (1998), and Mahiya (1999). Each experiment introduced new controls and mechanisms to ensure optimal experimental conditions and accuracy. Ambusso (1996) employed real-time measurement of temperature and pressure to determine the status of the core at several points along the core. Ambusso conducted his experiments at a range of temperature and pressure gradients. Temperature at the first core thermocouple ranged from 101 °C to 117 °C. The fluid was injected in two-phase flow by heating it under pressure and then flowing it through a throttle valve. Ambusso (1996) determined an X-curve relationship between relative permeability and saturation. Experiments by Satik (1998) changed the inlet mechanism, adding separate inlets for steam and for water. Mobile steam quality was calculated on the basis of separate inlet fluid flows and measured heat flux out of the

core. A new core was prepared, with a core holder of high-temperature plastic. Satik's results indicated a Corey-type curve relationship for steam-water relative permeability, with a steam residual saturation of less than 10% and a water residual saturation of 30%. A subsequent experiment by Mahiya (1999) solved the problem of phase changes with the addition of a flexible heat guard. This maintained adiabatic conditions throughout the experiment. Mahiya's experiment relied on a combination of separate inlets and enthalpy calculations to determine the steam quality. Generally, mobile saturation during the imbibition steps could be determined by maintaining single-phase flow from each inlet, while some of the high-water-saturation drainage steps required mixed flow from each inlet with the actual mobile saturation estimated from enthalpy. Mahiya's results generally agreed with Satik's, though the steam relative permeability values were slightly higher and the intersection of steam and water relative permeability was at  $S_w = .65$  rather than  $S_w = .55$ . Mahiya also concluded that there was a Corey-type relationship.

The experimental design used in this experiment built on the advances in procedure and apparatus developed in the previous experiments. The experiment determined the steam-water relative permeability for a Berea sandstone core. This was the same core used in experiments by Satik (1998), Mahiya (1999), and Belen (1999). The core had the following properties: length 43 cm, diameter 5.04 cm, measured porosity 24%, and permeability 1200 md. Clays in the core were deactivated in previous experiments by baking it at 800 °C, and the core was cemented with epoxy to a core holder of high-temperature plastic.

Pressure ports were drilled through the core holder at fixed intervals; heat-resistant plastic tubing ran from these ports to a pressure transducer box. At these ports, as well as the inlets and outlets, the pressure tubings were fitted with T-type thermocouples. There were eight pressure and temperature measurements along the core, two at the inlets, and one at the outlet. A flexible heat guard, described later, was wrapped around the core holder. A heat flux sensor was fixed under every section of the heat guard, sending both heat flux and temperature data to the system. As these sensors were outside the core holder, they did not register the interior core temperature as accurately as did the thermocouples at the pressure ports. The whole core was wrapped with insulating fiber on top of the heat guard to further minimize heat loss. A schematic of the apparatus is shown in Figure 1.1, and a photograph is shown in Figure 1.2.

The outlet end piece was plastic, fitted with a pressure port and thermocouple. The inlet end piece was stainless steel, fitted with two pressure ports and thermocouples, one for the steam inlet and one for the hot water inlet. A thermal switch was installed within the end piece to deactivate the furnaces in the event the end piece temperature exceeded 170 °C. This was added to prevent damage to the core in the event of interruption of water flow to the heaters, as had happened in previous experimental attempts.

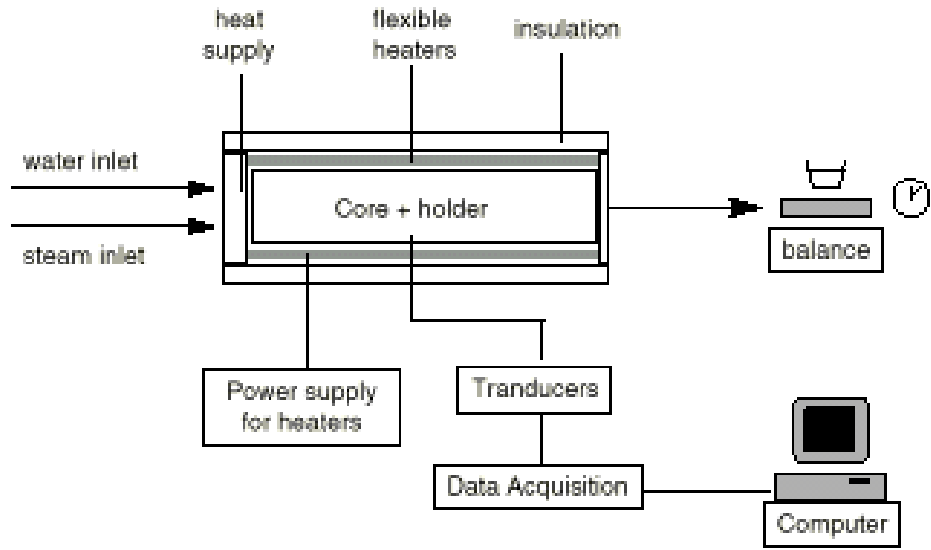


Figure 1.1: Experimental design schematic.

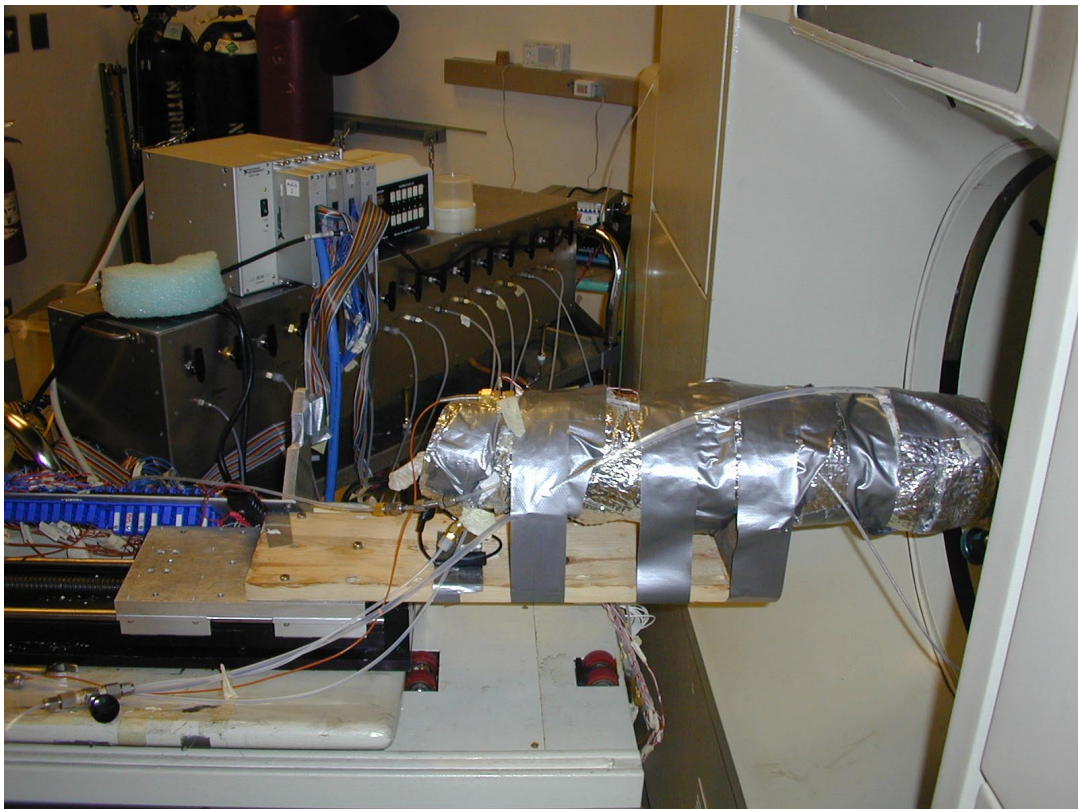


Figure 1.2: Core assembly mounted on CT scanner couch. Pressure transducer box and SCXI modules and chassis box seen in background.

Deionized distilled water was sent to a boiler, where it was deaerated. The boiling water was then pumped through a cooling tank to enable it to pass through the displacement pump and into the inlet end piece. Two resistance heaters heated the water either to liquid just below the saturation temperature or to vapor just above the saturation temperature, and the fluids then entered the core and mixed. A tube ran from the outlet to a collecting flask on a scale, where the outlet mass flow rate could be measured and compared to the inlet mass flow rate to determine if the system was at steady state.

We recorded pressures, temperatures, and heat fluxes with a data acquisition system designed for previous experiments. This system utilized several National Instruments devices to process a considerable amount of data simultaneously and display it in an easily readable format on a PC. Signals from the transducers, thermocouples, and heat flux sensors were sent through a patch board to SCXI-1100 modules, and these modules were installed in a SCXI-1000 chassis box. The chassis box sent the data to a PC, where the data was displayed. The PC ran the National Instruments program LABVIEW version 4.1, a graphical programming utility for instrumentation. LABVIEW provided a means of monitoring heat flux, temperature, and pressure simultaneously, as well as controlling the flexible heaters. LABVIEW did not monitor the flow rates or furnace settings directly, but these could be entered manually so that they would be saved with the pertinent data. We reconfigured previous LABVIEW routines to suit the needs of this experiment.

A flexible heat guard consisting of 18 independent heating elements was wrapped around the core. A schematic is shown in Figure 1.3. The flexible heaters were connected through a step-down transformer to a variable output power supply. A LABVIEW routine was redesigned to activate the heater units as necessary to maintain a constant heat flux of near zero. To control the individual heaters, we used National Instruments' SCXI 1163-R module, consisting of 32-channel optically isolated digital output/solid-state relays. In the closed state, each relay had a maximum resistance of 8 ohms and carried up to 200 mA of current. A LABVIEW algorithm was constructed to monitor the heat flux and adjust the heaters as necessary to maintain adiabatic conditions. As the relays are not variable voltage controllers but simple on/off switches, the necessary heat flux was generated by setting a duty cycle to each relay, and thus to each heater. A duty cycle of 0% corresponded to relay being closed and the heater operating all the time, while a duty cycle of 100% corresponded to the relay remaining open and the heater being inactive. A cycle in between would open the relay a percentage of the time equal to the duty cycle during each period. The heaters were generally set to a cycle period of 2-3 seconds, and the ideal power setting was to have most of the duty cycles near 50%.

The control protocol checked the heat flux every minute. If the heat flux for a specific heater was outside the tolerance range, usually  $30 \text{ W/m}^2$ , the program would increase or decrease the duty cycle accordingly by a given increment, typically 5%. Due to PC speed and memory constraints, this protocol often failed to work properly when the graphical displays were active. For this reason, the control protocol was allowed to establish the correct heater settings for adiabatic conditions, then the duty cycle increment was set to 0% and the graphical displays were activated. If the heat flux averages left the tolerance range, the control protocol would be reengaged to adjust as needed. In some cases, when

specific heat flux sensors failed to function adequately, the duty cycle of a given heater would be set manually to equal that of the heaters on either side and preventing from adjusting independently.

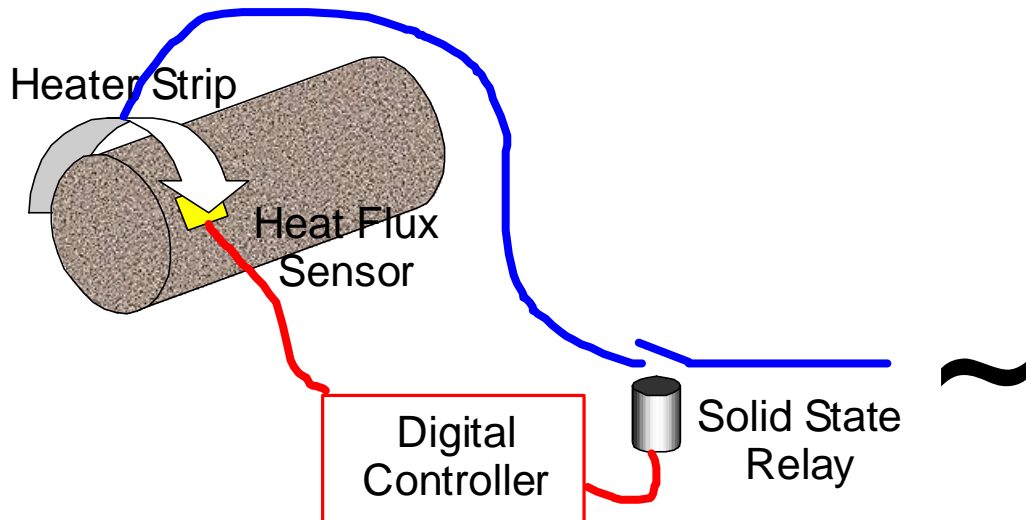


Figure 1.3: Flexible heat guard design.

A modified medical X-ray CT scanner was employed to determine the water saturation at all points along the core. In-situ saturation values were calculated from images generated by the Picker Synerview 1200X X-ray CT scanner. The core assembly was mounted and secured on a couch, which could be controlled by the console on the scanner. The scanner was equipped with a visible laser and a digital display of the couch position. We therefore could establish accuracy of the measurement by ensuring that each scan was at the same relative position along the core for each experiment.

The scanner had been augmented and modified to fit the needs of petroleum and geothermal reservoir engineering experiments, in particular with the addition of a large range of variable power settings. This experiment required setting the scanner at 125 kV, 65 mA, an exposure time of 8.49 seconds per slice, and a slice thickness of 10 millimeters. The large slice thickness of the CT scans reduced any potential errors caused by inaccuracy in the couch positioning system.

This experiment provided insight into potential future improvements to the experimental procedure and apparatus. The data acquisition system is exceptionally useful and should become even more powerful and adaptable with newer versions of LABVIEW. We suggest employing a faster PC to take full advantage of LABVIEW's capabilities. The CT scanner is accurate and provides a clear picture of the interior of the core. The flexible heat guard greatly enhances the effectiveness of the experiment by negating the need for heat loss estimations.

The core holder itself could be improved, in particular the inlet end piece. The stainless steel end piece is resistant to thermal damage and permits the addition of a thermal switch to prevent damage to the core. However, this particular device creates difficulties in controlling the steam and water inlets. Excess heat from the steam furnace heats the inlet water, to the extent that it was often not needed to supply any heat at all to the water furnace in order to have water at the saturation temperature. Maintaining superheated steam and liquid water at the two inlets was difficult. At times, the hot water temperature appeared to exceed the saturation temperature, despite the fact that there was not enough power going into the core to heat the given flow rate to superheated conditions. This may have been a consequence of steam pockets forming in the water furnace at the location of the thermocouple, or asymmetrical water flow around the furnace. In all of these cases, the temperature at the first pressure port was at the saturation temperature, even if both steam and water inlets had appeared to be injecting superheated steam. Therefore, it is not considered that injection through the water inlet was actually superheated steam in these cases.

The steel end piece also at times heated the water at the first pressure port to a higher temperature than the water in the inlet. This would be the case when the energy produced by the heaters could not be entirely transferred to the injected fluids as they passed through the end piece. This effect is visible in a couple of the temperature profiles in Section 5, though it was often a problem that had to be fixed during the experiment. If, as a consequence of heat transfer between the furnaces, there was more steam entering the core than was entering solely through the steam inlet, we would have underestimated the steam relative permeability in some cases.

A future end piece should retain the stainless steel construction, but should have a greater separation between the steam furnace and the water furnace. A gap cut down the length of the endpiece, filled with insulation or left open to the air, would greatly reduce heat transfer between the steam heater and the water heater. A thermal switch should be installed in the steam heater side of the inlet, since it will be necessary to deactivate the heaters in the event of interruption of water supply. Two other methods might allay the problem of heat transfer between the heaters. Preheating the steam would reduce the power necessary for the steam furnace, as would the use of external furnaces. The internal furnaces minimize atmospheric heat loss, an advantage that we may not wish to dispense with.

The displacement pumps used in this experiment were accurate, but not very reliable. In one case, loss of fluid flow resulted in damage to the core and warranted the installation of the thermal switch. After that modification, there were several other flow decreases that caused temperature spikes and triggered the thermal switch. We suggest replacement of the displacement pumps.

If the experiment is to be repeated at a different pressure gradient, additional modifications would be necessary. The current core holder is probably not suitable for temperature and pressure gradients significantly higher than those used in this

experiment. A titanium core holder might be an effective option if its cost is not prohibitive.

## **1.2 EXPERIMENTAL PROCEDURE**

This section describes the steps taken in the experiment, conceptual goals, and challenges encountered. The experimental procedure closely followed the procedure established by Mahiya (1999), though certain changes were made to enhance the effectiveness of the experiment.

The water supply was set up as detailed in Section 1.1. The boiler had to be refilled periodically with water and allowed to boil for a length of time sufficient to deaerate the water. Once the water was deaerated and the boiler was full and turned off, the system could generally be allowed to run overnight or for several hours during the day to establish steady-state conditions. This was not the case for experiments at high mass flow rate. Outlet water was collected occasionally and weighed on a scale to compare the outlet mass flow rate to the injection mass flow rate, to verify steady-state conditions and to confirm the accuracy of the pump flow rates.

The experiment began with an imbibition process. Performing the imbibition process first allowed determination of the maximum necessary steam flow and correspondingly the maximum necessary power input. The initial step was a flow of superheated steam into an evacuated core; as the CT values for this step were actually slightly lower than those found for the evacuated core, this was used as the baseline for calibration of the CT values. Therefore, the steam saturation in this step was taken to be 100%, as the temperature at all points along the core was considerably higher than the saturation temperatures. Fluid injection continued, with an increasing water mass fraction in each successive step of the experiment. We attempted to control temperature sufficiently that there was obviously single-phase flow from each inlet. At each step, after the system had reached steady-state conditions, a CT scan of the core was taken. The images were processed on the Picker console, transferred to a magnetic tape drive, and then saved to a PC.

Once the imbibition step was complete, the drainage process began. During this process, only one inlet pump was available and two-phase fluid was injected at saturated conditions. Mobile steam quality was calculated as detailed later. The drainage experiments took place over a range of high and moderate water saturations. Unfortunately, it was not possible to further investigate the region of low water saturation.

In this experiment, we attempted to maintain a constant pressure gradient of 0.89 psi/inch (a 15 psi pressure drop over a 43 cm core) to avoid any effects of temperature on relative permeability. The outlet was at atmospheric pressure, and an inlet pressure of 15 psig corresponded to a saturation temperature of 120 °C. Constant pressure gradient was to be maintained by varying the flow rate as needed. Total mass flow rate ranged from 2 g/min to 16 g/min for all of the steps at the target pressure gradient.

Certain modifications to the experiment were necessitated by limitations of the apparatus. During the drainage step, hot water was to be injected through one inlet and steam through another, as had been done in the imbibition step. However, in this stage of the experiment we sought to produce very small steam flow rates, to further examine the area of high water saturation. For the flow rates considered, it proved to be impossible to heat fluid in the steam inlet to superheated conditions without considerable transfer of excess heat to the core and to the hot water inlet. It proved easier to produce miniscule amounts of steam by heating the inlet water to the saturation temperature. Later in the drainage step, it would have been possible to return to a dual-inlet setup, but the other displacement pump had begun to fail, possibly due to a leaking seal.

The original inlet thermocouples failed and were replaced before the drainage step, but the replacement thermocouples were less accurate due to difficulties in positioning them precisely enough. They routinely read temperatures too high (if the thermocouple was positioned near the heater) or too low (if it was further back along the pressure tubing). In the drainage step, the temperature at the first pressure port was used to determine if the flowing fluid was at saturated conditions. While it would be better to know the actual inlet temperature, it was not crucial, as we did not have separate inlets of superheated steam and liquid water.

Certain of the drainage steps may not have reached steady-state flow. Due to the large volume of water involved, they could only be left unattended for 2-3 hours at most before the boiler would need to be refilled; as a consequence, they could not stabilize overnight. In these cases, they were monitored and as much time as possible was allowed for the system to stabilize. This most likely accounts for the saturation front seen in some of the drainage experiments.

### **1.3 EXPERIMENTAL RESULTS AND DISCUSSION**

A total of 28 steady-state experiments were performed over a period of several weeks. The resulting data covered the full range of saturations, with particularly large amounts of data for regions of moderate saturation. Fifteen imbibition experiments were performed, followed by 13 drainage experiments. The drainage experiments had greater success in covering the range of high water saturations but suffered from loss of accuracy in determining the flowing steam saturation. Near-adiabatic conditions were maintained for all experiments. Other than an initial flow of 100% steam into an evacuated core, the maximum steam saturation reached was about 65%. The maximum water saturation reached was 100%, due to condensation of immobile steam during the earliest drainage step.

Saturation profiles during the imbibition step, shown in Figure 1.4a, were constant across the core and cover the range of steam saturation from 30% to 65%. These tests did not cover a range of high-water or high-steam saturations. The saturation profiles in the drainage step, shown in Figure 1.4b, exhibit greater variation across the core, but also covered a wider range of saturations. The existence of a saturation front and multiple flat

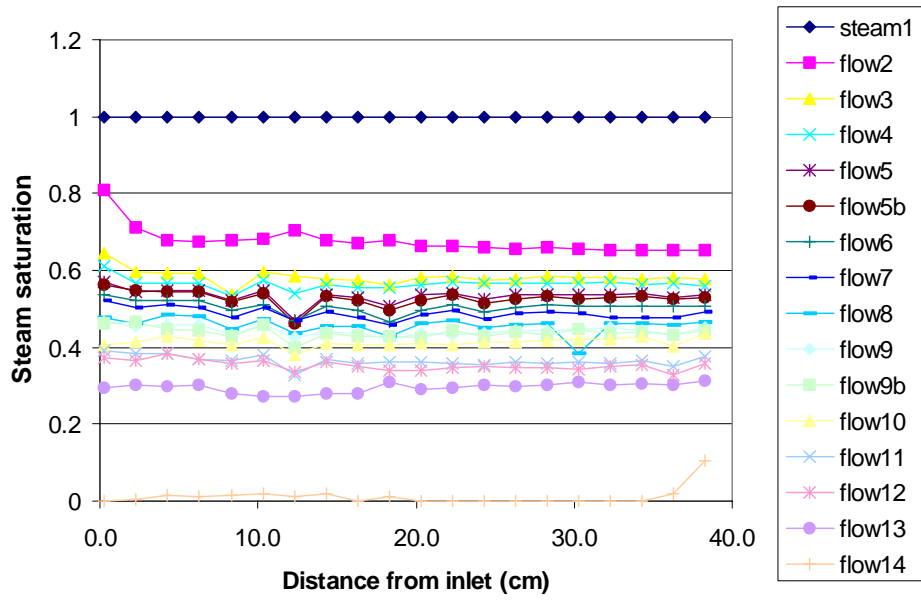
saturation regions allowed these experiments to provide useful data. The presence of fronts in the drainage phase may be the result of unsteady-state conditions, or it may be the result of the steam in the latter part of the core being more difficult to displace. In results presented later in this chapter, one relative permeability graph is presented using the average saturation from the first half of the core, which showed stable saturation at all points. Capillary end effect was visible in many of the steps. For this reason, one relative permeability graph is presented excluding the pressure ports nearest to the inlet and outlet.

For the drainage steps, only one inlet could be used. This was generally acceptable for determining the liquid flow rate when the total mass flow rate was large, as it was in most of the drainage steps. It was necessary to determine the steam flow rate for these experiments and both flow rates for the low mass flow rate drainage experiments. Analyzing previous flow tests from this experiment, and considering other experiments, we derived a reasonable correlation between inlet steam quality and in-place saturation. It appears that large amounts of inlet water can displace even “immobile” steam saturation, though this may be a factor of a phase change too minor to be prevented by the heat guard. These correlations are shown in Figures 1.5a and 1.5b. A relationship was derived and applied to the data, estimating the inlet and mobile steam quality from the mean saturation. Equation 1.8a was used for high steam saturation, ( $S_{st} > .20$ ) and Equation 1.8b was used for lower steam saturation. In this manner, steam inlet quality was calculated for the drainage steps. We present this method with some reservations, but consider the uncertainty in steam flow rate to be moderate and the uncertainty in water flow rate to be extremely minor. As an example, underestimating a steam quality of 6% as being 3%, a 50% error, would only result in overestimating the water mass flow rate by 3.2%. In most cases, the estimated steam quality was considerably less than 1%.

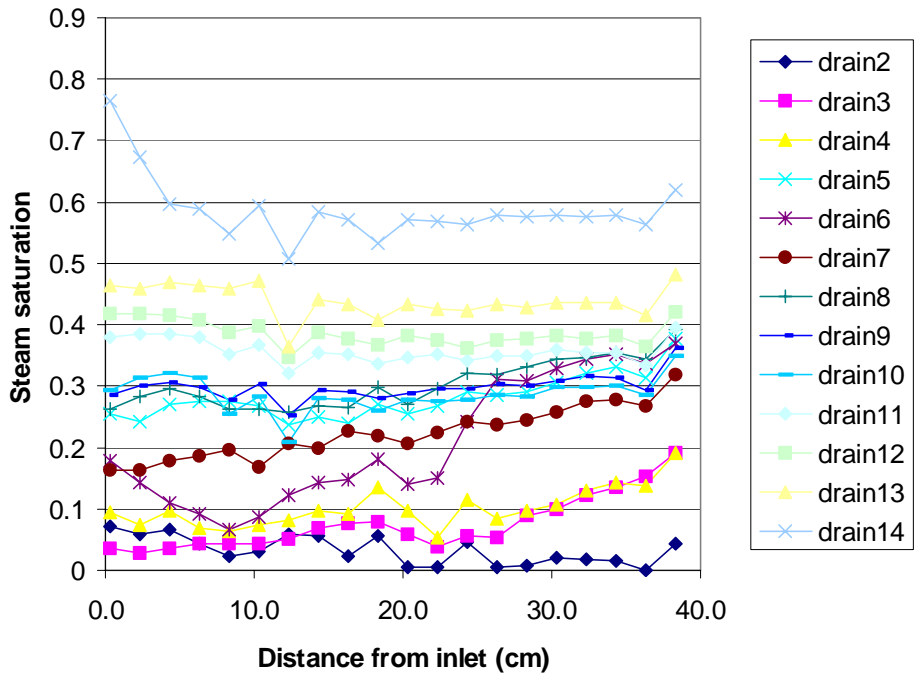
$$x = \frac{S_{st} - 0.3886}{0.2462} \quad (1.8a)$$

$$x = e^{\frac{S_{st} - 0.5225}{0.0415}} \quad (1.8b)$$

The goal of this experiment was to maintain a constant pressure drop of 15 psi by varying the flow rate as needed. This was successfully accomplished throughout the entire imbibition phase, save for the 100% water inlet step at the end. The constant pressure gradient could not be maintained in a few cases of high water flow, such as the end of the imbibition phase and the first few trials of the drainage phase. In these cases, the pump and heater could not supply sufficient water at 120 °C to maintain a 15-psi pressure drop across the core. For attempts to increase the flow rate further, the main limitation appeared to be the rate of heat transfer from the water heater to the fluid flowing over it. The water being injected remained considerably below the saturation temperature, yet the temperature at the first pressure port was higher than that measured for the hot water inlet. This indicated that the heater was not transferring all of its heat to the fluid, and that the excess was transferred directly to the core, which could result in damage to the core. Pressure profiles are shown in Figure 1.6a and Figure 1.6b. Note that the pressure drop is very close to 15 psi for most of the drainage steps and all but one of the imbibition steps.

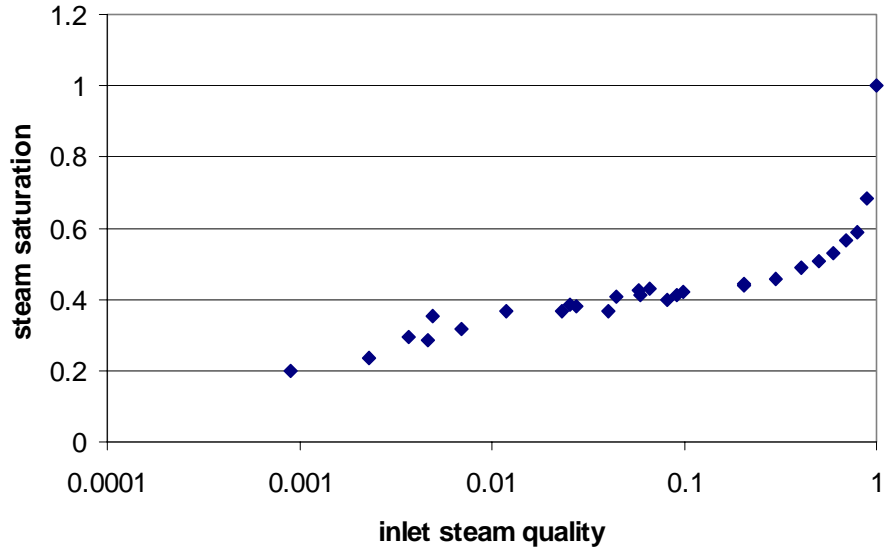


(a) Imbibition

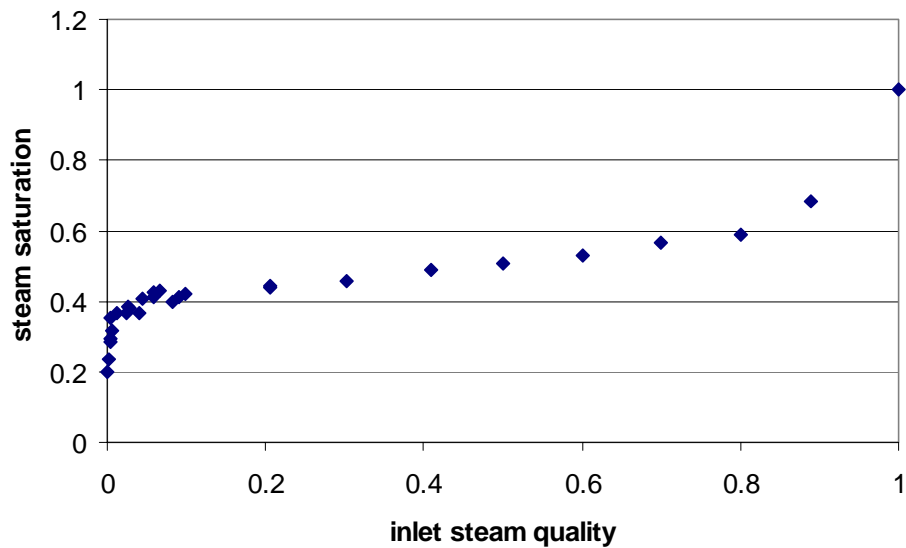


(b) Drainage

Figure 1.4: Saturation profiles.



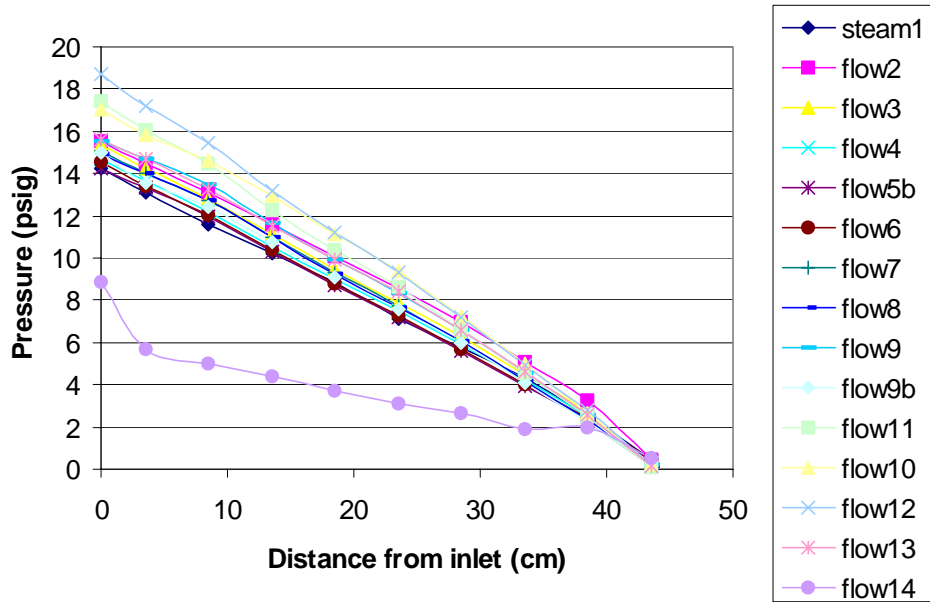
(a) Logarithmic plot



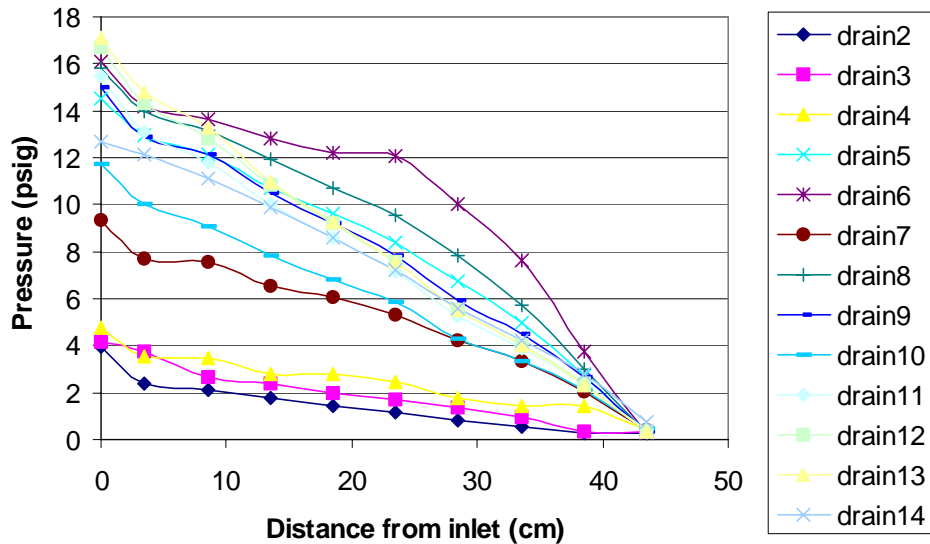
(b) Linear plot

Figure 1.5: Correlation of saturation with inlet quality.

A second reason to maintain the 15 psi pressure drop is that it appears the transducers are most reliable in that range. Flow tests at lower pressure seem more likely to have minor anomalies, which resulted in relative permeability either inflating or becoming negative. This may simply be a consequence of absolute errors and fluctuations in the pressure readings, which produce a greater relative effect at low pressure. For this reason, the flow tests with lowest pressure gradients are excluded from most presentations of the relative permeability data.



(a) Imbibition

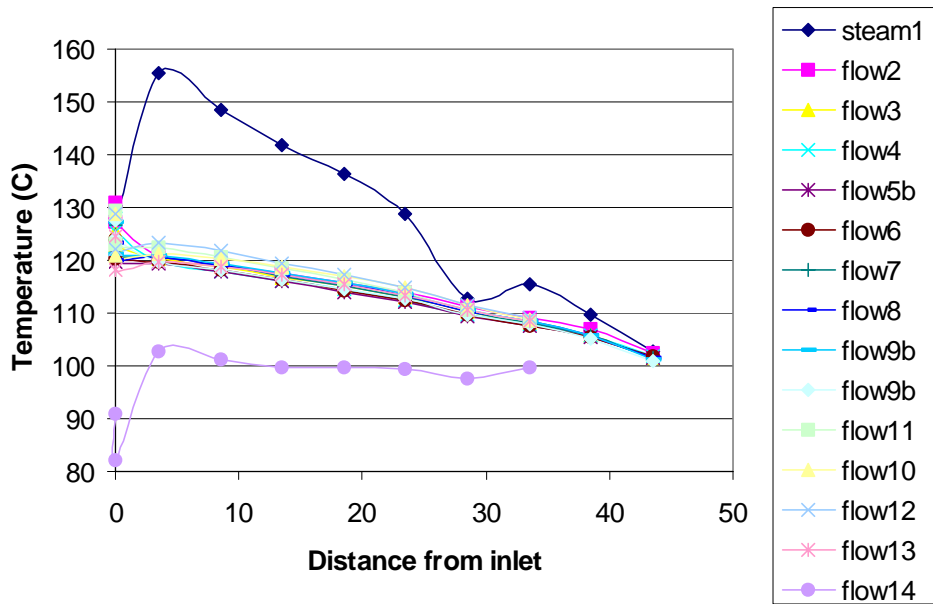


(b) Drainage

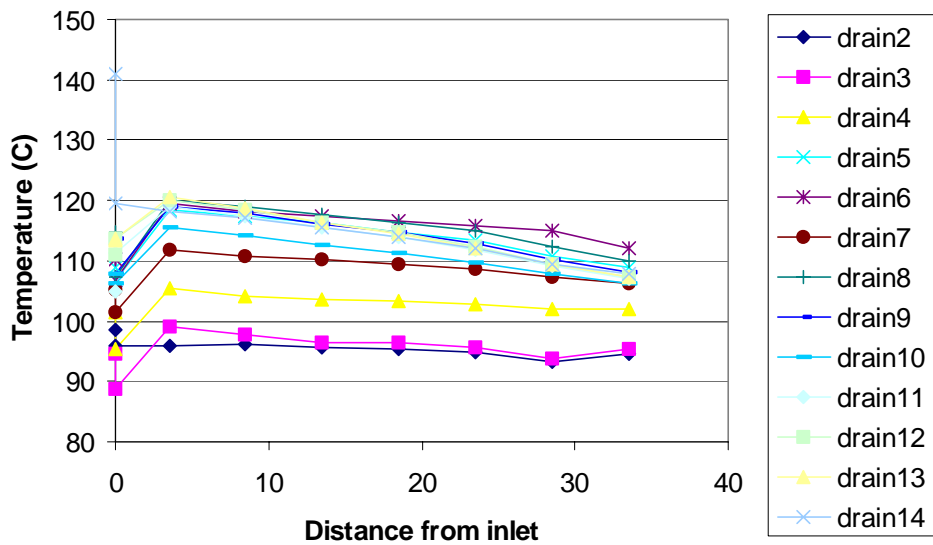
Figure 1.6: Pressure profiles.

The core temperatures generally matched the saturation temperatures at the measured pressures. Slight deviations due to instrument inaccuracy and fluctuation existed, so we took 1 psi to be an acceptable margin of error between the measured temperature and the saturation temperature. Anything outside of that range was considered superheated or unsaturated. Some steps, such as the steam imbibition phase, exhibited a higher temperature at the first pressure port than at the inlet. This was regarded as a consequence of inadequate heat transfer away from the steam heater, with the result being

that the heater was radiating excess heat through the end piece and into the core. This was generally not a desirable condition. Temperature profiles are shown in Figure 1.7a and Figure 1.7b. Note that for much of the drainage phase the thermocouples near the end of the core were not functional. The more reliable thermocouples from the end of the core had been moved to replace malfunctioning thermocouples at the inlets, as controlling the inlet temperature as precisely as possible was of greater importance than monitoring the outlet temperature.



(a) Imbibition



(b) Drainage

Figure 1.7: Temperature profiles.

The average heat flux was kept within 30 W/m<sup>2</sup> of a target heat flux of 0 W/m<sup>2</sup> throughout each experiment. As the individual heaters cycled on and off, the instantaneous heat flux at any given sensor at a specific time may have been between 80 and -80 W/m<sup>2</sup>. The instantaneous heat flux data was recorded but is not an effective measure of the actual heat flux and so is not included here. Two heat flux sensors were highly erratic, so the heaters for these strips were set to the duty cycles of adjacent heaters. A recurring concern throughout the experiment was heat flux through the stainless steel inlet end piece. This prevented the calculation of inlet enthalpy based on power supplied to the furnaces, which would have otherwise been a useful method to estimate inlet steam quality.

Results for relative permeability appear to be Corey-type curves for water and possibly a more linear relationship for steam. Maximum steam saturation appears to be around 70%, and maximum water saturation appears to be 90%. When considering the flow trials not occurring at the target pressure gradient, there are indications that  $k_{rw}$  may be as high as 0.65 or even higher. These less-reliable trials comprise nearly all of the cases with water saturation greater than 0.8, so it might not be appropriate to discard them entirely.

In all figures other than Figure 1.10 (the harmonic averages), the data from the first pressure port and the outlet are excluded. Each stage of the experiment showed a considerable disparity between the data from these ports and the data determined elsewhere along the core. This was most likely due to capillary end effect or unusual pressure behavior involving the placement of the inlet and outlet pressure tubings. The data are presented as follows:

Figures 1.8a and 1.8b show the relative permeability curves for all data points other than the first pressure port and the outlet. Note that a few data points indicated permeabilities significantly greater than 1 or less than 0 even after correcting for the slip factor; these were attributed to instrumentation anomalies and were ignored. Figure 1.8b focuses on the data near the area of low permeability around  $S_w = 0.64$ . In this view, we see that the imbibition steps show scattered clusters of the  $k_{rs}$  data, rather than any significant trend.

Figures 1.9a and 1.9b show the relative permeability for all points in the interior of the core (pressure ports 2-7) and the points from flow tests with a gradient less than 12 psi. This shows a maximum water saturation of 0.92, a maximum steam saturation of 0.69, and increasing scatter in  $k_{rw}$  as  $S_w$  increases.

Figures 1.10a and 1.10b show the mean relative permeabilities across the core for each step; Figure 1.10a shows the mean values from all steps, while Figure 1.10b excludes the runs which did not occur with a pressure drop near 15 psi.

Figures 1.11a and 1.11b show the relative permeability calculated at the data points 2-5, which had uniform saturation in each flow test and were generally free from anomalous pressure readings resulting in inflated or negative relative permeability. Figure 1.11a shows all the data, and Figure 1.11b shows the averaged values for each flow test. These

graphs exclude the flow tests of high water saturation that had a pressure drop of less than 12 psi. The corrections show some improvement in the scatter for the graph of all data points, but no real change from the harmonic means of the entire core.

Note that there are considerably more data points than there are steady-state experiments; each experiment allowed determination of relative permeability across every interval between pressure ports. In addition, some experiments had pressure and temperature data recorded several times during the 30-minute scanning interval, resulting in multiple relative permeability values for a single flow test if there was variation in the transducers or thermocouples.

It is our conclusion that the data from the harmonic means (Figure 1.10a) are the most reliable and the best representation of the total data gathered. It then appears that while water relative permeability follows a Corey-type curve similar to that found in previous experiments, steam relative permeability follows a steeper and more linear trend. This conclusion does not change when different sections of the data are considered. The steam relative permeability deviates from a Corey curve in several regions, and not simply for the drainage data points involving a mobile steam quality calculated through correlations. It may be that steam relative permeability follows a truly different relation, or it may be that there was some systematic error in the calculation of steam flow rates. If, for example, the inlet heaters were heating the end piece enough that water was turned to steam after it passed the inlet thermocouples and entered the core, the result would be underestimated inlet steam quality. This bears further investigation with particular focus on the region of water saturation between 50% and 75%.

From the graphs, residual water saturation appears to be around 30%, and residual steam saturation appears to be around 10%. Residual steam saturation is hard to determine since the drainage tests began with an initial water saturation of about 100%.

The data points from the low-pressure stages are not consistent with the rest of the data. This may be due to an actual effect of pressure on relative permeability, but it is more likely due to two other factors. The low-pressure flow tests are also the flow tests with highest water saturation, and low pressure gradients are more significantly disturbed by fluctuations and inaccuracies in the pressure transducers.

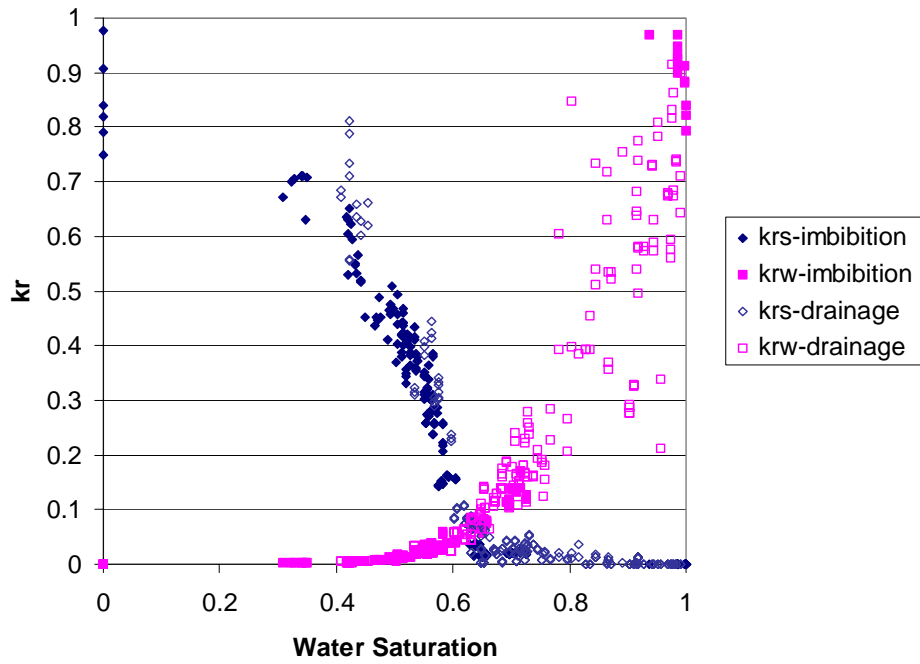
The values for mean relative permeability across the core were calculated by taking the harmonic average of the relative permeabilities for all points along the core, then plotting against the mean saturation across the core. This accounted for the varying viscosity and density, whereas averaging the temperature and viscosity and calculating relative permeability based on the overall pressure drop would not have done so. The data was originally calculated considering all data points, then considering only the interior data points (ignoring the data points closest to the inlet and outlet). There was no noticeable difference in the appearance of the averaged data; while the capillary end effect may create anomalous outlying points on a graph of all data, these points will not significantly

alter the average of the data. In Figure 1.11b, the same method was used, but only the values for saturation and relative permeability between ports 2 and 5 were considered.

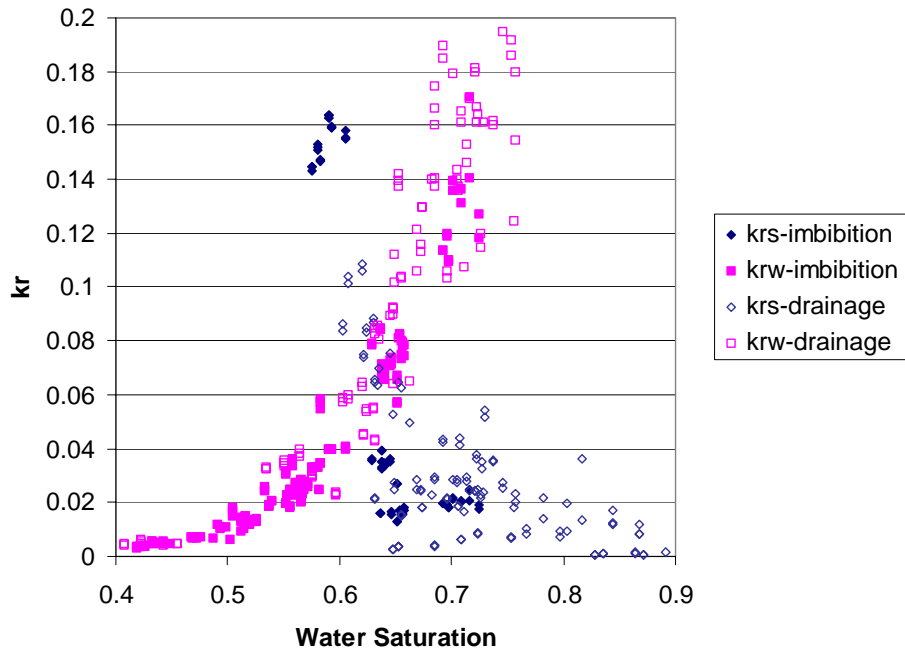
Averaging the saturation across the core does not account for the flow tests in which the saturation varied across the half of the core nearest the outlet, as was the case for approximately half of the drainage tests. This problem was to be eliminated by only considering ports 2 through 5. However, even when the whole core was considered and averaged, the points from these tests did not diverge from the data trends, as the relationship between relative permeability and saturation is nearly linear over the relatively small range of saturation seen in those tests.

Data were also compiled for the relative permeability as measured at each individual pressure port. The shapes of the relative permeability graph were similar throughout, though each pressure port had different endpoints. The lack of high water saturation values in the latter part of the core limited the data available in those sections, and the graphs overall did not reveal any abnormalities in any of the interior pressure ports.

Figure 1.12 shows the results of this experiment (the harmonic average data presented in Figure 1.10a) compared with previous results obtained by Satik (1998) and Mahiya (1999). The general trend of the data is similar in shape. Data from this experiment agrees more with the Mahiya data in fixing the point of intersection of steam and water relative permeability at  $S_w = 0.65$ , rather than the 0.55 determined by Satik. Relative permeabilities were, overall, lower for water flow and higher for steam flow than in the previous experiments.

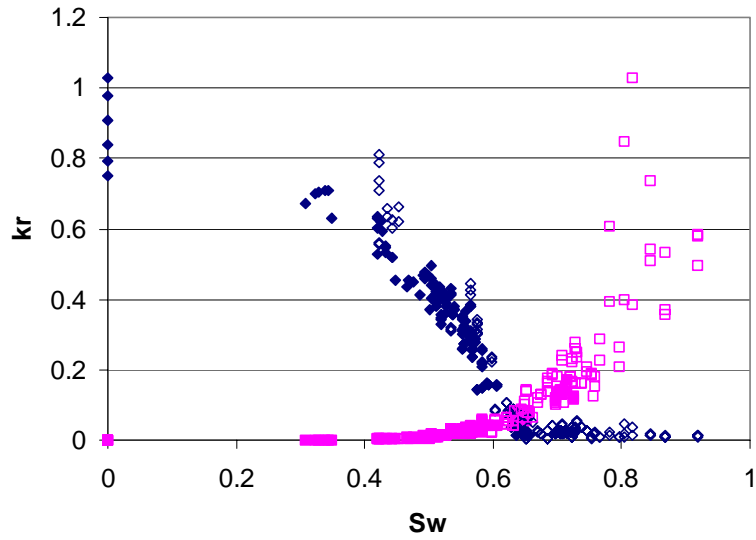


(a) All data

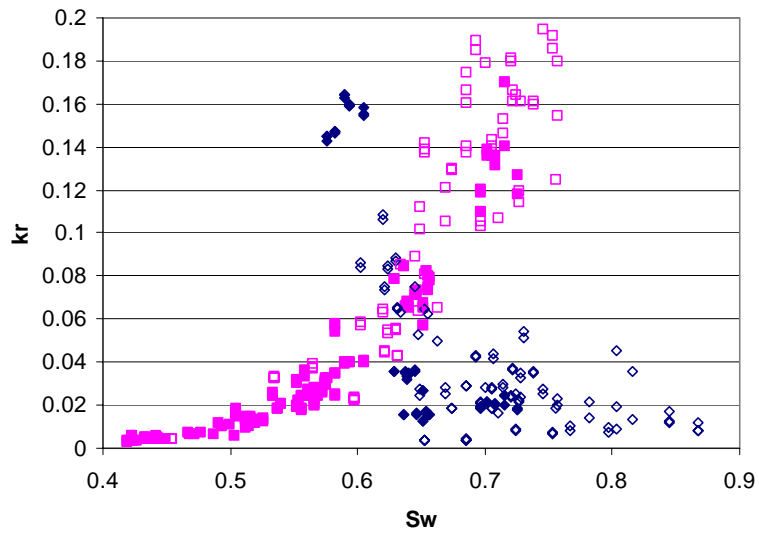


(b) Close-up of area of intersection

Figure 1.8: All data points.

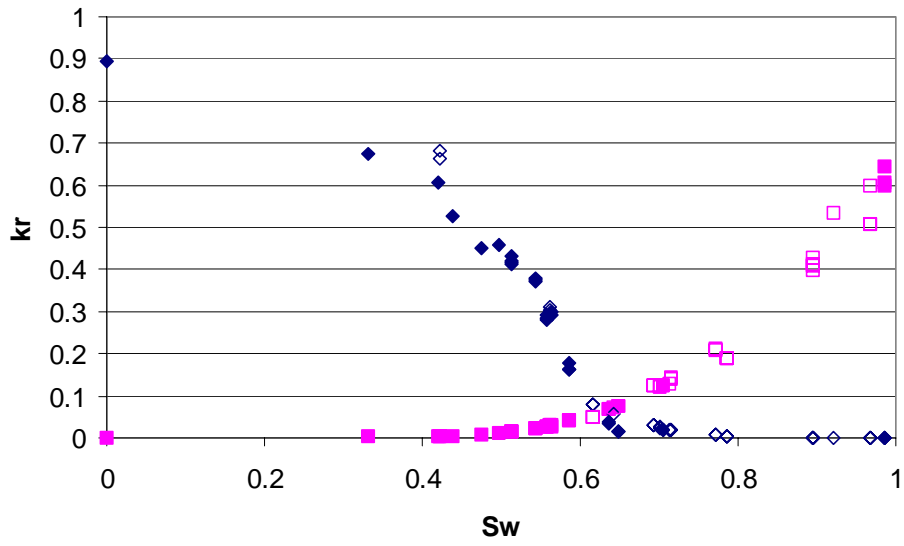


(a) All data

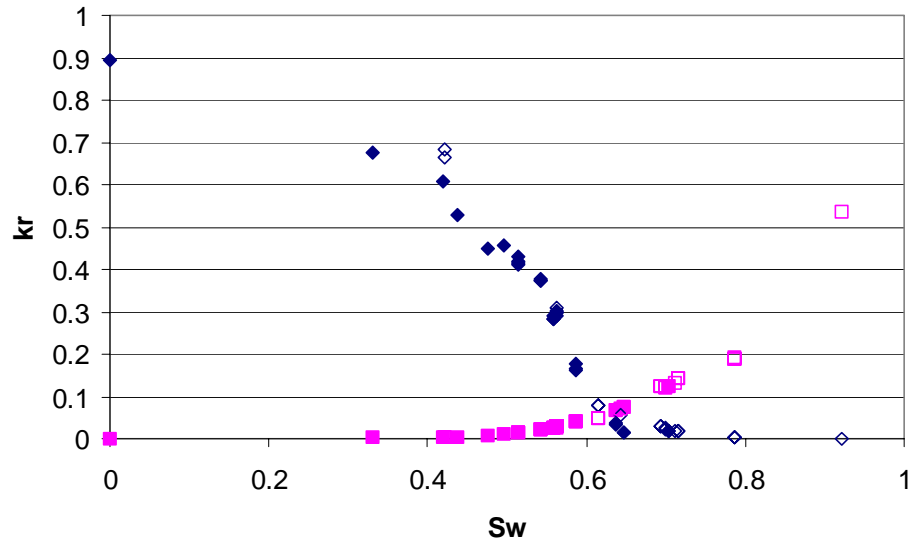


(b) Close-up of area of intersection

Figure 1.9: Interior data points, 15 psi pressure drop. Legend as in Figure 1.8.

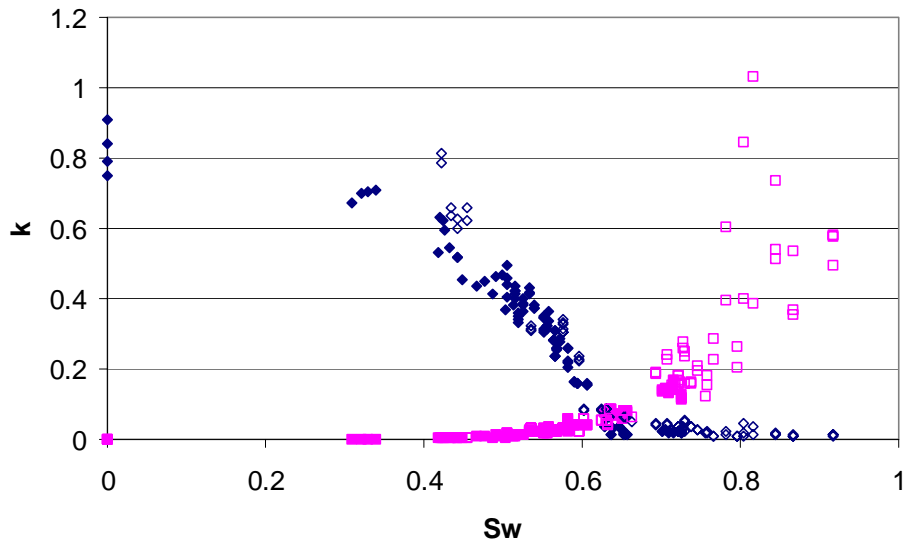


(a) All flow tests

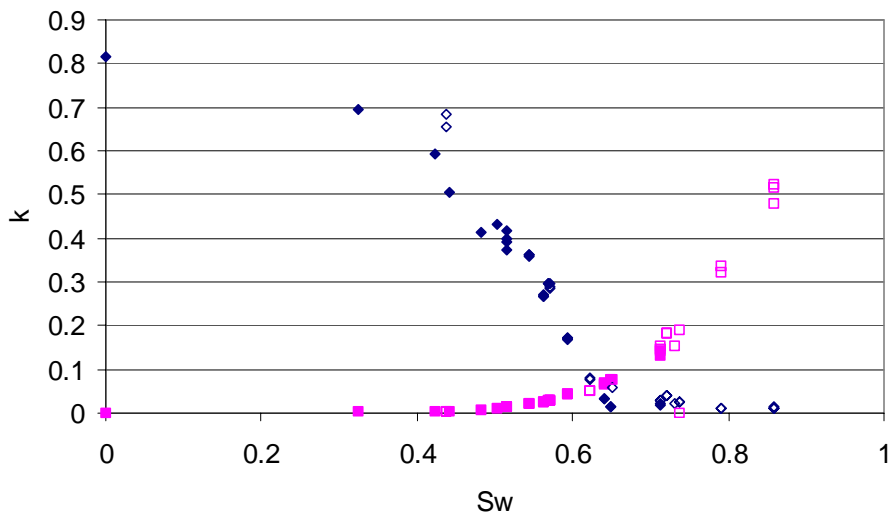


(b) Constant pressure flow tests

Figure 1.10: Harmonic means. Legend as in Figure 1.8.



(a) Ports 2-5



(b) Average of ports 2-5

Figure 1.11: Experiments conducted at constant saturation and  $\sim 15$  psi pressure drop. Legend as in Figure 1.8.

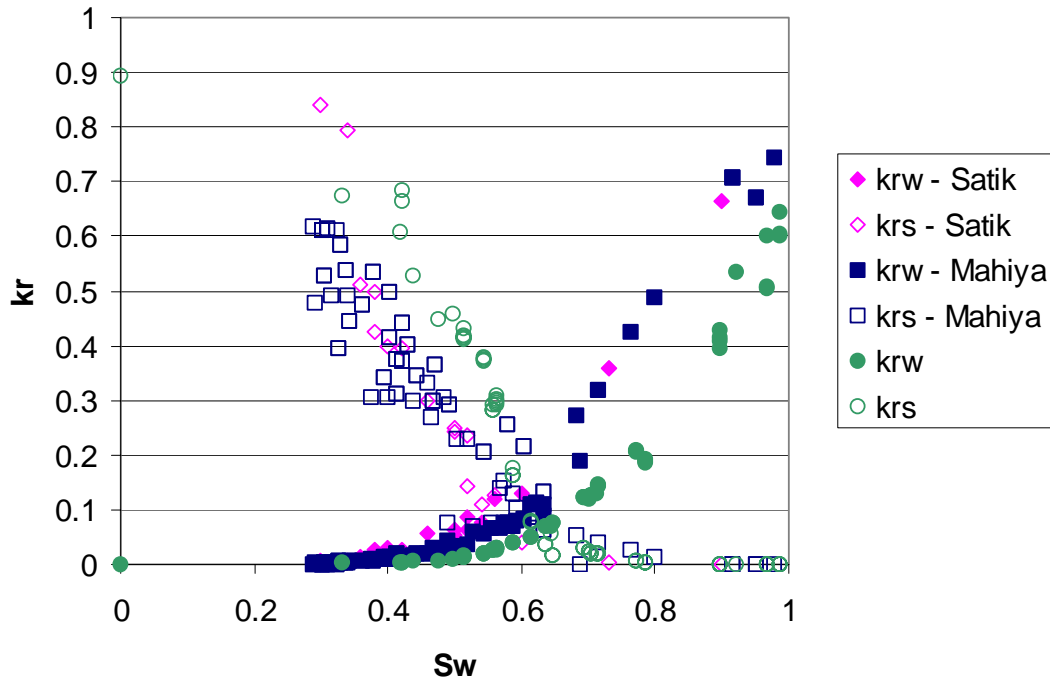


Figure 1.12: Comparison of results with previous experiments.

#### **1.4 CONCLUSIONS**

This experiment built on the methodology developed in previous experiments to determine steam-water relative permeability at constant pressure gradient. Heat flux was controlled successfully to maintain adiabatic conditions within the core, though concerns remain about excessive heat gain or loss through the inlet. A constant pressure gradient was maintained in most cases, though maintaining a constant pressure gradient at high water flow rates continues to be a challenge.

A comprehensive data set was compiled. Pressure, temperature, and saturation were measured and recorded and used to calculate relative permeability. The data were then analyzed in a number of ways, and several representations of the steam-water relative permeability relations were presented.

The relative permeability relations suggested by this study support a Corey-type profile for water relative permeability, though they suggest otherwise for steam relative permeability. As in previous experiments, residual water saturation of this core was found to be in the vicinity of 30%. Residual steam saturation was more difficult to determine but apparently near 10%. The steam phase slip factor has a significant effect on the relative permeability. If not considered, it will increase the apparent relative permeability of the steam phase by 20-40%.

This relative permeability experiment focused on a specific Berea sandstone core under a pressure gradient of 15 psi across 43 cm, with an inlet temperature of 120 °C. As geothermal reservoirs tend to be of a composition different than sandstone, with temperatures in excess of 120 °C, these results are not directly applicable to geothermal reservoir engineering in their current form. However, they do provide important insights into the general behavior of steam and water in two-phase flow, which should be similar in form if not in detail to the flow properties of steam and water under geothermal conditions. The experimental methodology established should prove useful for expanding this experiment to include geothermal reservoir material.

For the immediate future, it is our hope that subsequent investigations involve similar experiments at a different pressure gradient, to evaluate the role of pressure and temperature on relative permeability. Experimentation at a greater pressure gradient may require the development of a different core holder mechanism, while experimentation at a lesser pressure gradient may require more sensitive and precise transducers.

## **2. STEAM-WATER CAPILLARY PRESSURE**

This research project is being conducted by Research Associate Kewen Li and Professor Roland Horne. The objective of this project is to investigate the fundamentals of steam-water capillary pressures during drainage processes. In this report, we present the results of water drainage in both steam-water and air-water systems. The differences between steam-water and air-water capillary pressures were identified.

### **2.1 SUMMARY**

We conducted both steam-water and air-water gravity drainage tests in a vertically positioned ceramic core sample. The core sample was scanned using an X-ray CT scanner. The results were compared and differences between drainage steam-water and air-water capillary pressures were found. The drainage steam-water capillary pressure was less than the air-water capillary pressure.

### **2.2 INTRODUCTION**

Li and Horne (2001) found significant differences between steam-water and air-water capillary pressures in imbibition processes. However, the steam-water and air-water capillary pressures were measured at different temperatures. To compare the two, Li and Horne (2001) used a J-function approach to scale the air-water capillary pressures measured at low temperature to the high temperature at which the steam-water capillary pressures were measured. The main purpose of the current stage of the study was to exclude the effect of temperature. The gravity drainage tests in both steam-water and air-water systems were conducted at the same temperature. The relationships between height and water saturation were measured by the X-ray CT method after equilibrium between gravity and capillary pressure was reached.

We also changed the way of scanning the core sample from the vertical mode to the horizontal mode. The core sample was still positioned vertically but the X-ray CT scanner was positioned horizontally. By doing so, it is not necessary to move the core sample up and down. Moving the core is not convenient and may cause position shift. We could also obtain the whole water saturation profile (the relationship between the water saturation and the height) through just one scanning. Therefore, we were able to monitor the process of the spontaneous water imbibition into the core sample in a better way.

### **2.3 THEORY**

The basic theory behind the measurements of steam-water and air-water capillary pressures is the balance between gravity and capillary pressure as a function of height in a core sample positioned vertically. Steam-water or air-water capillary pressure is equal to the gravity force once the spontaneous water imbibition into the core sample has been completed. The equation is expressed as follows:

$$P_{ci} = \Delta\rho gh \tag{2.1}$$

where  $P_{ci}$  is the steam-water or air-water capillary pressure;  $\Delta\rho$  is the density difference between water and steam or air;  $g$  is gravity constant and  $h$  the height. The water saturation in the core at  $h$  was measured by using the X-ray CT method. Water saturation is calculated as follows:

$$S_w = \frac{CT_{exp}(T) - CT_{dry}(T)}{CT_{wet}(T) - CT_{dry}(T)} \quad (2.2)$$

where  $CT_{wet}(T)$ ,  $CT_{dry}(T)$  are CT numbers of the core when it is fully saturated by water and air respectively;  $CT_{exp}(T)$  is the CT number of the rock when it is partially saturated by steam, all at the same temperature  $T$ .

Porosity measured by the X-ray CT method is computed using the following expression:

$$\phi = \frac{CT_{wet}(T) - CT_{dry}(T)}{CT_{water}(T) - CT_{air}(T)} \quad (2.3)$$

here  $CT_{water}$  and  $CT_{air}$  are the CT numbers of water and air respectively.

Once the porosity is known, the water saturation can be calculated as follows:

$$S_w = \frac{CT_{exp}(T) - CT_{dry}(T)}{\phi[CT_{water}(T) - CT_{air}(T)]} \quad (2.4)$$

## **2.4 EXPERIMENTS**

**Rock and Fluids.** Distilled water was used as the liquid phase in this study; the specific gravity and viscosity were 1.0 and 1.0 cp at 20°C. Steam and air were used as the gas phase; the surface tension of water/air at 20°C was 72.75 dynes/cm. It was assumed, as usual, that there were no differences between the surface tension of water/air and that of water/steam. The ceramic sample was provided by Refractron Technologies Corp. It had a porosity of 40.90%, a length of 25.0 cm, an inner diameter of 4.275 cm and an outer diameter of 6.287 cm. We did not measure the permeability of the core sample due to its special shape but the permeability was estimated to be over 15 darcy.

The ceramic core sample had a hollow center; the cross-section is shown in Fig. 2.1 (a) schematically and the scanning image from the direction perpendicular to the cross-section of the core sample is shown in Fig. 2.1 (b).

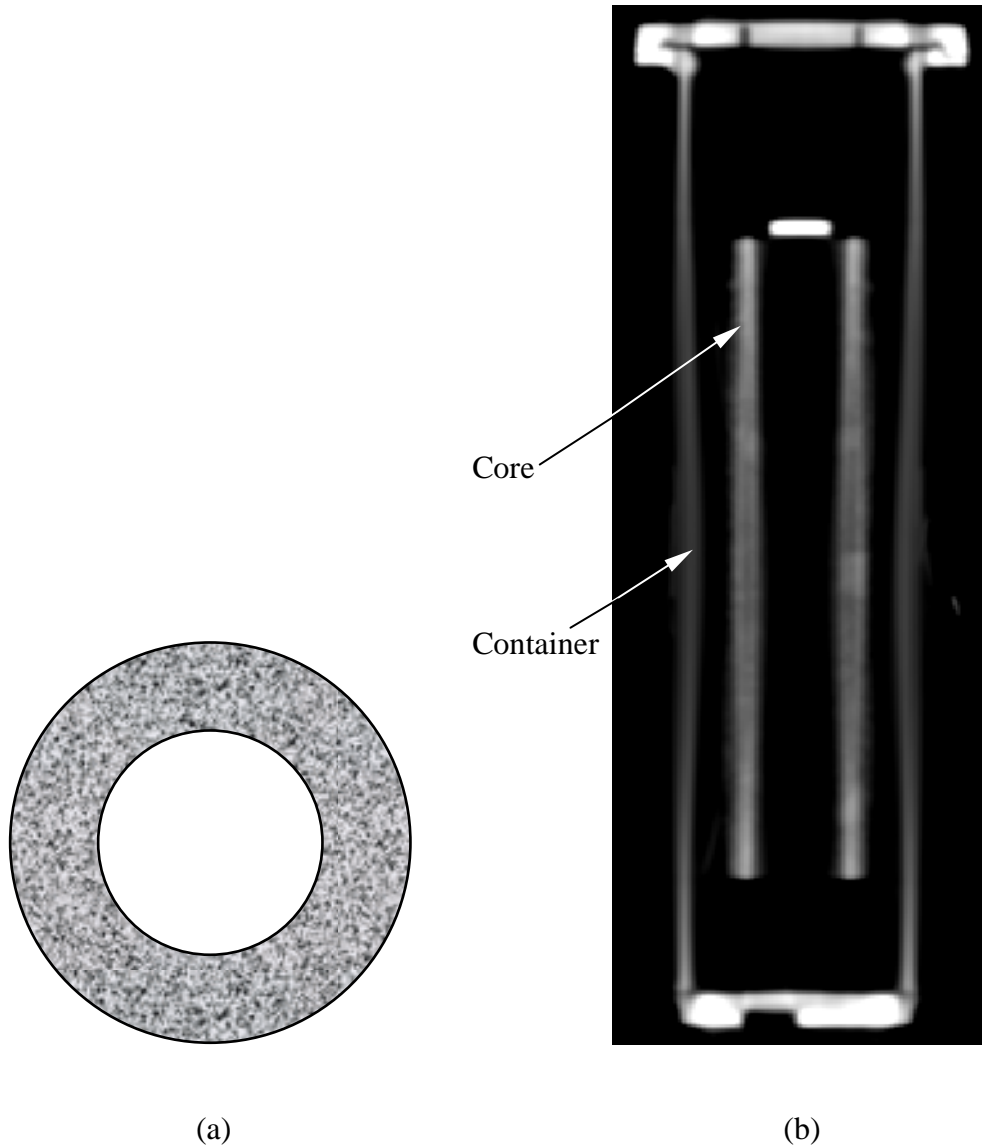


*Figure 2.1: Shape of the ceramic core sample.*

**X-ray CT Scanner.** Distribution of water saturation in the core sample was measured along the height using a Picker<sup>TM</sup> Synerview X-ray CT scanner (Model 1200 SX) with 1200 fixed detectors. The voxel dimension was 0.5 mm by 0.5 mm by 5 mm, the tube current used was 50 mA, and the energy level of the radiation was 140 keV. The acquisition time of one image was about 3 seconds while the processing time was around 40 seconds.

**Experimental Apparatus.** A schematic of the apparatus to measure steam-water and air water capillary pressures is shown in Fig. 2.2. The core system was assembled in an aluminum containment vessel.

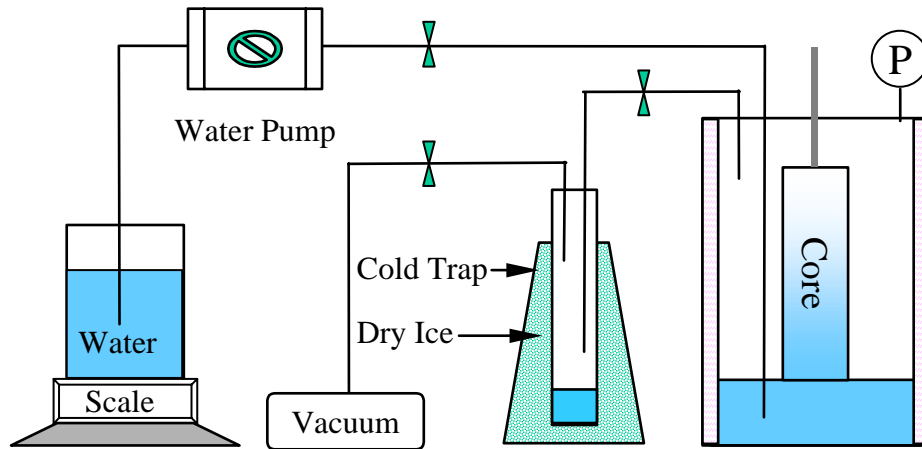


Figure 2.2: Schematic of the apparatus for steam-water and air-water capillary pressure.

The vacuum pump (Welch Technology, Inc., Model 8915) was used to remove the air in the core sample and in the aluminum cylinder in order to generate the steam-water environments. A cold trap with dry ice was employed to protect the steam from entering the vacuum pump to extend its life and reduce the frequency of replacing the pump oil.

Water in the aluminum cylinder was delivered by the water pump (Dynamax, Model SD-200, manufactured by RAININ Instrument Co.) and the amount was measured by the scale (Mettler, Model PE 1600) with an accuracy of 0.01g and a range from 0 to 1600g.

**Procedure.** The core sample assembled in the container was dried and saturated with water. An X-ray CT scan was made before and after the core was saturated with water. Then the drainage test in air-water systems was conducted by draining water in the container and letting air in. Another X-ray CT scan was made after the drainage was completed. The X-ray CT scanner was positioned in horizontal mode so the scanning section plan was parallel to the cross-section of the core sample. To do the drainage test in steam-water systems, the same procedure was repeated. The main difference was the way to drain water from the container to create a steam-water system. No air was allowed to enter the core and the container during the water drain by evacuating at the bottom of the container. The amount of water drained was monitored by scanning the core system from time to time.

## **2.5 RESULTS**

We conducted water drainage tests in both steam-water and air-water systems. Fig. 2.3 shows the CT values of the left part of the core sample (see Fig. 2.1b) when the core was dry and saturated with water. The CT values were obtained by the ROI function of the software FP Image Viewer.

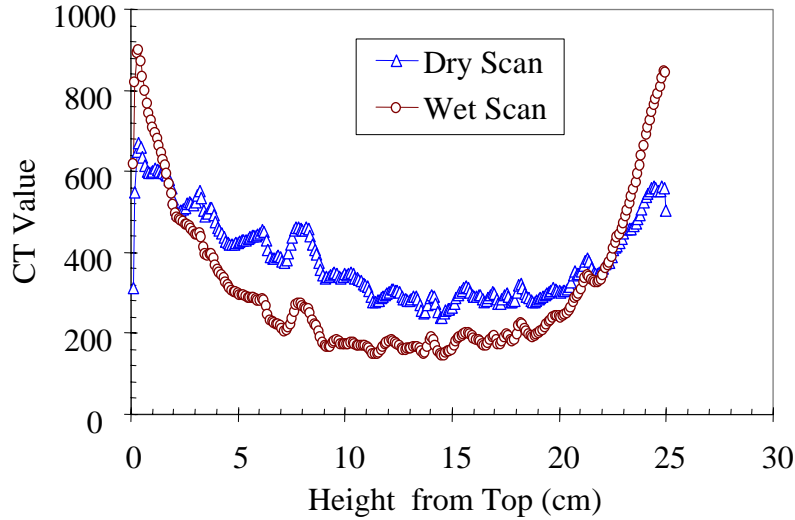


Figure 2.3: Distribution of CT value in the core sample before and after the saturation with water.

The CT values of the core saturated with water should be greater than the CT values of the dry core. However, Fig. 2.3 shows the opposite trend at some of the positions in the core. This may be caused by artifacts caused by the beam hardening effect. We could not calculate the porosity from these measurements. Fig. 2.4 shows the CT value distributions in the core for both steam-water and air-water drainage tests.

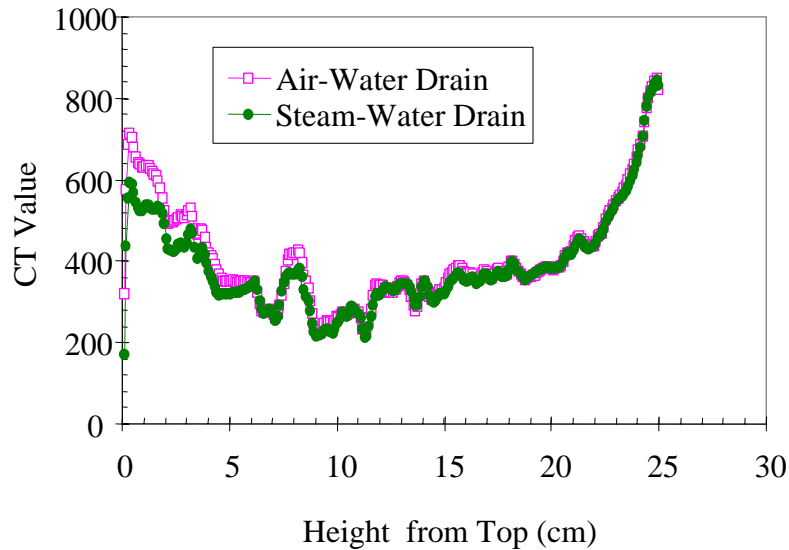


Figure 2.4: CT value distributions in the core for both steam-water and air-water drainage tests.

The open squares represent the air-water drainage and the solid circles represent the steam-water drainage. At the bottom of the core, there is almost no difference between the steam-water and air-water drainage tests. This is consistent with our previous experimental results (Li and Horne, 2001). Above a certain height, the CT values of the

steam-water case are less than the air-water case. This implies, according to Eq. 2.4, that the water saturation in steam-water drainage is less than that in air-water drainage at the same height in the core. Therefore, we can see from these experimental results that the steam-water drainage capillary pressure is less than the air-water drainage capillary pressure. This is consistent with the experimental results in imbibition cases from Li and Horne (2001).

## **2.6 CONCLUSIONS**

Based on the present study, the following conclusions may be drawn:

1. Drainage steam-water capillary pressure in the ceramic core sample studied is less than the drainage air-water capillary pressure at the same water saturation. This is consistent with the experimental results in imbibition cases.
2. The experimental results in the drainage case also show that we may not be able to substitute steam-water flow simply using air-water flow.

Because of the effect of X-ray beam hardening artifacts, we need to confirm the experimental results in this study.

### **3. SCALING OF WATER IMBIBITION DATA**

This research project was conducted by Research Associate Kewen Li and Professor Roland Horne. The goal of this study was to develop a method to scale the experimental data of spontaneous water imbibition (cocurrent) for gas-water systems.

#### **3.1 SUMMARY**

Spontaneous water imbibition is an important mechanism during water injection into geothermal reservoirs. Scaling the experimental data has been a challenge for gas-water systems. Ignoring the effects of wettability and gravity in the dimensionless time could be the reason. In this study we developed a method to scale the experimental data of spontaneous water imbibition for gas-liquid systems. In this method, we defined a dimensionless time with wettability and gravity included. The definition was not empirical as usual but based on a theoretical derivation. Using this dimensionless time, experimental data from spontaneous water imbibition in different rocks with different size, porosity, permeability, initial water saturation, interfacial tension, and wettability could be scaled. The scaling results from this study demonstrate that the spontaneous cocurrent water imbibition in gas-water systems could be predicted.

#### **3.2 INTRODUCTION**

Geothermal reservoirs are usually highly fractured. When water is injected in highly fractured reservoirs, the amount and the rate of water imbibition from the fracture into the matrix by spontaneous imbibition are essential to the understanding of reservoir performance. The process of spontaneous water imbibition is controlled by the properties of the porous medium, fluids, and their interactions. These include porosity, permeability, pore structure, matrix size and shape, boundary condition, fluid viscosity, initial water saturation, wettability, the interfacial tension, relative permeability, and gravity. Scaling spontaneous water imbibition is important to evaluate the production performance because so many factors are involved. In order to successfully scale the experimental data, it may be necessary to consider the effects of all the significant factors. Scaling has been investigated widely in oil-water systems but rarely in gas-liquid systems.

Dimensionless time is usually defined as follows (Ma *et al.*, 1995):

$$t_D = \sqrt{\frac{k}{\phi}} \frac{\sigma}{\mu_m L_a^2} t \quad (3.1)$$

where  $t_D$  is the dimensionless time,  $k$  is the rock permeability,  $\phi$  is the porosity,  $\sigma$  is the interfacial tension between oil and water,  $t$  is the imbibition time,  $\mu_m$  is the geometric mean of water and oil viscosities and  $L_a$  is the characteristic length defined as follows:

$$L_a = \sqrt{\frac{V}{\sum_{i=1}^n \frac{A_i}{d_{ai}}}} \quad (3.2)$$

where  $V$  is the bulk volume of the matrix,  $A_i$  is the area open to imbibition in the  $i$ th direction, and  $d_{ai}$  is the distance traveled by the imbibition front from the open surface to the no-flow boundary.

The scaling group in Eq. 3.1 was modified from Mattax and KYTE (1962) who used only the water viscosity in the scaling group but a condition for scaling was that the viscosity ratio in the laboratory tests be equal to that in the reservoirs. Ma *et al.* (1995) proposed the geometric mean of the oil and water viscosities in the scaling group. Eq. 3.1 was verified experimentally by Zhang *et al.* (1996) in oil-water-rock systems. Zhang *et al.* (1996) mentioned that the geometric mean of the oil and water viscosities did not scale results in gas-liquid-rock systems. Eq. 3.2 was modified from the shape factor suggested by Kazemi *et al.* (1989)

As pointed out by Zhang *et al.* (1996), when the dimensionless time defined in Eq. 3.1 was used to scale the experimental data in gas-liquid systems, the results were scattered significantly. Therefore, we developed a method to scale the experimental data of spontaneous water imbibition (cocurrent) for gas-water systems using a newly defined scaling group with almost all the factors included. This method was verified experimentally by the data from different rocks (Berea and geothermal rocks from The Geysers) with different size, porosity, permeability, initial water saturation, and wettability.

### **3.3 THEORY**

A scaling model was developed in this section based on the solution to the recovery by spontaneous water imbibition. Li and Horne (2001) proposed a linear model to characterize the process of cocurrent spontaneous water imbibition. The model reveals a linear relationship between the imbibition rate and the reciprocal of the gas recovery by spontaneous water imbibition and is expressed as follows:

$$Q_w = \frac{dN_{wt}}{dt} = a \frac{1}{R} - b \quad (3.3)$$

where  $Q_w$  is the rate of water imbibition,  $N_{wt}$  is the accumulative volume of water imbibed into rocks,  $R$  is the recovery and is equal to  $N_{wt}/V_p$  ( $V_p$  is the pore volume).  $a$  and  $b$  are two constants representing capillary pressure force and gravity force respectively. The values of  $a$  and  $b$  can be calculated from the spontaneous water imbibition data using Eq. 3.3. The details of the calculation of  $a$  and  $b$  were shown in Li and Horne (2001).  $a$  is expressed as follows:

$$a = \frac{Ak_w (S_{wf} - S_{wi})}{\mu_w L} P_c \quad (3.4)$$

where  $A$  and  $L$  are the cross-section area and the length of the core respectively,  $\mu_w$  is the viscosity of water,  $S_{wi}$  is the initial water saturation and  $S_{wf}$  is the water saturation behind the imbibition front;  $k_w$  is the effective permeability of water phase at a water saturation of  $S_{wf}$ . Similarly,  $P_c$  is the capillary pressure at  $S_{wf}$ .

Constant  $b$  is expressed as follows:

$$b = \frac{Ak_w}{\mu_w} \Delta\rho g \quad (3.5)$$

where  $\Delta\rho$  is the density difference between water and gas and  $g$  is the gravity constant.

Given that:

$$c = \frac{b}{a} \quad (3.6)$$

$$R^* = cR \quad (3.7)$$

and

$$t_d = c^2 \frac{k_w}{\phi} \frac{P_c}{\mu_w} \frac{S_{wf} - S_{wi}}{L_a^2} t \quad (3.8)$$

here  $c$  is the ratio of the gravity force to the capillary force,  $t_d$  is the dimensionless time with gravity and capillary forces included. In the cocurrent water imbibition case in this study,  $L_a$  is equal to the core length.

Substituting Eqs. 3.6, 3.7, and Eq. 3.8 into Eq. 3.3, the following equation is obtained:

$$\frac{R^* dR^*}{dt_d} = 1 - R^* \quad (3.9)$$

We found experimentally that  $R^*$  was less than 1.0 in most cases. Therefore, the solution of Eq. 3.9 is:

$$\ln(1 - R^*) + R^* = -t_d \quad (3.10)$$

Eq. 3.10 could also be expressed as follows:

$$(1 - R^*)e^{R^*} = e^{-t_d} \quad (3.11)$$

We can see from Eq. 3.11 that  $R^*$  is only a function of the newly defined dimensionless time. This feature shows that experimental data from spontaneous water imbibition in rocks with different size, porosity, permeability, initial water saturation, interfacial tension, and wettability can be scaled to a single curve of  $R^*$  vs.  $t_d$ .

The term  $e^{R^*}$  will be close to 1 when  $R^*$  is small enough. Therefore, Eq. 3.11 is reduced as follows:

$$R^* = 1 - e^{-t_d} \quad (3.12)$$

Eq. 3.12 is in the form of an imbibition model suggested by Aronofsky *et al.* (1958).

It is known:

$$\ln(1 - R^*) = -R^* - \frac{1}{2}(R^*)^2 - \frac{1}{3}(R^*)^3 - \dots \quad (3.13)$$

Substituting Eq. 3.13 into Eq. 3.10 after neglecting the third- and the greater-order terms, the following expression can be obtained:

$$(R^*)^2 = 2t_d \quad (3.14)$$

Eq. 3.14 can be expressed as follows:

$$N_{wt}^2 = \frac{2P_c k_w \phi (S_{wf} - S_{wi}) A^2}{\mu_w} t \quad (3.15)$$

Eq. 3.15 is similar to the Handy equation (Handy, 1960). The only difference between the two is that initial water saturation is not included in the Handy equation.

The imbibition model suggested by Aronofsky *et al.* (1958) and the Handy equation (Handy, 1960) are the models most often used to characterize the process of spontaneous water imbibition. According to the new analysis, we can see that the imbibition model proposed by Li and Horne (2001) is more generalized. This is because the Li and Horne model includes both the Handy equation and that suggested by Aronofsky *et al.* (1958).

### **3.4 EXPERIMENTS**

The tests of spontaneous water imbibition (cocurrent) in Berea sandstone with clay removed by firing were conducted by Li and Horne (2001). Also conducted by Li and

Horne (2000) were the experiments in the rocks from The Geysers. The experimental data were used to verify the scaling method developed in this study.

**Fluids.** Air was used as the gas phase and distilled water as the liquid phase because the clay in the Berea sandstone core was deactivated by firing. The surface tension of water/air at 20°C is 72.75 dynes/cm.

**Core Samples.** The Berea sandstone sample had a permeability of around 1200 md and a porosity of about 24.5%; its length and diameter were 43.5 cm and 5.06 cm. The Geysers rock sample from a depth of 1410.1m was obtained from the Energy and Geoscience Institute; its porosity was about 4.5%. The matrix permeability of the rock sample is not available yet. The permeability of a nearby sample measured by nitrogen injection was about 0.56 md (after calibration of gas slip effect), which is probably attributable mainly to the fracture permeability. The length and diameter of this rock sample were 3.52 cm and 8.25 cm.

### 3.5 RESULTS

The amount of water imbibed into the Berea sandstone at three different initial water saturations and the dry rock from The Geysers geothermal field are shown in Figure 3.1.

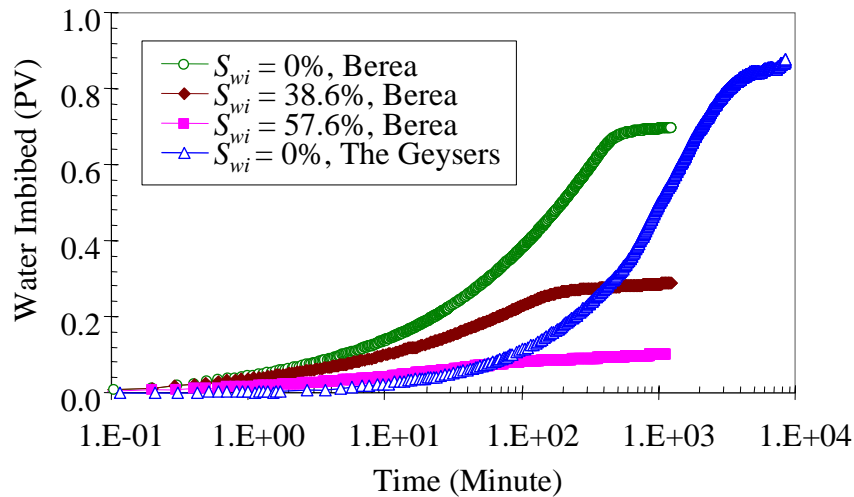


*Figure 3.1: Spontaneous water imbibition behavior in Berea sandstone and The Geysers rock.*

Figure 3.2 shows the scaling results using the dimensionless time defined in Eq.3.1. Note that only water viscosity was used in the scaling. The geometric mean viscosity term in Eq. 3.1 was substituted by the viscosity of water. It is supposed that all the experimental data points from different rocks at different initial water saturations should sit close to a single curve if the dimensionless time is appropriate for the scaling. However, Figure 3.2 demonstrates that the experimental data scatter significantly.

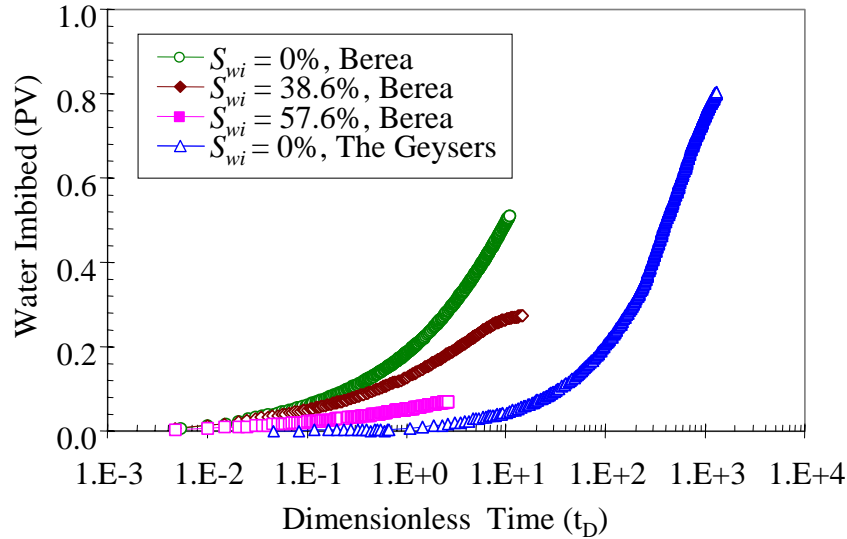


Figure 3.2: Scaling using existing dimensionless time for Berea sandstone and The Geysers Rock.

Using the scaling model (Eqs. 3.8 and 3.11) developed in this study, the same experimental data used in Figure 3.2 were scaled and the results are shown in Figure 3.3.

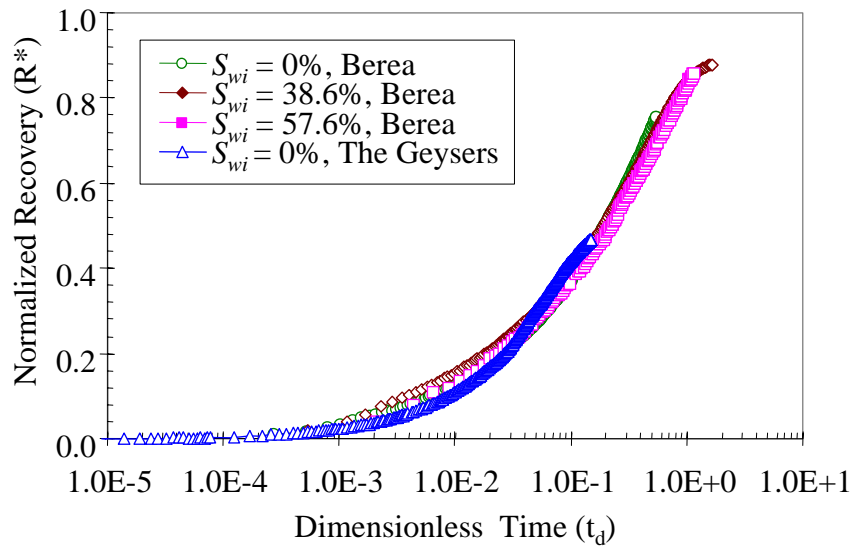


Figure 3.3: Scaling using the scale model developed in this study for Berea sandstone and The Geysers Rock.

Note that the experimental data points after the water imbibition front contacted the top of the core sample were not plotted in either Figure 3.3 or in Figure 3.2. This is because the scaling model was based on Eq. 3.3 that only applies before the water contacts the top of the core sample. We can see from Figure 3.3 that the proposed scaling model works well for spontaneous water imbibition data in The Geysers rock and Berea sandstone, even at different initial water saturations.

### **3.6 CONCLUSIONS**

Based on the present study, the following conclusions may be drawn:

1. A scaling model was derived according to an imbibition model proposed by Li and Horne (2001).
2. The imbibition model proposed by Li and Horne (2001) includes both the Handy equation and the imbibition model suggested by Aronofsky *et al.* (1958).
3. The spontaneous water imbibition data obtained in different rocks (Berea sandstone and The Geysers rock) under different conditions can be scaled using the scaling model developed here.

In the next stage of the work, we will verify the method developed in this study using more data of spontaneous water imbibition data from different rocks.



## **4. FRACTURED ROCK RELATIVE PERMEABILITY**

This project is being conducted by Research Assistant Mark D. Habana, Research Associate Kewen Li and Prof. Roland N. Horne. The objective is to measure relative permeability relations for steam and water flow in a fractured geothermal rock. This work is an extension of current studies of steam-water flows, which have so far considered only artificially uniform porous rock. This quarter, further analysis of the gas experiments was done. Also, a nitrogen-water relative permeability experiment was conducted on The Geysers core and an electrical resistivity tomography (ERT) experiment, using a different core, was done inside the CT scanner.

### **4.1 BACKGROUND**

Various works on flow through fractures have shown different kinds of relative permeability behavior. Experimental studies by Persoff and Pruess (1995) resulted in curves that can not be classified either as Corey type or as linear (X-curve) type. Fourar et al. (1993) suggested that multiphase interaction in a fracture is a function of flow velocity and therefore that relative permeability is not the appropriate way to describe multiphase flow in fractures.

Past experiments have used synthetic fabricated fractures and/or gas-water or oil-water as fluids. This experimental study will use a real fractured core from The Geysers geothermal field to study steam-water relative permeability.

Nitrogen and helium permeability experiments were conducted on the core to determine the effects of the rock fractures and to investigate the constraints and practicalities of conducting multiphase flow experiments in real geothermal rocks. The core contains several fractures as determined from an X-ray computer tomography image.

Experiments were also conducted to develop an electrical resistivity tomography (ERT) method to measure saturations in the core. This saturation measurement technique is more appropriate than X-ray CT because of the long duration of the experiment and because of the application of high confining pressures in the planned steam-water relative permeability experiment.

### **4.2 EXPERIMENTAL METHODOLOGY**

The rock permeability was measured using nitrogen and helium gas at room temperature. The apparatus used is shown in Figure 4.1. Since gas permeability is a function of pressure, as described by Equation 4.1, the flow measurements were conducted at a series of different mean pressures.

$$k_{gas} = k_{abs} \left(1 - \frac{b}{p_{ave}}\right) \quad (4.1)$$

The core sample was obtained from a depth of 1409.3m at The Geysers geothermal field. The core is 6.91 cm in length and 4.70 cm in diameter.

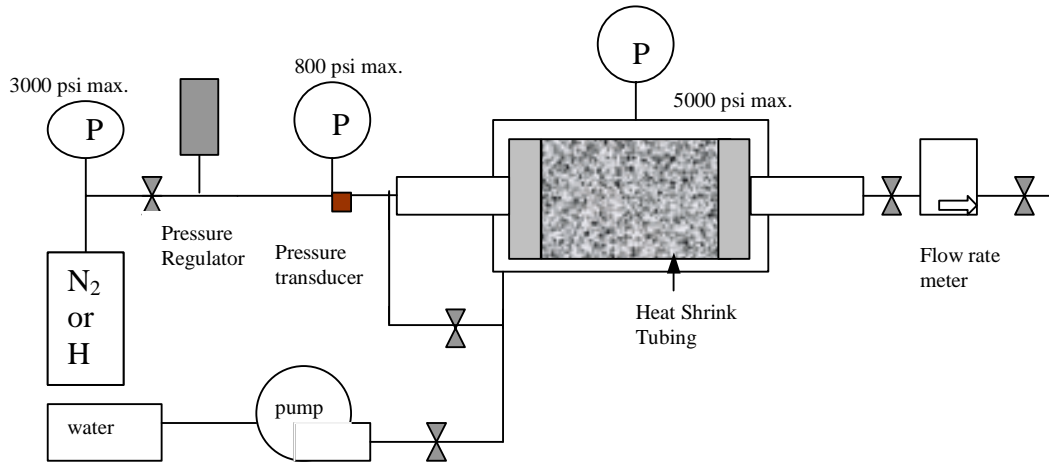


Figure 4.1: Apparatus for flow measurement in geothermal rock.

A pressure gauge and a pressure transducer connected to a digital display measured pressure at the inlet. The pressure at the outlet was taken to be 1 atm. The flow rate at the outlet was measured using a Matheson flow rate meter and controller (Model 8272-MF2000). The flow rate transducer calibration equation used was that determined by Kewen Li when he used the device in his experiments on slip factors (Oct-Dec 1999 Quarterly Report).

For the nitrogen-water relative permeability experiment, at a confining pressure of 850 psig, water was pumped into the core up to irreducible gas saturation. Irreducible gas saturation was determined by the absence of gas flow through the translucent outlet tube. Then, nitrogen gas was pumped to displace the water in the core. Refer to Figure 4.2.

The flowmeter was placed upstream of the inlet. The first graduated cylinder was filled with water and inverted while the second graduated cylinder was placed on a weighing scale. The gas coming out of the core was trapped in the first cylinder and the displaced water flowed into the second cylinder. The water in the second cylinder is equal to the sum of the volume of the gas in the first cylinder and the water from the core outlet.

Figure 4.3 shows the apparatus used in the ERT experiment. Several wires, held in place by rubber sheets, are in contact with the core. Heat shrink tubing was wrapped around the core and the wires to decrease water evaporation rate. Water was made to imbibe into the core and resistance readings were taken. The core was placed in the CT scanner while the resistance readings between nodes, at the same cross section of the core, were taken.

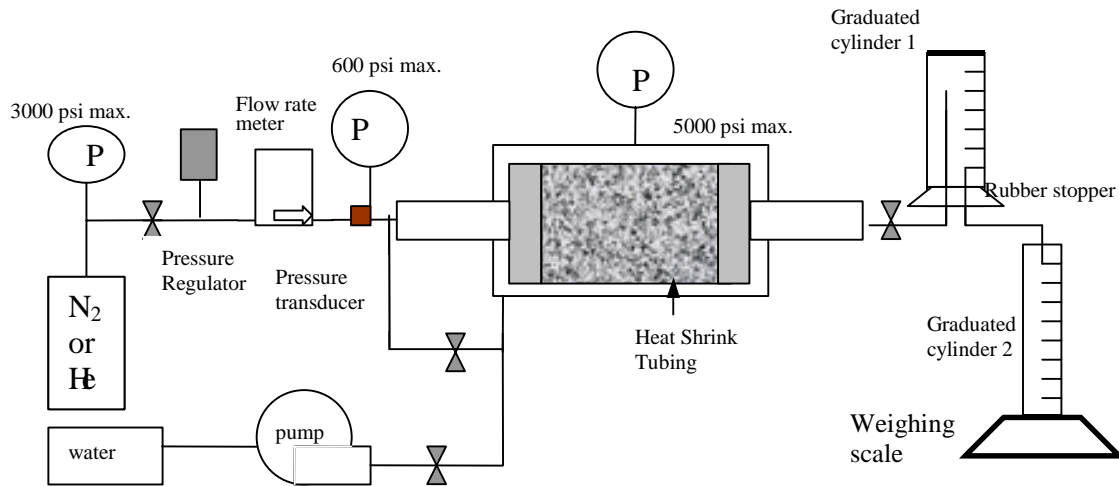


Figure 4.2: Apparatus for nitrogen-water relative permeability experiment.

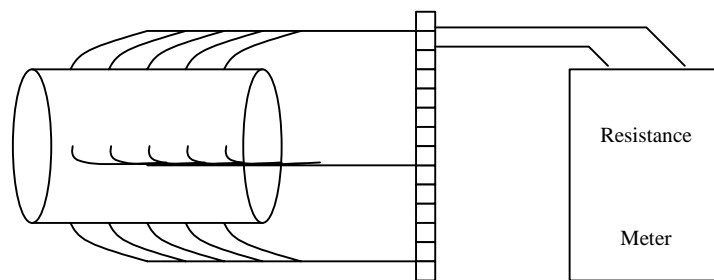


Figure 4.3: Apparatus for ERT experiment in the CT scanner.

### **4.3 PARTIAL RESULTS AND DISCUSSION**

Figures 4.4 and 4.5 show two helium experiment results compared to the two nitrogen experiments preceding each helium experiment. All four flow experiments were done at a confining pressure of 850 psig. For the helium experiment the permeabilities obtained are higher than the values from the nitrogen experiments. Also, the slope for the helium experiment is lower than that for nitrogen at high confining pressures. This is not as expected. The slope for helium should be much steeper than that for nitrogen considering the difference in viscosities and molecular weights of the two fluids.

The behavior of helium in the experiments can not be explained by the theories of flow through porous media because helium was in supercritical condition throughout most of the experiment. The helium data points to the left of the broken line in Figure 4.5 and Figure 4.6 are at supercritical conditions.

Analyses of the data of the nitrogen-water relative permeability experiment and the ERT experiment is not yet complete.

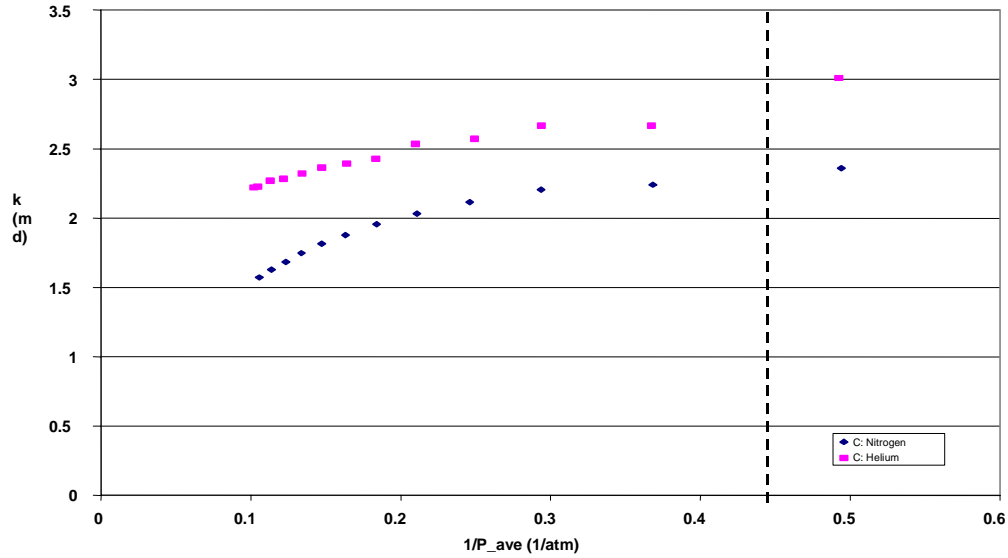


Figure 4.4: Results of helium and nitrogen permeability as a function of pressure.

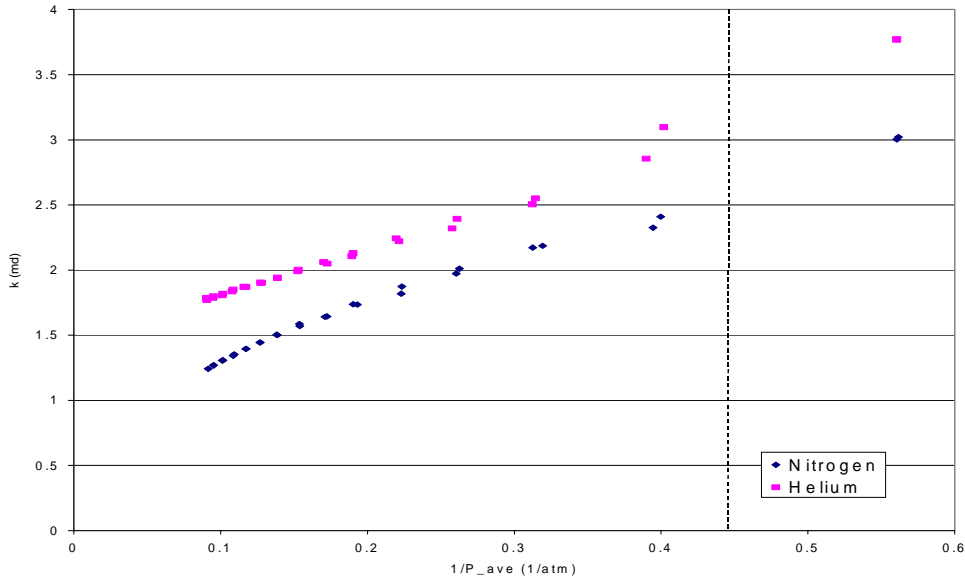


Figure 4.5: Results of helium and nitrogen permeability as a function of pressure.

#### **4.4 CONTINUING AND FUTURE WORK**

The ERT experiment data will be used to develop a mathematical procedure to determine saturation from multi-node resistance measurements.

After establishing a method to determine the saturation from resistance measurements and after analyses of the nitrogen-water relative permeability experiment data the next step will be the design and construction of an apparatus for the steam-water relative permeability experiment. The steam-water relative permeability experiment will be an unsteady-state displacement process.



## **5. THE MEASUREMENT OF STEAM-WATER CAPILLARY PRESSURE**

This research project is being conducted by Research Assistant Chih-Ying Chen, Research Associate Kewen Li, and Professor Roland Horne. The aim is to measure steam-water and air-water capillary pressures, and to distinguish the difference between them. A simple experiment has been finished measuring capillary rise in narrow tubes. Preliminary data were acquired and will be used for future research reference. A new capillary pressure apparatus has been constructed for measurements in real rocks.

### **5.1 BACKGROUND**

Capillary pressure, an important but hard-to-measure physical property, plays a significant role in reservoir performance and production forecasting. In the geothermal engineering field, the knowledge of the steam-water capillary pressure is limited because of difficulties in the measurement. Most of the difficulties come from the phase relationship between the steam and the liquid water. There is mass transfer between the steam and the water phase which makes conventional measurement methods invalid or inaccurate. Horne et al. (1995) summarized the adsorption mechanism in geothermal reservoirs and described how adsorption curves could be used to infer capillary pressures. Sta. Maria and Pingol (1996), and Persoff and Hulen (1996) inferred values of steam-water capillary pressure from the adsorption data of Horne et al. (1995), and found steam-water capillary pressures ranging from 0 to 586 MPa (at 120°C) and 0 to 190 MPa (at 28.5°C) respectively. The difference between these two results is large. Li and Horne (2000) developed a mathematical model to calculate steam-water capillary pressure of geothermal rocks using the steady-state steam-water flow experiment, and the results obtained were consistent with those measured by Persoff and Hulen (1996).

A capillary rise experiment is a straightforward way to measure the capillary pressure. A schematic of capillary rise is shown in Figure 5.1. The capillary pressure can be obtained using the following equation:

$$P_c = \Delta\rho gh \quad (5.1)$$

where  $\Delta\rho = \rho_w - \rho_g$  denotes the difference in density between the water phase and gas phase;  $g$  is the gravity constant and  $h$  is the height of the capillary rise of the meniscus above a flat liquid surface.

The capillary pressure can be also represented in terms of the tube radius, contact angle, surface tension in a circular capillary tube:

$$P_c = \frac{2\sigma \cos \theta}{r} \quad (5.2)$$

where  $\sigma$  denotes the interfacial tension between water phase and gas phase;  $\theta$  is the contact angle and  $r$  is the radius of the capillary tube.

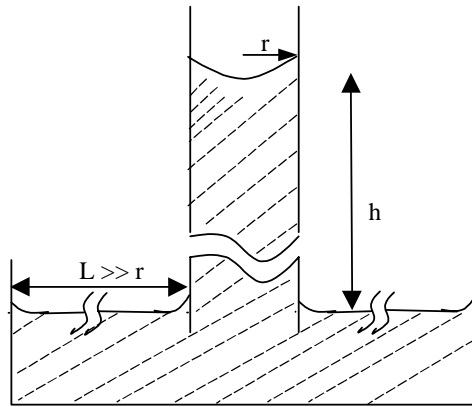


Figure 5.1: Capillary rise phenomenon (not to scale).

As discussed in previous quarterly report, the capillary rise experiment were not successful in measuring the difference between air-water and steam-water capillary pressure. This is because of problems found during the experiment. The problems were attributed to: (a) the capillary balance time; (b) the hysteresis between imbibition and drainage; (c) the quality of the tubes. These issues were discussed in the previous quarterly report.

A more practical and applied experiment has been designed using real core samples. The main goal in this experiment is to develop a practical method to measure the capillary pressure in geothermal rock. The first step has used an artificial ceramic core and a Berea sandstone core. If a satisfactory result is obtained, an actual geothermal core will be used.

## **5.2 NEW APPARATUS**

The new experiment is shown in Figure 5.2. This apparatus will be used to measure the air-water and steam-water capillary pressure of core samples at different water saturation. The properties of the samples studied are shown in Table 5.1. Two different types of cores have been used in the first stage. The ceramic core sample has characteristics of high porosity and low permeability; the Berea sandstone has a relative low porosity and high permeability. The capillary pressure in different rocks can be represented using the J-function suggested by Leverett (1941) as follows:

$$P_c = \frac{\sigma \cos \theta}{\sqrt{\frac{k}{\phi}}} J(S_w) \quad (5.3)$$

where,  $\sigma$ ,  $k$ ,  $\phi$ ,  $S_w$ , and  $J(S_w)$  are surface tension, permeability, porosity, water saturation and J-function, respectively. According to Eq. 5.3, the ceramic core sample must have much higher capillary pressure than the Berea sandstone sample because of its high porosity and low permeability properties.

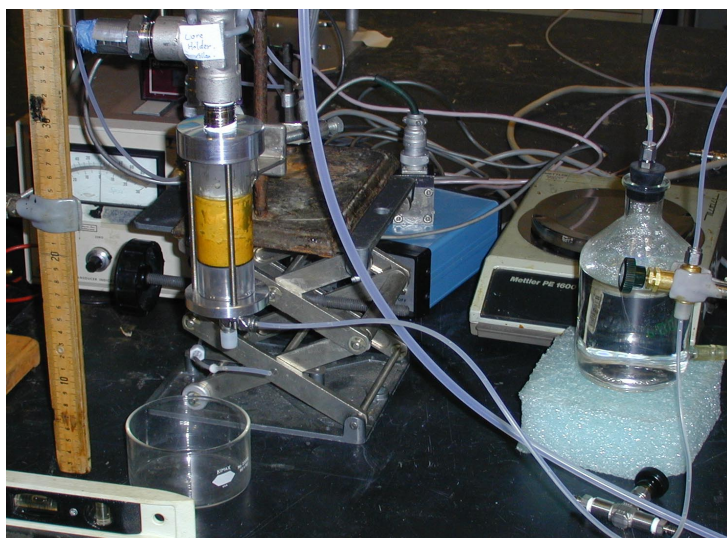


Figure 5.2: The apparatus of the air-water and steam-water capillary pressures experiment.

Table 5.1: Properties of samples studied.

Sample	Size (mm)	Pore Volume (ml)	Porosity (%)	Permeability (md)
Ceramic Core	25.62 D X 51.20 L	14.07	53.3	31.6
Berea Sandstone	25.70 D X 26.87 L	3.44	24.7	1200

### **5.3 PROCEDURES**

**Imbibition:** As described in the previous quarterly report, an unexpected gas bubble occurs between the bottom of the core sample and the water column during the imbibition capillary pressure measurement in low water saturation situations (Figure 5.3). There may be two reasons for the formation of this gas bubble. One is due to the vaporization of the water. A schematic of this situation is shown in Figure 5.4. When the water saturation in the ceramic core is small, the capillary pressure is large enough to evaporate the water and produce a vapor zone in the bottom of the core sample. A second possible reason is the breakthrough of the gas. When this experiment was designed, a piston-like water imbibition front was assumed (Figure 5.5a). However, when the imbibition behavior is not piston-like, it is easy to produce a channel through the core and allow the gas to break through at the bottom of the core. This situation can be seen in Figure 5.5(b). Once the gas bubble expands to the whole cross section of the core holder, the bubble will block the communication between water and the core. Hence, the pressure will no longer be communicated and the experiment will fail.

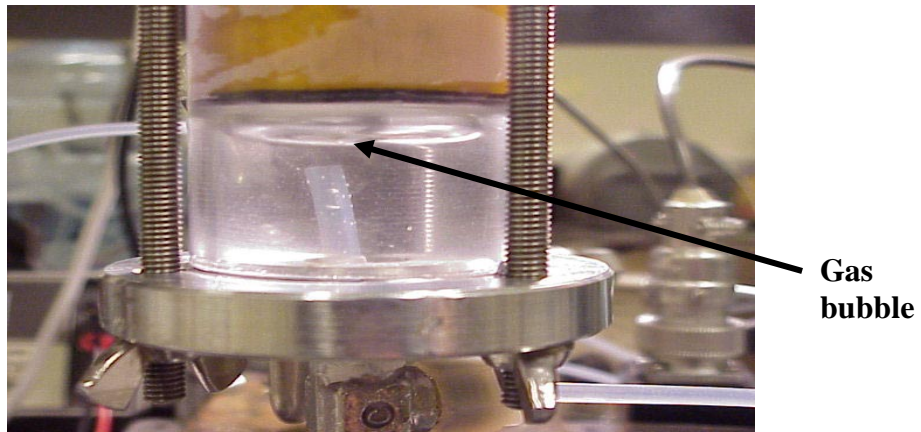


Figure 5.3: The gas bubble phenomenon.

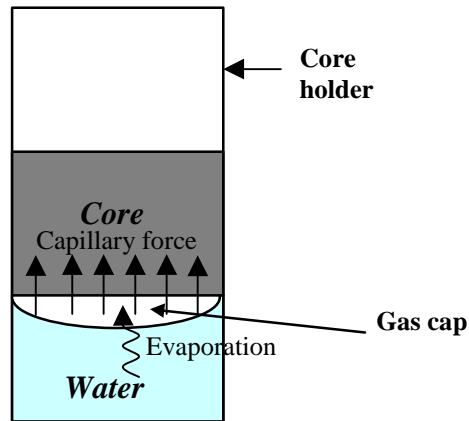


Figure 5.4: The formation of the gas cap due to water evaporation in the core holder.

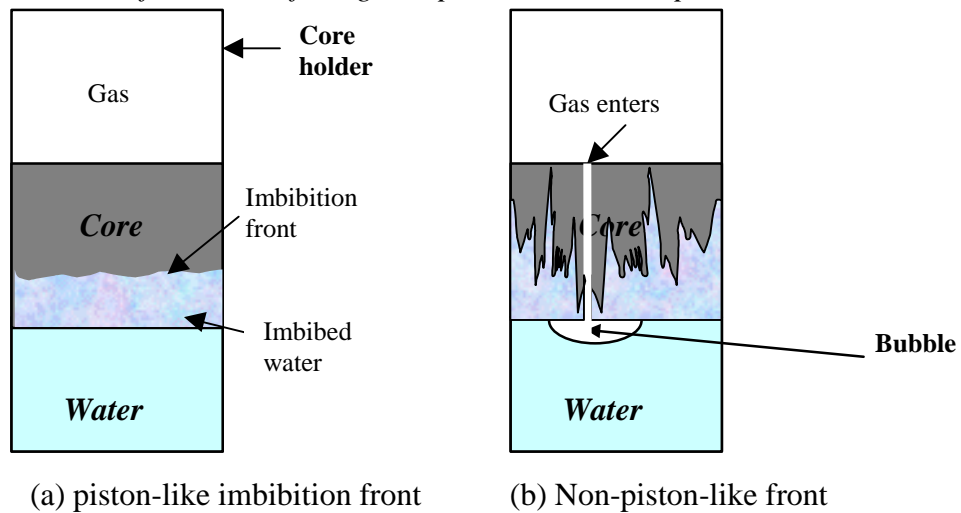


Figure 5.5: The formation of the gas cap in the core holder due to gas breaking through.

If the first explanation (water vaporization) is the main cause of the gas bubble, the problem is easy to overcome by pressurizing the whole core holder. Water will be more difficult to vaporize in the high-pressure environment. However, if the second

explanation is the cause, this method and apparatus may be not an appropriate way to measure the capillary pressure.

The apparatus for imbibition capillary pressure measurement was modified by adding a pressurizing system to reduce the water evaporation. A schematic of the apparatus is shown in Figure 5.6. In the imbibition experiment, the core holder was pressurized to 60 psig with nitrogen, and then the core holder was isolated by closing valve 1. In order to make sure there was no leak in the whole system, at least one-day pressure monitoring was necessary. In this experiment the LabView® programmable virtual instrument software and SCXI-1000 data acquisition device were used to record the pressure and weight. After passing the leak test, water was injected to the core holder using the water pump (Dynamax, SD-200). The flow rate was 5 ml/min, and the maximum injection pressure was 100 psig. The pressure difference between the top and bottom of the core sample was recorded to the computer from the pressure transducer P2, and the saturation was calculated by recording the reading change in the balance. The water saturation in the core was controlled by opening valve 2 and injecting more water.

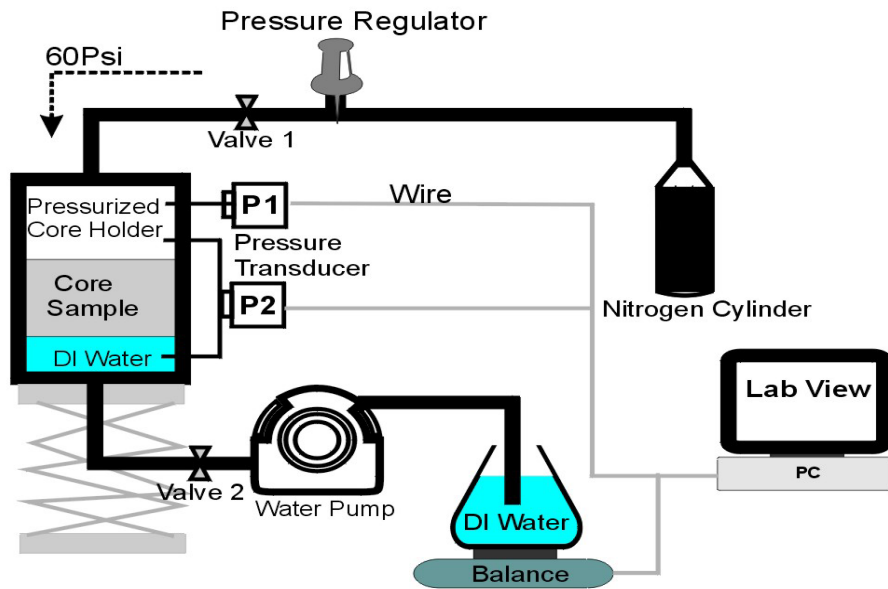


Figure 5.6: Schematic of the experiment for air-water imbibition capillary pressure.

**Drainage:** A schematic of the drainage capillary pressure experiment is shown in Figure 5.7. In the drainage experiment, for air-water capillary pressure, the core sample was fully saturated by water using the vacuum method. After saturation, the wet weight,  $W_{wet}$  was obtained by weighing the core holder. Then nitrogen was injected into the core holder. A regulator was used to adjust the inlet nitrogen pressure. The output pressure of the regulator was maintained constant with an accuracy of 0.0025 psi during the two-hour test time. We started from 1 psig inlet pressure. If there was no water produced or the reading of the water level in the glass pipette remained constant for 8 hours, another 0.5-psi pressure was added to increase the inlet pressure. This procedure was continued until

there was a water level change in the glass pipette. At this point, we define the pressure as the entry capillary pressure (or threshold capillary pressure). At this time, the saturation can be calculated using the following equation:

$$S_w = \frac{W_i}{W_{wet} - W_{dry}} \quad (5.3)$$

where  $W_{wet}$  and  $W_{dry}$  denote the wet weight and dry weight of the core holder, respectively;  $W_i$  is the water volume produced in the glass pipette. The pressure was recorded by the data acquisition system. The pressure and corresponding water saturation obtained is the drainage capillary pressure versus water saturation of the sample.

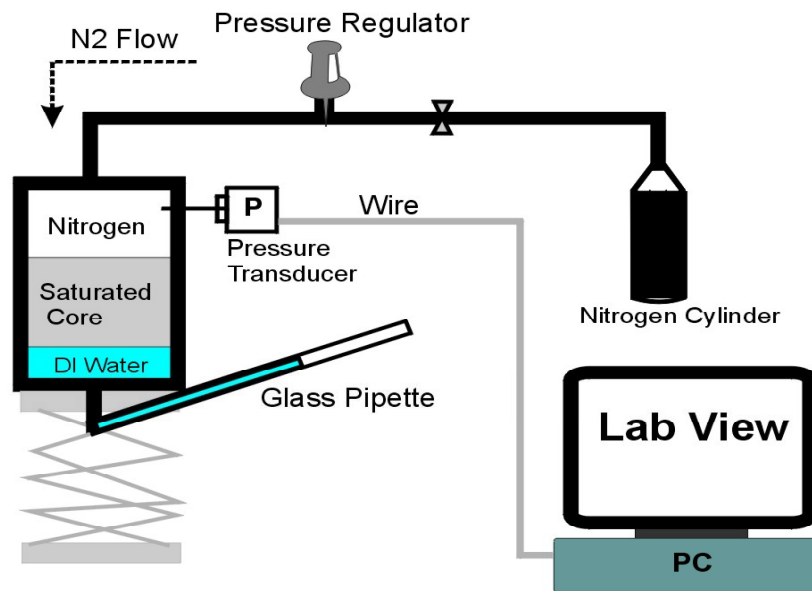


Figure 5.7: Schematic for the experiment of the air-water drainage capillary pressure.

#### **5.4 PARTIAL RESULT AND DISCUSSION**

**Imbibition:** After pressurizing the core holder, the gas bubble problem did not improve. Bubbles formed and expanded under the bottom of both the ceramic core and Berea core when the water saturation in the core was low. The formation and expansion of the bubbles are shown in Figure 5.8(a)-(c). In the ceramic core case, when the water saturation was less than 35% there was a bubble formed (Fig 5.8a), which then expanded (Fig. 5.8b), and became a gas cap that blocked the communication between water and the core (Fig 5.8c). Once blocked, the indicated capillary pressure was always zero or near zero.



(a) Bubble forms      (b) Bubbles form and expand      (c) Gas cap

Figure 5.8: The stages of the gas cap phenomenon.

When the water saturation in the ceramic core was greater than 35%, the gas cap no longer occurred, but there were still some large bubbles (similar to Fig 5.8b). The capillary pressure could be measured until this water saturation value. The accuracy of the capillary pressure value, however, may be questionable due to the existence of the bubble.

With the existence of the bubble, the imbibition air-water capillary pressure was obtained from 49% to 92% water saturation in the ceramic core. This capillary pressure curve is shown in Figure 5.9. When the water saturation was 91%, a negative capillary pressure (-0.2 psi) was measured. The injected water also broke through the core at this water saturation. This means the water saturation has exceeded the irreducible saturation,  $S_m$ .

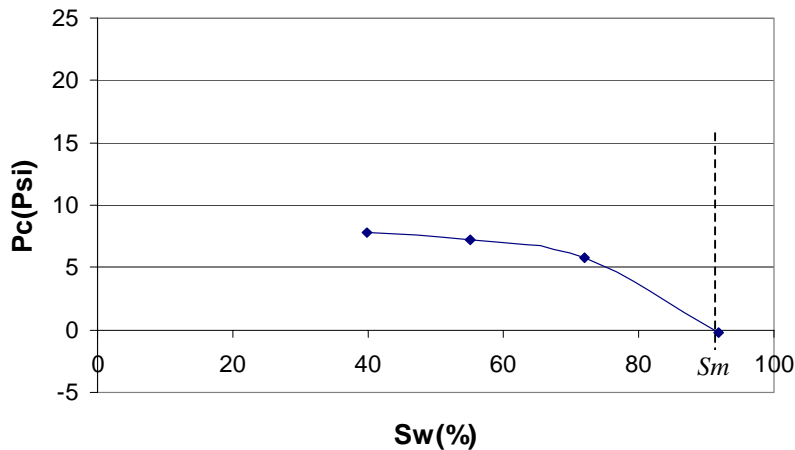


Figure 5.9: The imbibition capillary pressure of the ceramic core.

**Drainage:** The bubble problem was also encountered when the drainage experiment was conducted. During drainage, the threshold capillary pressure was measured to be 6.07 psi. However, when the pressure proceeded to 6.45 psi (85.8% water saturation), small bubbles started to form, then expanded and eventually formed a gas cap. This situation is similar to what happened in the imbibition process. The partial drainage capillary pressure values are shown in Figure 5.10.

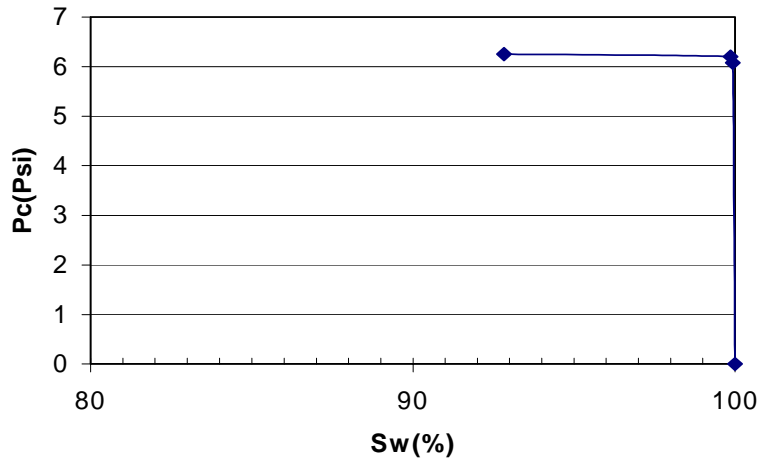


Figure 5.10: The partial drainage capillary pressure of the ceramic core.

**Discussion:** In both imbibition and drainage experiments, the existence of the bubble between the bottom of the core and the water column makes it impossible to measure the capillary pressure under a low water saturation condition. After failing when using the pressurizing method, we exclude water evaporation as a reason for the formation of the bubble. The invasion of the gas from the top of the core and the downflow of the gas inside the core appear to be the main cause of the bubble problem. This phenomenon can be explained using a tube bundle model. This model is illustrated in Figure 5.11. A bundle of tubes is used to represent a porous medium. According to Eq. 5.2, the small-radius tubes will have larger capillary pressure and the tubes with bigger radii will have smaller capillary pressure. In the low water saturation scenario, because of the surge of the capillary pressure, the gas on the top of the core flows through the biggest capillary tubes to compensate the pressure loss in the water which is assumed incompressible. This causes the formation of bubbles under the core.

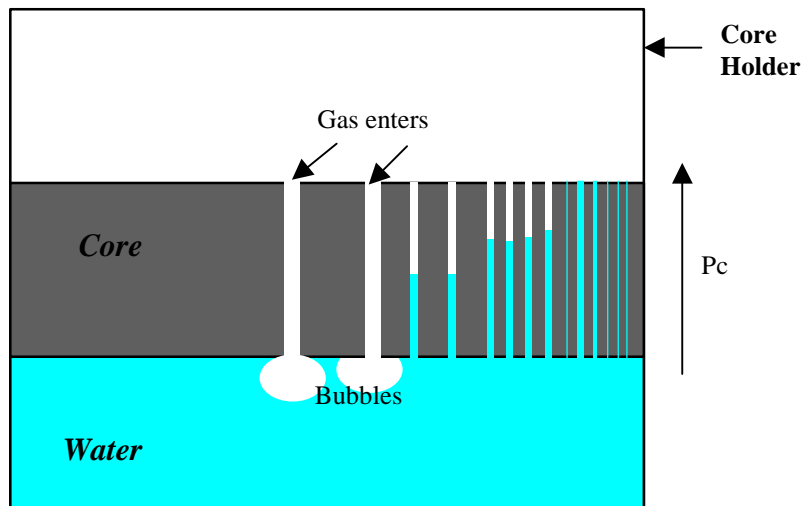


Figure 5.11: Tube bundle model to explain the formation of bubbles.

## **5.5 FUTURE WORK**

This preliminary capillary pressure experiment was unsuccessful because only a few data points could be obtained. After determining the reason for the formation of the bubble between the bottom of the core and the water column, it is important to consider this effect in subsequent experiment design. The future work will focus on finding appropriate methods and designing new apparatus to measure both air-water and steam-water capillary pressure in geothermal rock.

Further research will also focus on the theoretical surface chemistry and thermodynamics governing air-water and steam-water capillary interfaces.



## **6. EXPERIMENTAL INVESTIGATION OF RELATIVE PERMEABILITY IN FRACTURES**

This project is being conducted by Research Assistant Gracel P. Diomampo, Research Associate Kewen Li and Prof. Roland Horne. The goal is to gain better understanding of steam-water flow through fractured media and determine the behavior of relative permeability in fractures.

### **6.1 THEORETICAL BACKGROUND**

Geothermal reservoirs are complex systems of porous and fractured rocks. Complete understanding of geothermal fluid flow requires knowledge of flow in both types of rocks. At present, the governing flow mechanism for multiphase flow in fracture is still undetermined. There are two approaches commonly used in modeling multiphase flow in fractures, the porous medium approach and the equivalent homogeneous single-phase approach.

The porous medium approach treats fractures as connected two-dimensional porous media. In this model, a pore space occupied by one phase is not available for flow for the other phase. A phase can move from one position to another only upon establishing a continuous flow path for itself. As in porous media, the competition for pore occupancy is described by relative permeability and governed by Darcy's law. Darcy's law for single-phase liquid system is:

$$q_l = \frac{k_{abs}(p_i - p_o)}{\mu_l L} \quad (6.1)$$

where subscript  $l$  stands for the liquid phase,  $i$  for inlet and  $o$  for outlet;  $\mu$ ,  $p$ ,  $L$ ,  $q$ ,  $k_{abs}$  are the viscosity, pressure, fracture length, Darcy flow velocity and absolute permeability respectively. The Darcy flow velocity is equal to

$$q = \frac{Q}{bw} \quad (6.2)$$

with  $Q$  as the volumetric flow rate,  $b$  the fracture aperture and  $w$  as the fracture width. Absolute permeability of the fracture is a function only of the fracture aperture (Witherspoon et al., 1980) as described in the cubic law

$$k_{abs} = \frac{b^2}{12} \quad (6.3)$$

For liquid phase in two-phase flow, Eqn. (6.1) becomes

$$q_l = \frac{k_{abs}k_{rl}(p_i - p_o)}{\mu_l L} \quad (6.4)$$

where  $k_{rl}$  is the relative permeability of the liquid phase.

Similarly, Darcy's law derived for single-phase isothermal gas flow in porous media (Scheidegger, 1974) is

$$q_g = \frac{k_{abs}(p_i^2 - p_o^2)}{2\mu_g L p_o} \quad (6.5)$$

with the subscript  $g$  pertaining to the gas phase.

In two-phase flow, Eqn. (6.5) becomes

$$q_g = \frac{k_{abs} k_{rg} (p_i^2 - p_o^2)}{2\mu_g L p_o} \quad (6.6)$$

with  $k_{rg}$  as the gas relative permeability. The sum of the  $k_{rl}$  and  $k_{rg}$  indicates the extent of phase interference. A sum of relative permeabilities equal to one means the absence of phase interference. Physically this implies each phase flows in its own path without impeding the flow of the other. The lower is the sum of the relative permeabilities from unity the greater is the phase interference.

Relative permeability functions are usually taken to be dependent on phase saturation. The two most commonly used expression for relative permeability for homogeneous porous media are the X-curve and Corey curve (Corey, 1954). The X-curve takes relative permeability as linear function of saturation

$$k_{rl} = S_l \quad (6.7)$$

$$k_{rg} = S_g \quad (6.8)$$

where  $S_l$  and  $S_g$  are the liquid and gas saturation respectively. The Corey curve relates relative permeability to the irreducible or residual liquid and gas saturation,  $S_{rl}$  and  $S_{rg}$

$$k_{rl} = S^{*4} \quad (6.9)$$

$$k_{rg} = (1 - S^*)^2 (1 - S^{*2}) \quad (6.10)$$

$$S^* = (S_l - S_{rl}) / (1 - S_{rl} - S_{rg}) \quad (6.11)$$

The equivalent homogeneous single-phase approach treats flow through fracture as a limiting case of flow through pipes. In this model, phase velocities in a fracture are equal and capillary forces are negligible. A continuous flow path is not required for movement of each phase. A phase can be carried along by one phase as bubbles, slug or other complex structures. As in pipes, flow can be described by the concept of friction factors and using averaged properties (Fourar et al., 1993)

$$(p_i - p_o) = \frac{\Pi f \rho_m V_m^2}{2A} \quad (6.12)$$

where  $\Pi$  is the fracture perimeter,  $A$  is the cross sectional area to flow,  $\rho_m$  average density and  $V_m$  as average flow velocity. The average density is describe by

$$\rho_m = \frac{\rho_g Q_g + \rho_l Q_l}{Q_g + Q_l} \quad (6.13)$$

The average flow velocity is equal to

$$V_m = \frac{Q_g + Q_l}{A} \quad (6.14)$$

The friction factor,  $f$ , is derived empirically as a function of the averaged Reynolds number calculated by

$$N_{Re} = \frac{2bV_m\rho_m}{\mu_m} \quad (6.15)$$

with  $\mu_m$  as average viscosity

$$\mu_m = \frac{\mu_g Q_g + \mu_l Q_l}{Q_g + Q_l} \quad (6.16)$$

There are several expressions used to relate friction factor and Reynold's number. The commonly used one for flow through fracture is the generalized Blasius form (Lockhart and Martinelli, 1949):

$$f = \frac{C}{N_{Re}^n} \quad (6.17)$$

with  $C$  and  $n$  as constants derived from experimental data.

The validity of the two models for multiphase flow through fractures is still uncertain.

## **6.2 LITERATURE REVIEW**

Only a few published data are available for two-phase flow in fractures. Most of the studies have been done for air-water system or for water-oil system. Earliest is Romm's (1966) experiment with kerosene and water through an artificial parallel-plate fracture lined with strips of polyethylene or waxed paper. Romm found a linear relationship between permeability and saturation,  $S_w = k_{rw}$ ,  $S_{nw} = k_{rnw}$  such that  $k_{rw} + k_{rnw} = 1$ . Fourar et al. (1993) artificially roughened glass plates with beads and flowed air-water between them. Fourar and Bories (1995) did similar experiments using smooth glass plates and clay bricks. Both studies observed flow structures like bubble, annular and fingering bubbles comparable to flow in pipes and depicted flow in fractures to be better correlated using the equivalent homogeneous single-phase model. Pan et al. (1996) observed the identical flow structures in their experiment with oil-water system. They observed that a discontinuous phase can flow as discrete units along with the other phase. Pan et al. (1996) also found their experimental pressure drop to be better predicted by homogenous single-phase model. All of these experiments show significant phase interference at intermediate saturations.

Pruess and Tsang (1990) conducted numerical simulation of flow through rough-walled fractures. They modeled fractures as two-dimensional porous media with apertures varying with position. Their study shows the sum of the relative permeabilities is less than 1, residual saturation of the nonwetting phase is large and phase interference is greatly dependent on the presence or absence of spatial correlation of aperture in the direction of flow. Persoff et al. (1991) did experiments on gas and water flow through rough-walled fractures using transparent casts of natural fractured rocks. The experiment showed strong phase interference similar to the flow in porous media. The relative permeability data of Persoff (1991) and Persoff and Pruess (1995) for flow through rough-walled fractures were compared in Horne et al (2000) against commonly used relative permeability relations for porous media, the X-curve and Corey curve. as shown in Figure 6.1.

In both experiments of Persoff (1991) and Persoff and Pruess (1995), flow of a phase is characterized by having a localized continuous flow path that is undergoing blocking and

unblocking by the other phase. Recent parallel plate experiments by Su et al. (1999) illustrate the same flow mechanism of intermittent localized fluid flow. Kneafsey and Pruess (1998) observed similar intermittent flow in their experiments with pentane through various parallel plate models made from glass, sandblasted glass or transparent fracture replicas. These observations are contrary to the findings of Fourar et al (1993), Fourar and Bories (1995), and Pan et al. (1996).

Presently, the mechanism of flow and the characteristic behavior of relative permeability in fractures are still undetermined. Issues such as whether a discontinuous phase can travel as discrete units carried along by another phase or will be trapped as residual saturation as in porous medium are unresolved. The question of phase interference i.e. is the relative permeability curve against saturation an X-curve, Corey or some other function is still unanswered. The main objective of this study was to contribute to the resolution of these issues. Experiments on flow through smooth-walled fractures have been done first for air-water flow with the aim of establishing a reliable methodology for flow characterization and permeability calculation. Subsequently these experiments will be done with a steam-water system; and with rough-walled fractures.

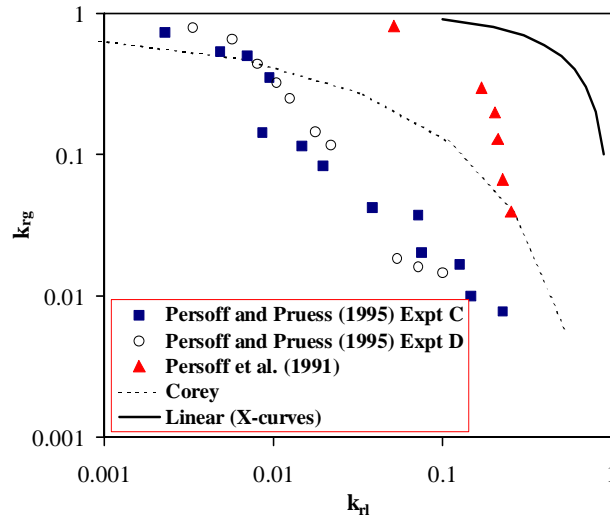


Figure 6.1: Some measurements of air-water relative permeabilities in rough-walled fractures (from Horne et al., 2000).

### **6.3 EXPERIMENTAL APPARATUS AND MEASUREMENT TECHNIQUES**

#### **Fracture Apparatus Description**

The fracture apparatus is a smooth glass plate on top of an aluminum plate. The whole apparatus is confined by another metal frame bolted to the bottom plate. This was done to improve the seal and to prevent deformation of the glass due to system pressure. The metal frame has several windows and a mirror attached to it for flow visualization. (See Figure 6.2 and Figure 6.3.)

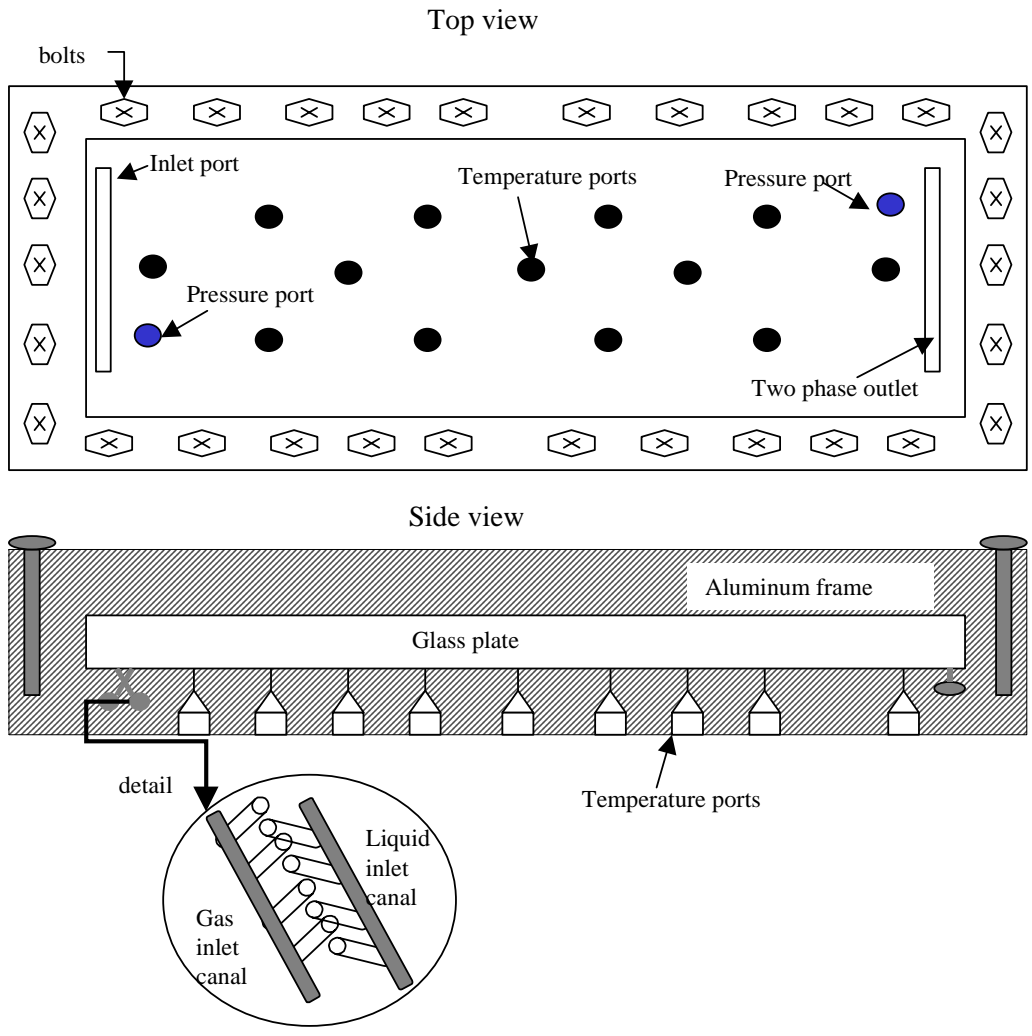


Figure 6.2: Schematic diagram of fracture apparatus.



Figure 6.3: Picture of fracture apparatus.

An O-ring (Viton 1/8" thick #2-272) was placed in between the glass and aluminum plate as a seal (see orange color lining in Figure 6.3). Placing this O-ring in the channel was not enough to provide good seal because the channel was custom made in width and length. Thinly cut rubber sheets were placed at the outer boundary to push the O-ring to the sides of the aluminum plate. These provided an excellent seal when compressed with the glass and metal frame. Since the O-ring is cylindrical in shape and the aluminum plate is rectangular; there will be a narrow channel in between the O-ring and the plate when squeezed together. A thin lining of copper based adhesive (Permatex Ultra Copper) was applied to minimize this channel. It is important to eliminate this channel for it serves as an easy conduit for the fluid to pass through instead of the fracture.

The phases enter to the fracture through two separate canals. Each canal has several ports drilled in a way that they align on the surface (See Figure 6.2). The surface of the fracture apparatus was designed such that there is an available 12" by 4" space for flow. Through out this flow area, tiny temperature ports the size of needles were drilled. Needle-size ports were drilled so as to minimize surface discontinuity. A pressure port was drilled at each end of the flow path. The two-phase fluid exits through a single outlet.

### **Control and Measurement Techniques**

There are two available canals for input of gas and liquid. The options to input nitrogen and water as separate streams or as mixed fluid in a single stream were tried. It was found that mixing the gas and water prior to input caused no significant improvement in fluid distribution. Thus, the gas and water streams were injected separately for simplicity, ease of flow rate control and inlet pressure reading.

Gas injection was controlled through a flow regulator (Matheson Flow Controller Model 8270). The gas regulator was connected to a gas meter (Matheson Flow Meter model 8170) that gives out a digital display. For water, a meter pump (Constameter pump model III) controlled the rate of injection. Distilled, deaerated water was used as the injection fluid. Red dye was dissolved in the water for better phase identification.

Nitrogen and water enters at the far left of the apparatus. Both phases flow in between the glass and aluminum plate and exit at the far right through a single channel. Attached to the exit is a cross of larger diameter that enables the separation of the phases for outlet pressure measurement. Figure 6.4 is a schematic diagram of this configuration.

Low-capacity differential transducers were used to measure the gas-phase pressure drop, liquid-phase pressure drop and the gas-phase outlet pressure. The liquid differential transducer (Celesco Transducer Model CD 10D range 0-5psi) is attached to the input water stream and to the bottom of the cross separating the phases at the outlet. The gas differential transducer (Celesco Transducer Model CD 10 D range 0-5psi) is screwed together in the nitrogen inlet and to the top of the cross separator. Another gas transducer (Celesco Transducer Model CD 10D range 0-0.5psi) is attached to the top of the cross separator. This last transducer measures the outlet pressure of the gas. These transducers

send electrical signals to a Labview program designed to record pressure data at user-specified time intervals. See Figure 6.4.

Experience has shown that these fracture experiments are unsteady state by nature. At a single gas-water input ratio, there is significant pressure fluctuations accompanied by saturation changes and change in gas flow rate (see Section 0). The water flow rate is considered constant since it is injected by meter pump. Due to this nature, data acquisition then requires gathering instantaneous pressure, flow rate and saturation data.

Instantaneous data gathering was accomplished by the use of a digital video camera. Video shots were taken of the pressure, flow rate and saturation data displayed all at the same time. The pressure data were displayed by voltmeters. The voltmeters are attached to each transducer outlet electrical wire. The digital output of the gas meter displays the gas flow rate. The saturation is taken from the image of the whole flow area of the fracture. Still images are then taken from the recorded video film. The data gathered from the video is connected with the Labview data through the time read from a digital clock recorded along with the other data. Figure 6.5 shows a typical video image taken from the experiments. See also Figure 6.4.

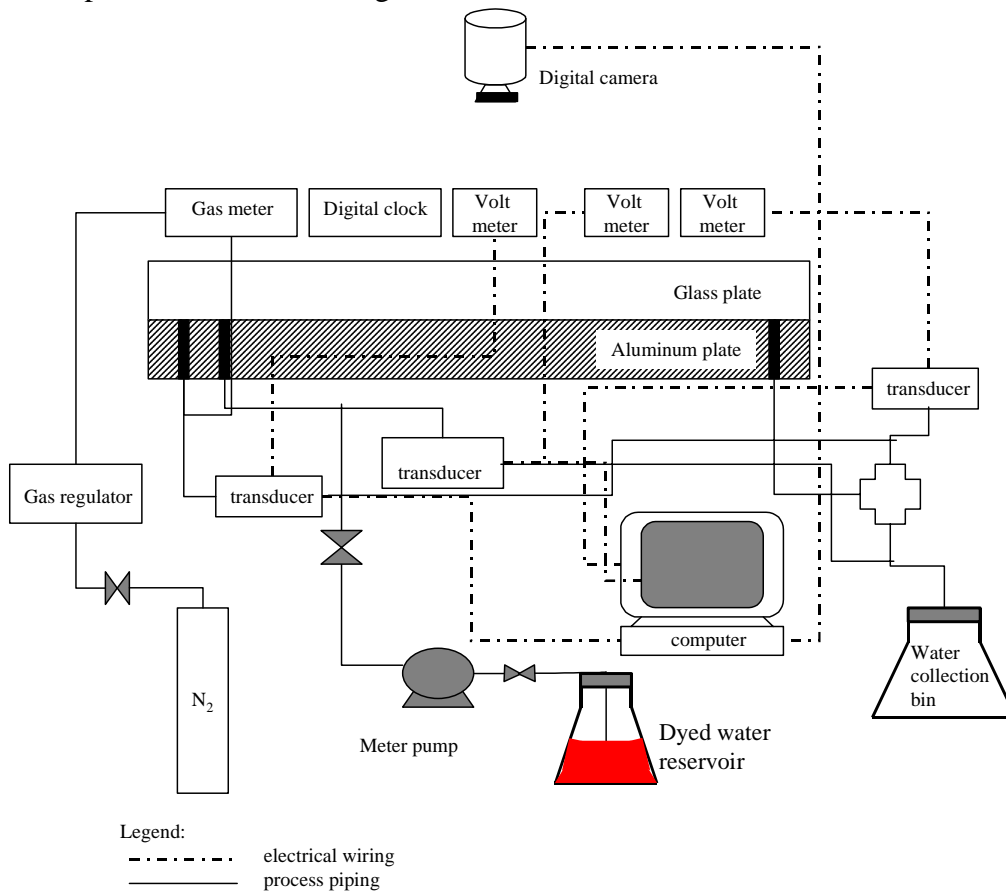
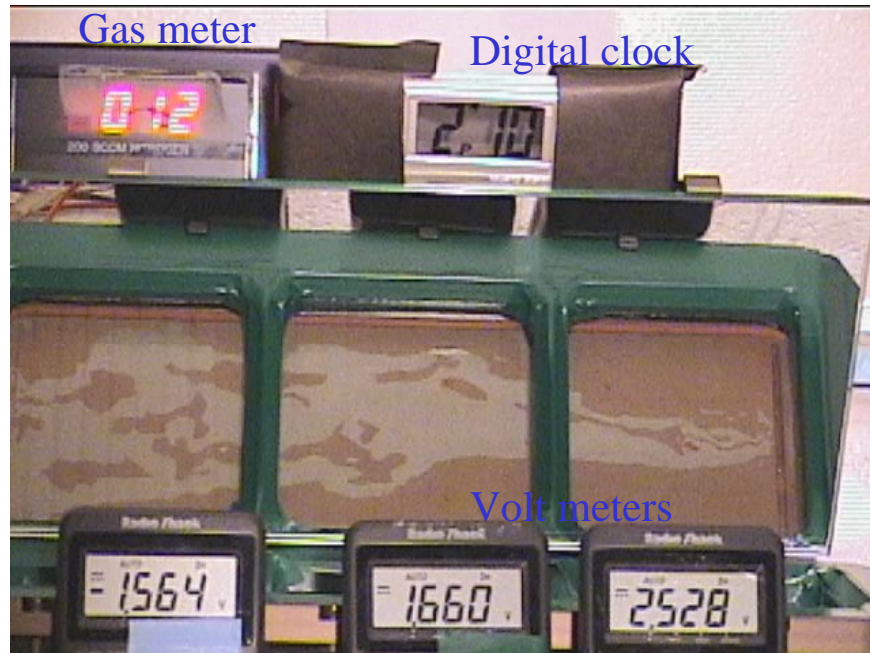


Figure 6.4: Process flow diagram for Nitrogen-Water experiment.



*Figure 6.5: Sample video image taken for nitrogen-water runs.*

Drainage and imbibition experiments were done for smooth- and for rough-walled fractures. The glass against the aluminum plate represented the smooth-walled fracture while the rough-walled fracture was created by inserting a wire mesh in between the glass and aluminum plate. The wire mesh is made from 0.00065" (0.0026cm) diameter stainless steel wire and has 30x30 mesh size. For both the rough- and smooth-walled fracture configurations, stainless steel shims were inserted in the perimeter of the flow area. The 0.003" (0.0076cm) thick shims were placed in between the glass and aluminum plate.

Drainage experiments were performed first. To start, the fracture was made fully saturated with water. Unlike in porous media, parallel plates can be easily saturated with water if the aperture is small enough. Full saturation was achieved simply by flowing water at slow rate on completely dried apparatus. This was true for both the smooth- and rough-walled configurations. The drainage experiment proceeded with the water injected at a constant rate and gas rate increased incrementally. If saturation change was not evident, then both the gas and the water rate were changed. The reverse was done for imbibition. At a specific gas-water ratio, the experiment was made to run for several minutes (usually 30 minutes) or up to time when the pressure change was minimal or when pressure fluctuations seemed to be in a certain range before taking video record.

### **Saturation Measurement**

From the still image of the fracture flow shown in Figure 6.5, saturation was computed by measuring the area that each phase occupied. The photographs were processed in a Matlab program. The program first cuts the photograph to display just the image of the flow area. Using this cut image, the program does quadratic discriminant analysis to group the pixels of the picture into three groups: the water phase, gas phase and the

frame. The grouping is based on color differences. Saturation is calculated as total pixels of liquid group over the sum of the gas and liquid group. Figure 6.6 is a comparison of the gray-scaled image produced by the program and the original cut photograph from the digital camera. The accuracy of the program in calculating the saturation can be related to the similarity in details of the gray scale image to the true image. From the figure, it can be said that the program has reasonable accuracy.

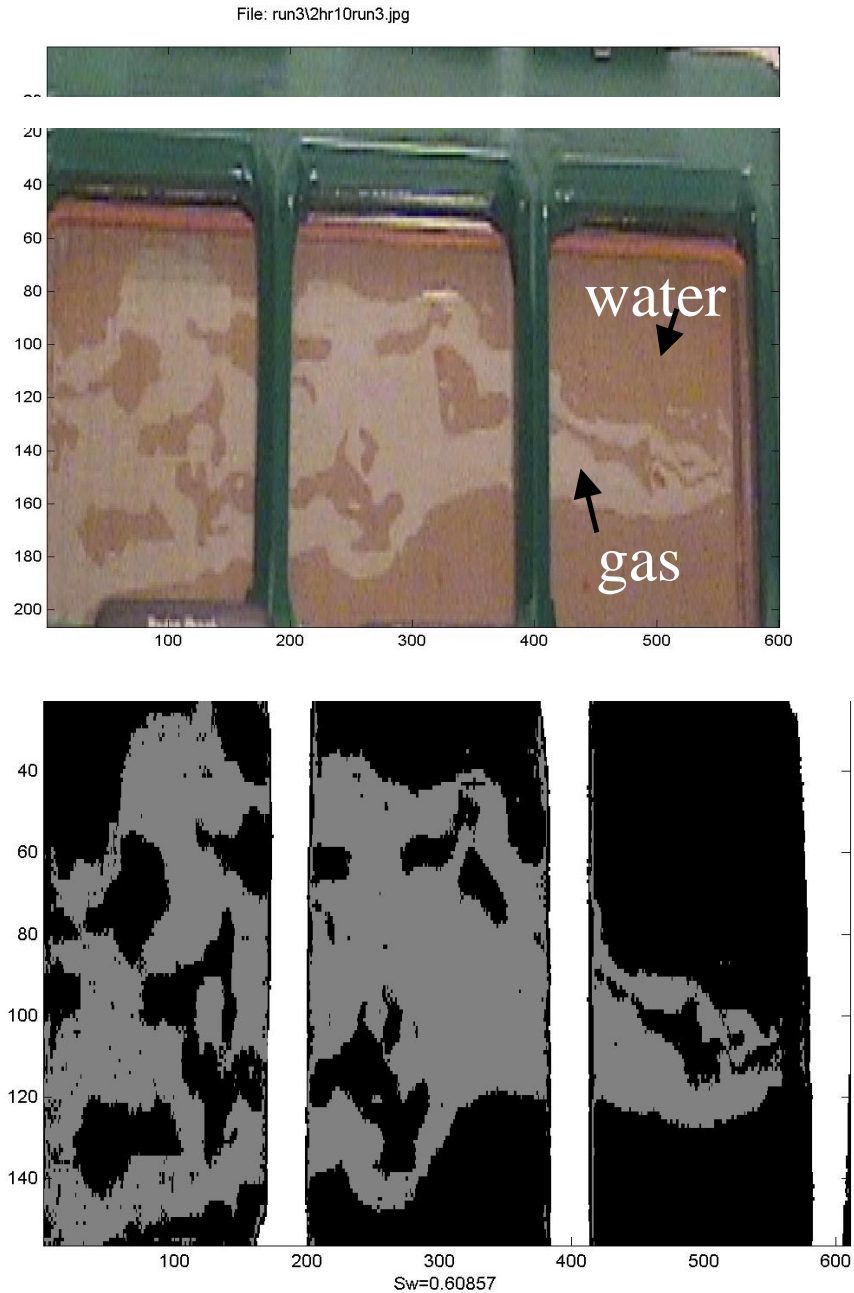


*Figure 6.6: Comparison between the true color image of the fracture flow and gray scale image from Matlab program used in measuring saturation.*

Pan et al. (1996) also used this technique for measurement of saturation. This study noted that the sources of error in this technique were the quality of the photographs and the water film adsorbed on the surfaces of the plates with the latter being of minimal effect. Good quality photographs are the ones with clear distinction between the gas and liquid phase. The use of dyed liquid enhanced visualization of phase boundaries. Good lighting is also necessary so that the colors in the image come out clear. The lighting should also be positioned in a way that it does not produce shadow on the flow area. The program will mistakenly take the shadow as liquid phase even if there is gas. It should be not too bright or focused too directly on the image to prevent reflection. Reflection will cast a white background on the picture. This will be taken automatically by the program as gaseous phase. In the experiment, good lighting was obtained by taking the picture in the dark with lamps directed on white ceiling to create adequate lighting on the apparatus.

## **6.4 RESULTS AND DISCUSSION**

### **For Smooth Wall Fracture Experiments**

#### ***Observed Flow Mechanism***

One dominant flow mechanism was observed in the smooth-walled fracture experiment. Each phase travels through the fracture by forming localized continuous flow path. This flow path is unstable as the other phase constantly blocks and unblocks certain points in the path.

For example in drainage experiment, the gas forms its own flow path through the liquid-dominated fracture. This flow path undergoes continuous snapping and reforming due to the invasion of water. This blocking and unblocking of flow path causes continuous pressure fluctuations throughout the experiment even at a constant gas-water ratio. Figure 6.7 shows the pressure fluctuations and the corresponding events observed. Snapshot images of the flow at these times are seen in Figure 6.8. These pictures were taken at gas rate of 19 cc/min and water rate of 8.5 cc/min. It was observed that the lower pressure drop corresponds to the time when gas is establishing its channel (see time 2:14 p.m. in Figure 6.7 and Figure 6.8). Upon establishing a complete path, gas is able to rush through the fracture length. This causes an increase in the gas pressure drop. As the gas surges, there is more space for water to come through the fracture. Water invades the gas channel (see time 2:16 p.m. in Figure 6.7 and Figure 6.8). As water breaks through there is an increase in liquid phase pressure drop. These are the pressure peaks seen in Figure 6.7. The cycle continues with the gas forming its pathway and water invading it (see time 2:17 p.m. and 2:18 p.m. in Figure 6.7 and Figure 6.8).

This flow mechanism of moving through continuous flow path was observed in a wide range of gas-water ratios from  $10^{-1}$  to  $10^4$ . The width of the flow path increases as gas rate increases. This flow path, however, was continuously being broken up by the water phase and reforming again. Figure 6.9 illustrates some examples.

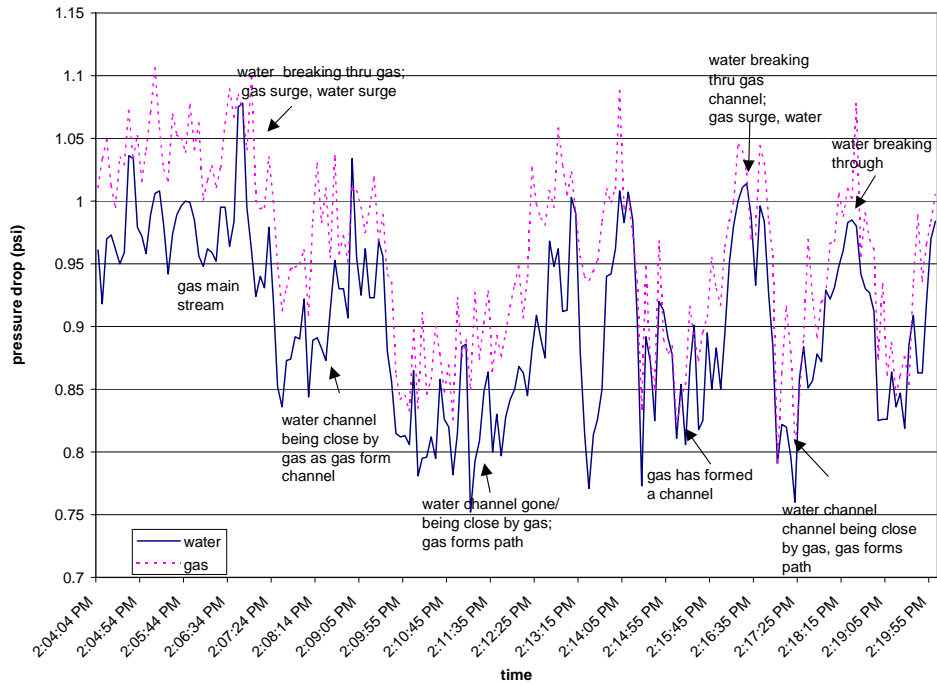


Figure 6.7: Pressure fluctuations cause by the breaking and reforming of gas flow path.

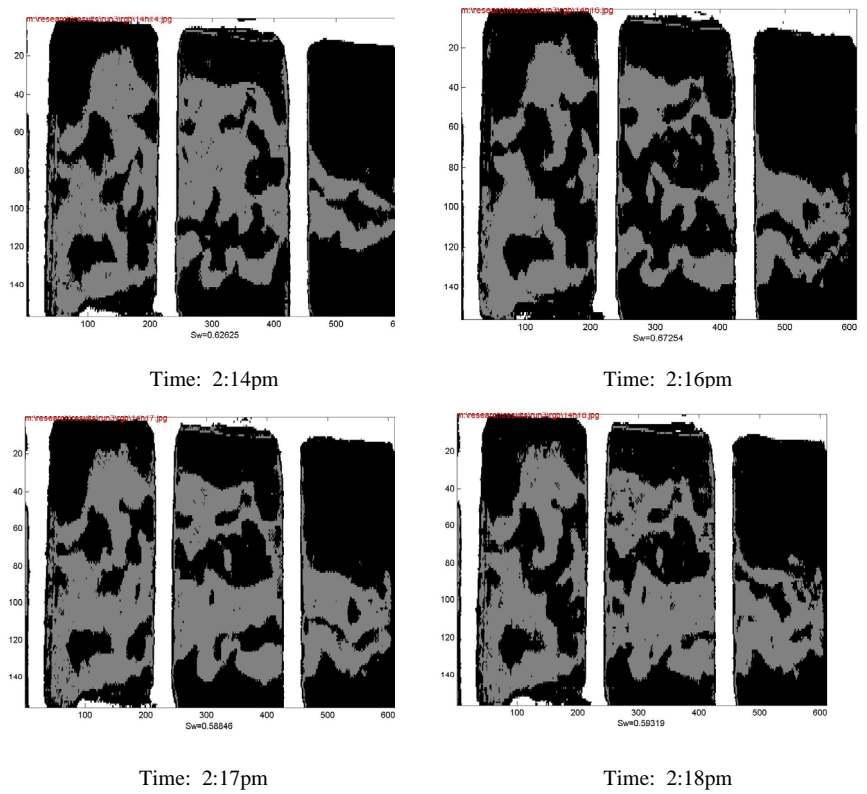
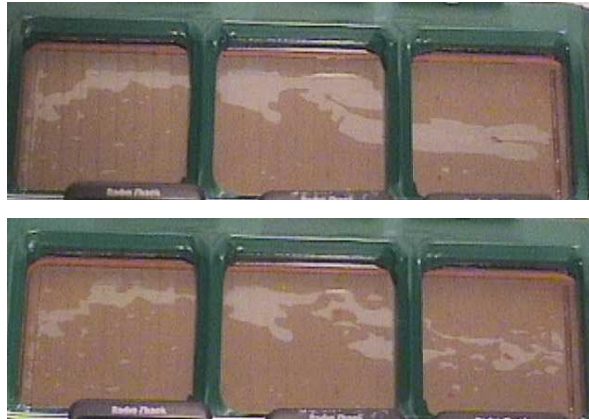


Figure 6.8 Images showing the forming and breaking of gas flow path corresponding to the time in Figure 6.7.

Gas rate: 0.5 cc/min water rate 8.5 cc/min



Gas rate: 19 cc/min water rate 8.5 cc/min



Gas rate: 140 cc/min water rate 8.5 cc/min



*Figure 6.9: Examples of gas flow path increase in width as gas flow rate increases and water breaking up this flow path.*

This flow mechanism shows the unsteady nature of the experiment. Even at constant gas and liquid injection rates, the pressure fluctuates and saturation changes as fracture space changes from being a gas path to water path and vice versa. This emphasizes the importance of acquiring instantaneous pressure, saturation and flow rate measurements.

Persoff and Pruess (1995) observed a similar flow mechanism in their experiment also with air-water flow in a transparent fracture replica. They also correlated the pressure fluctuations with the blocking and unblocking of flow path. They modeled the flow as flow through a cylindrical tube of constant radius with a certain critical throat point of radius very much smaller than the tube. Through their model they were able to prove that a phase flow path in fractures will be unstable and will consequently be invaded by the other phase. This observation is also consistent with the findings by Su et al. (1999), Kneafsy and Pruess (1998) and numerical simulations by Pruess and Tsang (1990) where the flow mechanism was described as intermittent localized flow.

Intermittent localized flow observation is contrary to that of the concept of moving "islands" or flow structures carried by one phase as observed by Fourar and Bories (1995), Fourar et al. (1993), and Pan et al. (1996). The superficial velocities for the smooth wall experiment are graphed on Fourar and Bories (1995) flow pattern map in Figure 6.10. Although the data covered a wide range of the proposed flow patterns, these flow patterns were not seen here. The intermittent localized flow observed is more comparable to flow in porous media. Phases in the experiment moved only through continuous phase paths, like in porous media. But unlike in porous media, the phase paths or occupancy are not constant but are rapidly changing and reforming.

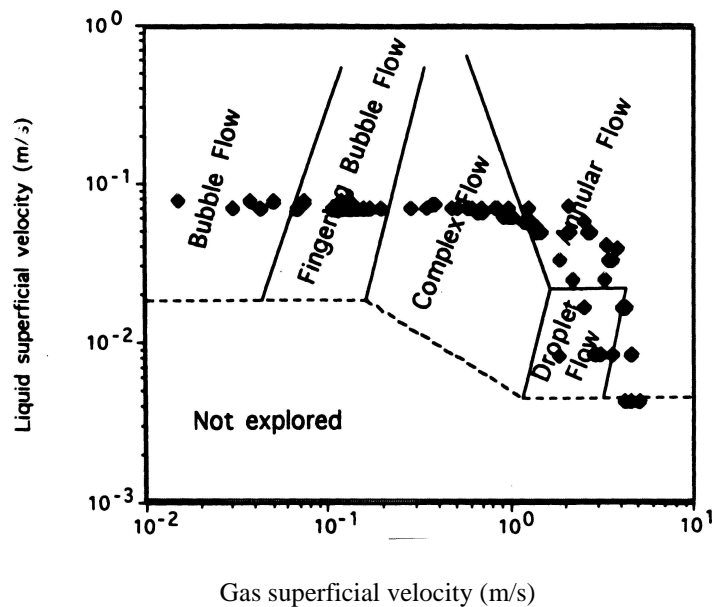
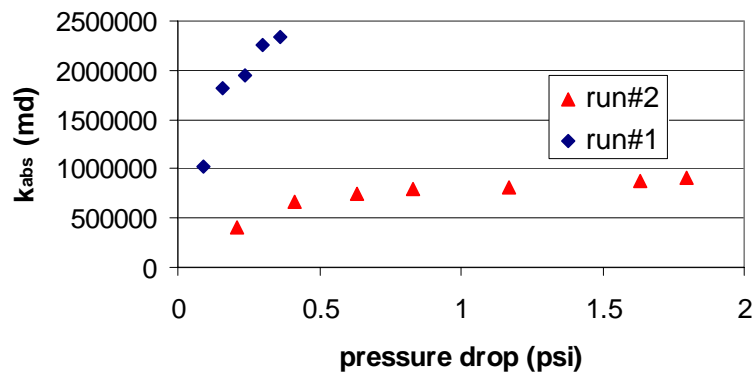


Figure 6.10: Smooth wall fracture experimental velocity data imposed in Fourar and Bories (1995) flow map for a glass channel.

### ***Relative Permeability Curve From Porous Medium Approach***

Eqn. (6.4) and Eqn. (6.5) for two-phase Darcy flow were used to calculate relative permeabilities. The use of these equations requires the knowledge of the fracture absolute permeability. The absolute permeability was derived using Eqn. (6.1) with the pressure drop and flow rate coming from single-phase liquid experiments.

Two single-phase experiments were done. The results of these are illustrated in Figure 6.11. Run #1 was done in sequence with the smooth wall experiments. After noticing that the absolute permeability changes with flow rate. Run #2 was done several weeks later with a different pump to investigate a wider flow rate range. Both runs show that for pressures below 0.5 psi,  $k_{abs}$  is changing with flow rate. This implies that the fluid is lifting the glass as it flows through the fracture. At pressures greater than 0.5psi, the glass is lifted to its maximum height defined by the confinement of the metal frame. At this pressure range, the absolute permeability is constant. All the data points in the experiment lie in this range of constant absolute permeability. However, the results of the two experiments were conflicting in terms of magnitude. The choice of which absolute permeability to use will affect the magnitude of the calculated relative permeability. This will not affect the shape of the relative permeability curve. The highest absolute permeability derived from Run #1 was used.



*Figure 6.11: Absolute fracture permeability derived from single-phase liquid experiments for the smooth-walled fracture.*

The results are graphed in Figure 6.12. In this figure, neglecting the data enclosed in blue square box, the relative permeability curve has the shape of the Corey curve (Corey, 1954). This follows with the observation that the flow in smooth-walled fractures is comparable to flow in porous media. It is also noticeable that the sum of the relative permeabilities at a particular saturation is less than unity. This indicates phase interference. This is consistent with the observed flow mechanism where the gas and water compete in establishing pathways through the fracture.

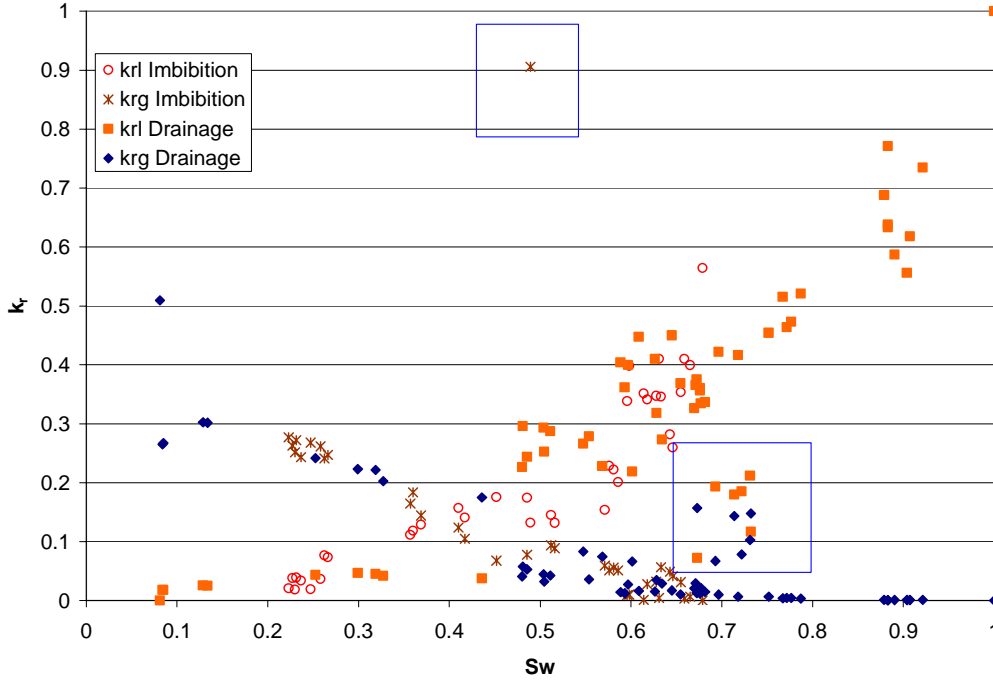


Figure 6.12: Relative permeability data obtained from the smooth-walled fracture experiment.

The data for both imbibition and drainage experiments were fitted separately with the Honarpour et al. (1982) expression:

$$k_{rw} = k_{rwo} \left[ \frac{(S_w - S_{wr})}{(1 - S_{wr} - S_{gr})} \right]^{n_w} \quad (6.18)$$

$$k_{rg} = k_{rgo} \left[ \frac{(1 - S_w - S_{gr})}{(1 - S_{wr} - S_{gr})} \right]^{n_g} \quad (6.19)$$

with

$$k_{rwo} = k_{rw}(S_{wi}) \quad (6.20)$$

$$k_{rgo} = k_{rg}(S_{wr}) \quad (6.21)$$

$S_{wi}$  being the initial water saturation for drainage while for imbibition

$$k_{rwo} = k_{rw}(S_{gr}) \quad (6.22)$$

$$k_{rgo} = k_{rg}(S_{wi}) \quad (6.23)$$

The resulting curves are graphed in Figure 6.13 and Figure 6.14. The parameters for the fitted curves are tallied in Table 0.1. In both graphs, the fitted Honarpour curves give good representation of the trend of relative permeability data with saturation. The fitted curves suggest different exponents in the Honarpour expression for imbibition and drainage cases. This is even though the data for both drainage and imbibition seem to lie on the same trend as seen in Figure 6.12. This shows the effect of saturation history on relative permeability. Compared to the Corey expression from Eqn. (6.9) and (6.10), the

drainage experiments have dissimilar exponents. For imbibition, however, the value of  $n_w$  (4.57) and  $n_g$  (1.92) are close to Corey exponents of 4 for  $n_w$  and 2 for  $n_g$ .

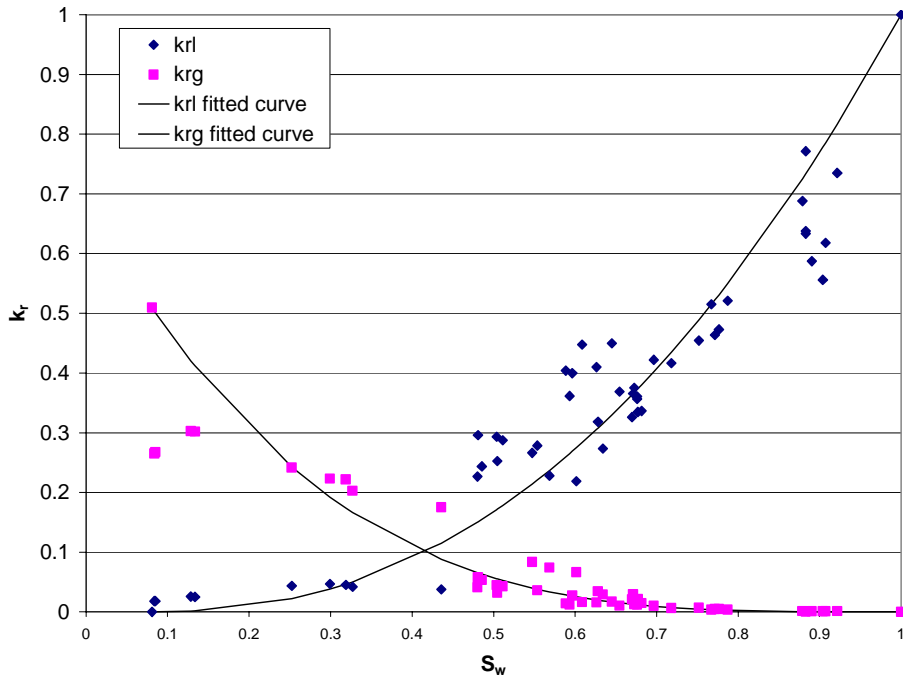


Figure 6.13: Fitted Honarpour expression for the smooth-walled fracture drainage experiment.

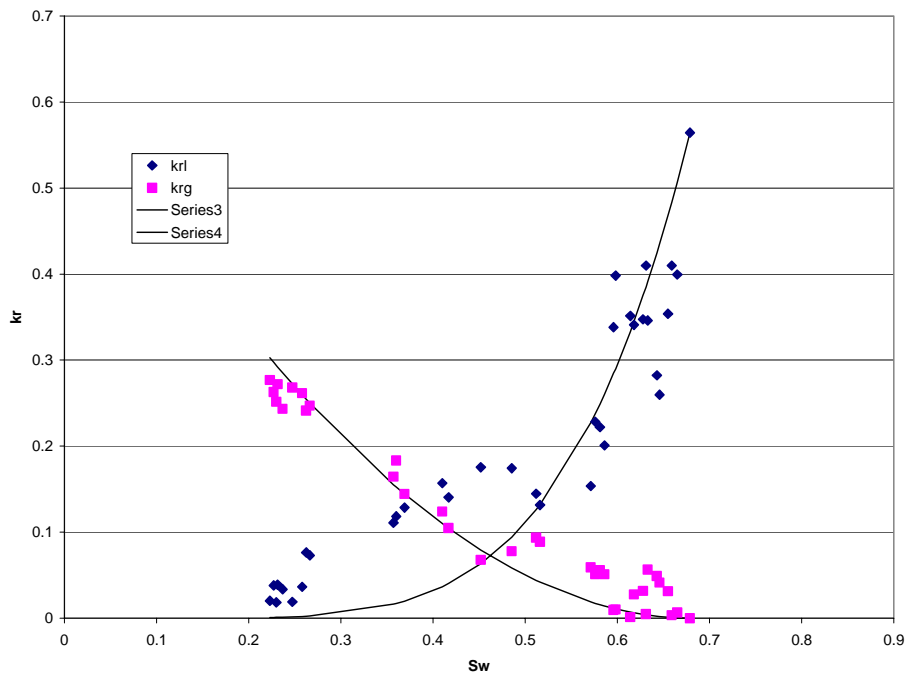


Figure 6.14: Fitted Honarpour expression for the smooth-walled fracture imbibition experiment.

Table 6.1: Fit parameters for the smooth-walled fracture experiment.

	Drainage	Imbibition
Swr	0.081	0.081
Sgr	0	0.321
krwo	1	0.564
krgo	0.509	0.509
nw	2.27	4.57
ng	3.59	1.92

### *Application of Homogeneous Single-phase Pipe Flow Model for The smooth-walled fracture*

The homogeneous single-phase pipe flow model was also applied to the data for the smooth-walled fracture. Figure 6.15 depicts the calculated friction factor with the modified Reynold's number in a log-log chart. From the fitted linear equation, the constants  $C$  and  $n$  in Eqn. (6.17) are 3.23 and 0.75 respectively. Figure 6.16 compares this result to previous works for parallel plate experiments. The slope of the fitted line (-0.75) is lower than the usual finding of negative unit slope for laminar flow. But among all the studies, the data is closer to that of Romm (1966).

The fit of Eqn. (6.17) for friction factor as a function of Reynold's number with the experimental data is not so good. Thus, pressure drop calculated from Eqn. (6.12) inadequately predicts the experimental data (see Figure 6.17). This was expected since the observed flow mechanism was not similar to the flow regimes in pipes on which this model is based.

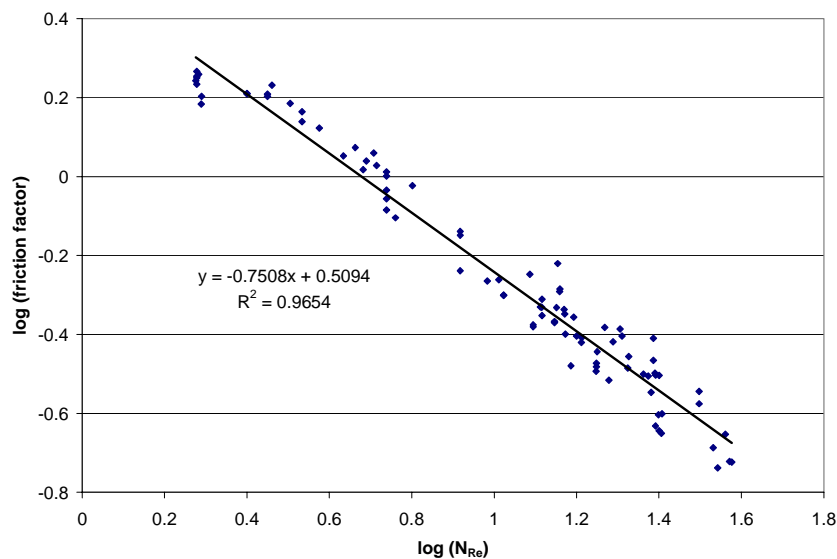


Figure 6.15: Natural logarithm of friction factor with natural logarithm of Reynold's number from data of the smooth-walled fracture experiment.

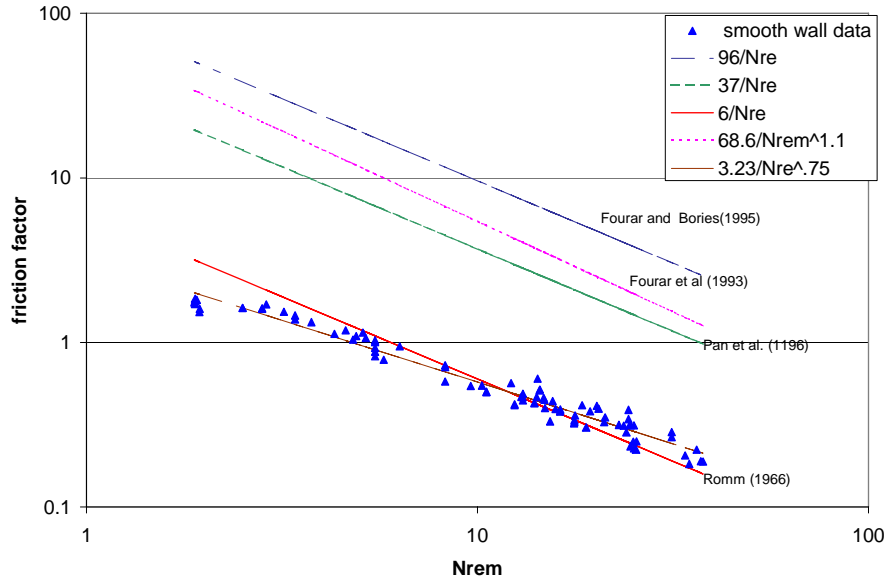


Figure 6.16: Friction Factor against modified Reynold's number for smooth-walled fracture in comparison to previous works.

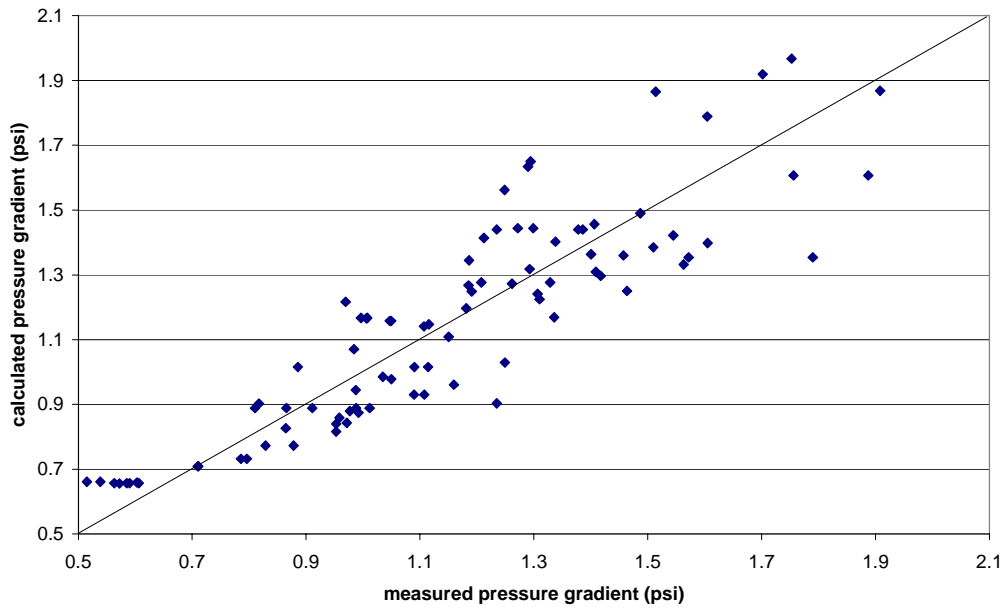


Figure 6.17: Comparison of the predicted pressure drop from homogeneous model and measured data for smooth-walled fracture.

## **Rough-Walled Fracture Experiments**

### ***Observed Flow Mechanism***

Similar to the smooth-walled fracture experiments, during drainage in the rough-walled fracture experiment a phase moves by establishing a continuous flow path for itself. However, the stability of a phase path varies greatly with gas-water ratio.

At low gas-water ratio, the gas invades the liquid-dominated fracture and establishes a path (see Figure 6.18). The path is wider than that in the smooth-walled fracture at the same gas-water ratio. This may be because the mesh gives the gas a way to move horizontally in the fracture even at low gas-water ratio. This path is very unstable; water quickly invades it almost completely leaving a few scattered residual gas areas. The residual gas areas left are not enough to establish a path. Thus, after the invasion of water the fracture can be said to return to its liquid-dominated condition. Within this liquid-dominated condition, the gas will again construct its own flow path and the cycle continues. Figure 6.19 shows two examples of gas flow channels, the water invasion that proceeds it and the residual gas areas left after the water invasion.

The formation of the gas path and the consequent water invasion again goes along with pressure fluctuations. Figure 6.20 shows the pressure data for Figure 6.18 and picture set (A) in Figure 6.19. As in the smooth-walled fracture (see section 0), the low pressure drop corresponds to the forming of the gas path, followed by a peak in both gas and liquid pressure related to the surge of the two fluids through the fracture. It was observed that the magnitude of the pressure peaks decrease as the gas-water ratio increases.

The diminishing magnitude of the pressure fluctuations relates to the point when the gas has established a stable path. With a stable path, gas can travel more smoothly and surge flow does not occur. Without surge flow, large pressure fluctuations are not observed. Stable gas paths were reached at high gas-water ratio. As in the smooth-walled fracture, the stable gas channels increase in width with increasing gas-water ratio (see Figure 6.21). Within these established gas paths, water sometimes forms narrow channels but these channels are unstable. Water flow is mostly at the edge of the gas path. In the ratios of stable phase paths, saturation can be considered constant at one gas-water injection rate.

For the imbibition experiment, two flow mechanisms were observed. At low gas-water ratio, a stable flow path of phases was seen (see Figure 6.22). This stable flow path is similar to that seen in the smooth-walled fracture and in the drainage experiment for the rough-walled fracture. At high gas-water ratio (50 and above), a wave-like flow similar to flow in pipe was observed. In this flow, water travels like a wave or a steady front covering the entire fracture. This wave flow caused increase in the pressure drop exceeding the maximum of the pressure transducer. Thus, the magnitude of the pressure drop when a wave front occurs can be higher than 5psi. Figure 6.23 shows a sample of the wave-like front and its corresponding pressure peaks.

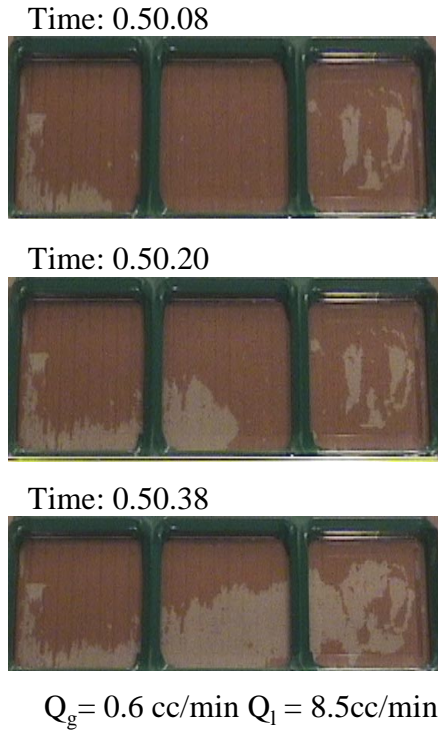


Figure 6.18: Gas invasion in drainage experiment with rough-walled fracture.

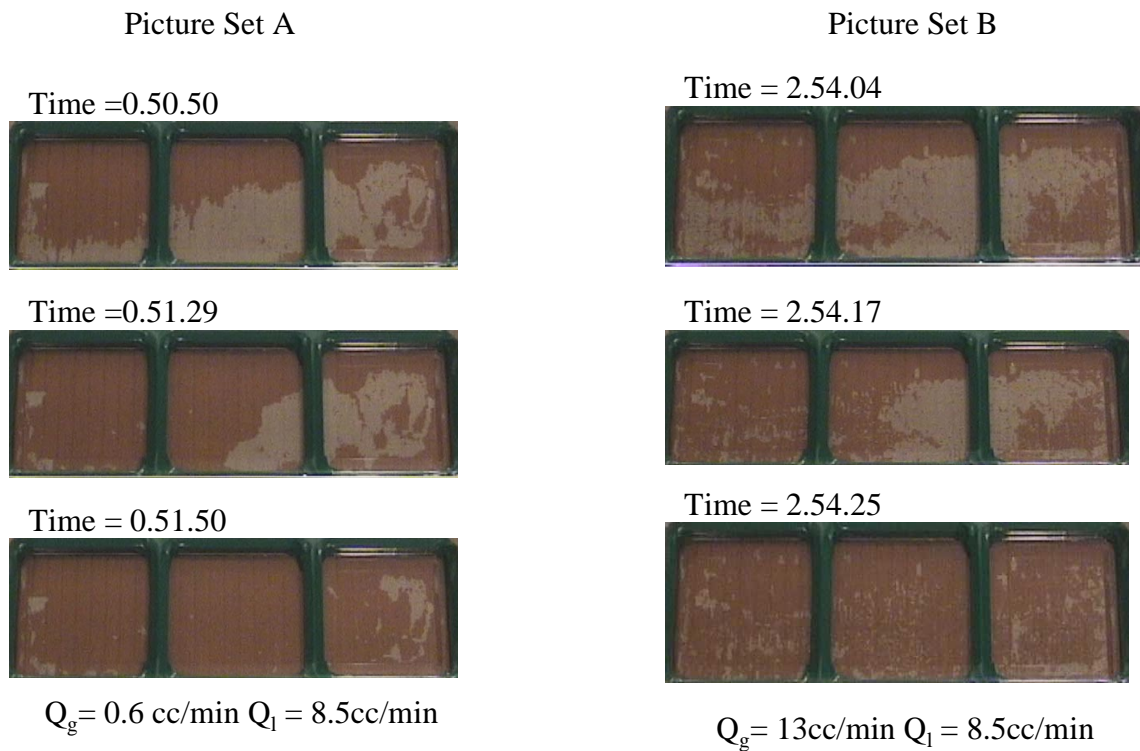


Figure 6.19: Examples of gas flow path, the invasion of water that follows and the residual gases left in rough-walled drainage experiment.

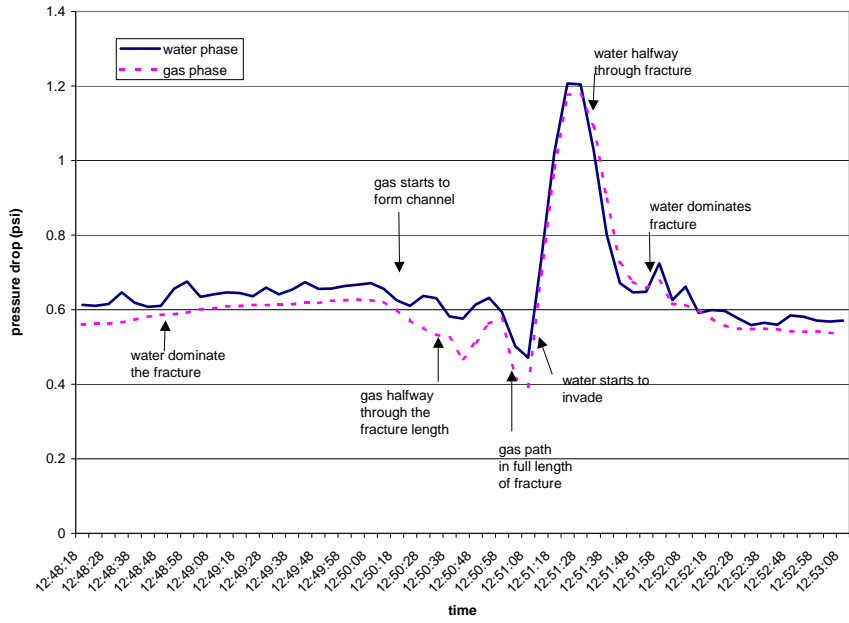


Figure 6.20: Example of pressure fluctuations caused by the building and breaking up of gas and water path. Pictures for this time span are shown in Figure 6.18 and picture set A in Figure 6.19.

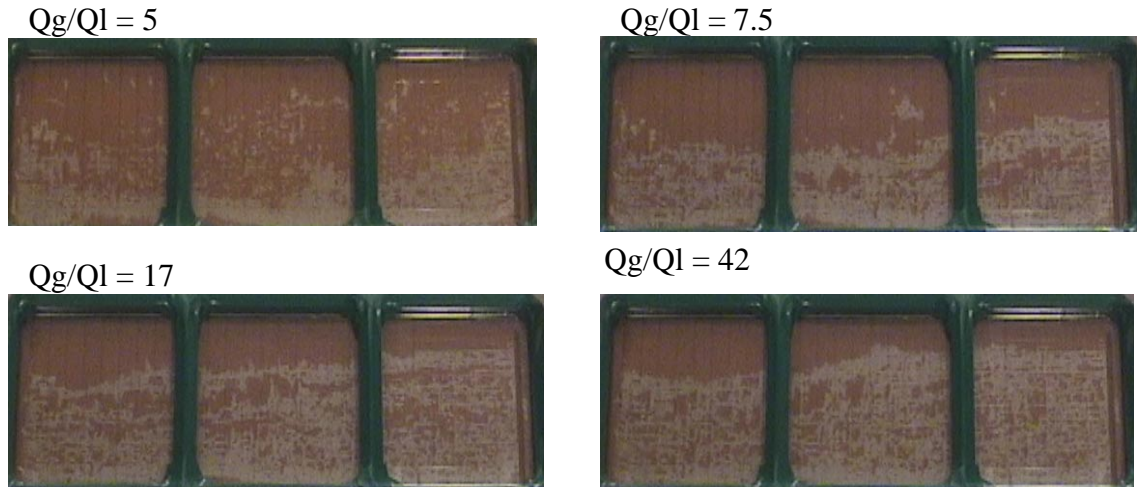
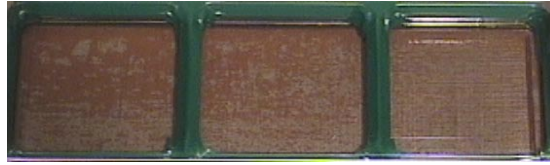


Figure 6.21: Images showing stable gas path in high gas-water ratio for the rough-walled fracture.

$Q_g = 125 \text{ cc/min}$   $Q_l = 7.5 \text{ cc/min}$



$Q_g = 50 \text{ cc/min}$   $Q_l = 9 \text{ cc/min}$

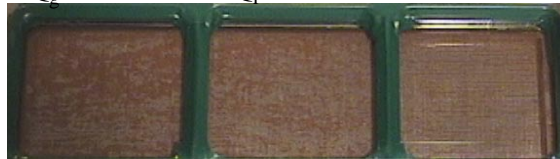


Figure 6.22: Images showing examples of stable flow path of imbibition experiment in the rough-walled fracture.

Time: 12.23.53



Time: 12.24.09



Time: 12.24.11



Time: 12.24.12



Time: 12.24.13

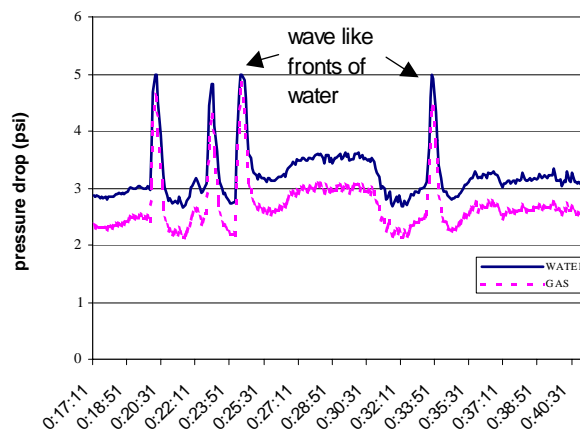


Figure 6.23: Picture of wave-like fronts seen at high gas-water ratio in imbibition experiment and the corresponding pressure peaks.

In all the experiments for the rough-walled fracture, there was considerable amount of trapped phases in the fracture as seen in the isolated red and white spots in pictures from Figure 6.18 to Figure 6.23. This is likely since the mesh provided small corners for the

wetting phase to cling to and be trapped in the gas-dominated area of the fracture. The mesh also provided a means to trap the nonwetting gas phase in the small empty space of the mesh as the water surrounds the walls.

***Relative Permeability Curve Through Porous Medium Approach***

The calculation procedure done in Section 0 for relative permeability was repeated for the data gathered in the rough-walled fracture experiments.

Several single-phase rough wall experiments were done to determine the absolute permeability of the fracture. The calculated absolute permeabilities from these experiments are shown in Figure 6.24. The reason for the variation of the absolute permeability value with pressure was discussed earlier. Like that in the smooth-walled fracture, the absolute permeability remains constant at pressures greater than 0.5 psi. Since all the data was at pressures higher than 0.5 psi, absolute permeability was taken as the average of data with pressures greater than 0.5 psi. The absolute permeability value used was 1,950 darcy.

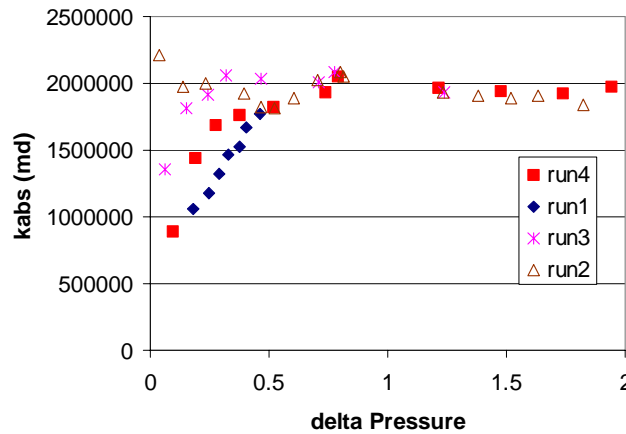


*Figure 6.24: Absolute permeability from single-phase experiments for the rough-walled fracture model.*

Figure 6.25 shows the complete data from the drainage experiment for the rough wall apparatus. This graph shows the relative permeability taken when the gas path was an unstable surging conduit and when it was a stable channel. Noticing that the flow is more comparable to porous flow when the gas has established a stable path, the data for the unstable gas surge was removed. The remaining data are seen in Figure 6.26. This figure displays a more defined trend. This indicates that the porous medium approach is more applicable to model flow through the rough-walled fracture when flow is characterized by established phase paths. It also suggests that other means of data analysis is needed for the data corresponding to unstable gas surge.

For imbibition, the calculated relative permeability for all type of flow mechanism observed is seen in Figure 6.27. The graph of relative permeability is very scattered and

shows no obvious relationship. One factor that may have caused this is the uncertainty with regards to saturation measurement for the imbibition experiment in the rough-walled fracture. The picture for the imbibition experiment has lower picture quality than the other experiments and saturation analysis was more difficult due to trapped water and gas phases scattered throughout the flow area. Figure 6.28 demonstrates how the programs for saturation measurement were unable to capture the finer details of trapped phases. This effect diminished as the stable fluid pathway was established with decreasing gas-water ratio.

The data corresponding only to flow characterized by stable fluid pathway was chosen and graphed in Figure 6.29. Although Figure 6.29 is an improvement over Figure 6.27, the association between relative permeability and saturation is still unclear. These data for imbibition are graphed along with the drainage data in Figure 6.30. This graph shows that the relative permeability for the nonwetting phase in imbibition is lower than that of drainage while the opposite is true for the wetting phase. This is consistent with studies for oil-water flow (Amyx et al., 1960) and steam-water flow (Li et al., 1999) in porous media. Amyx et al. (1960) noted that the imbibition process causes the nonwetting phase (oil) to lose its mobility at high values of wetting phase saturation while the drainage process causes the wetting phase to lose its mobility at higher values of wetting phase saturation.

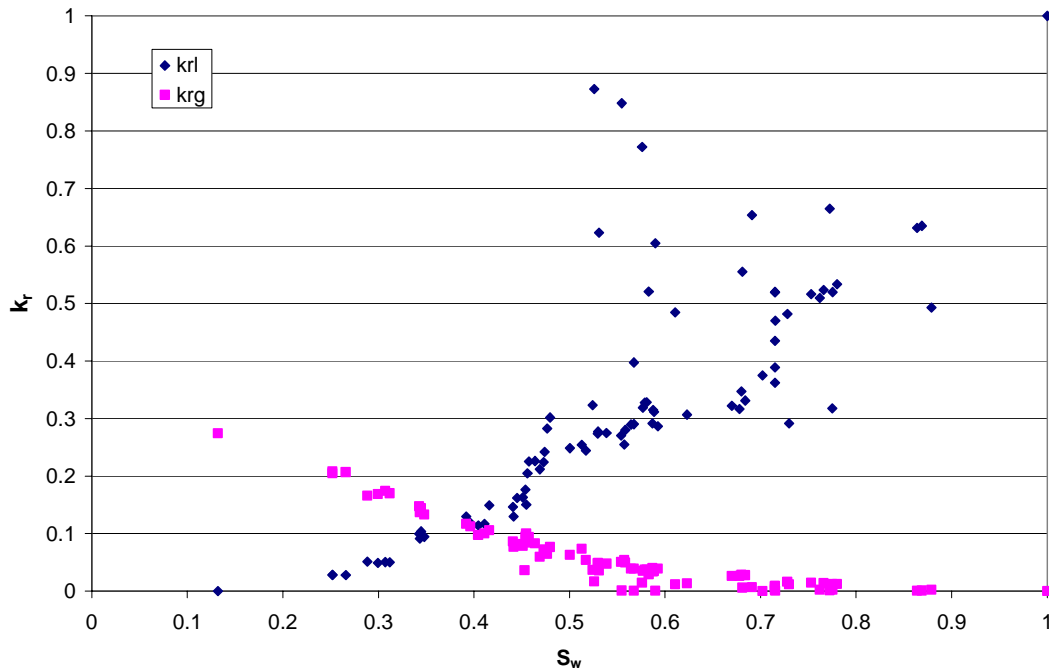


Figure 6.25: Relative permeability data for drainage experiment for the rough-walled fracture model.

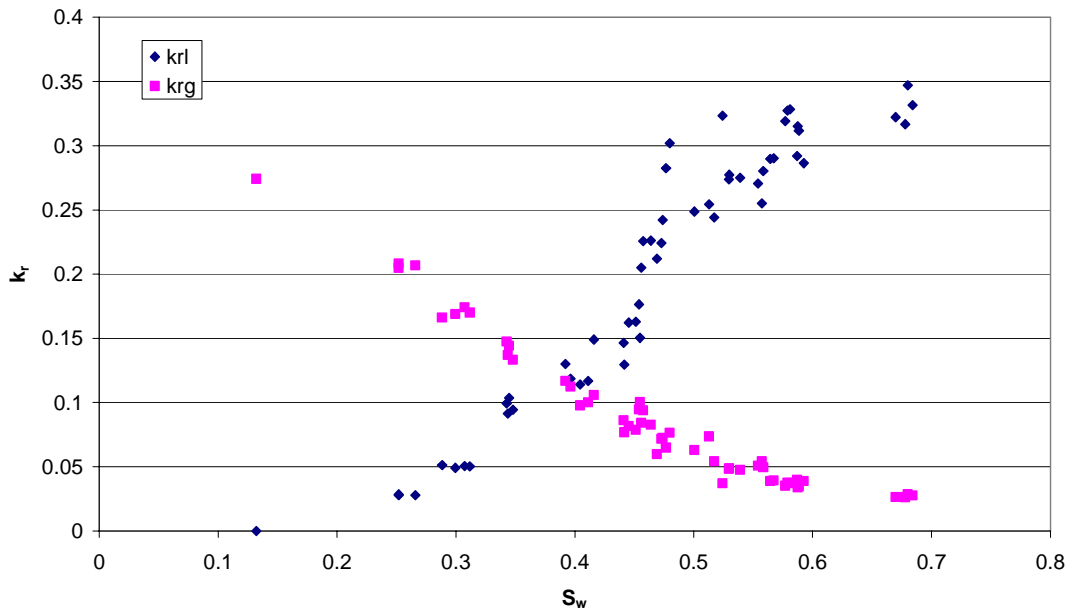


Figure 6.26: Relative permeability data for rough wall model when the gas path is stable.

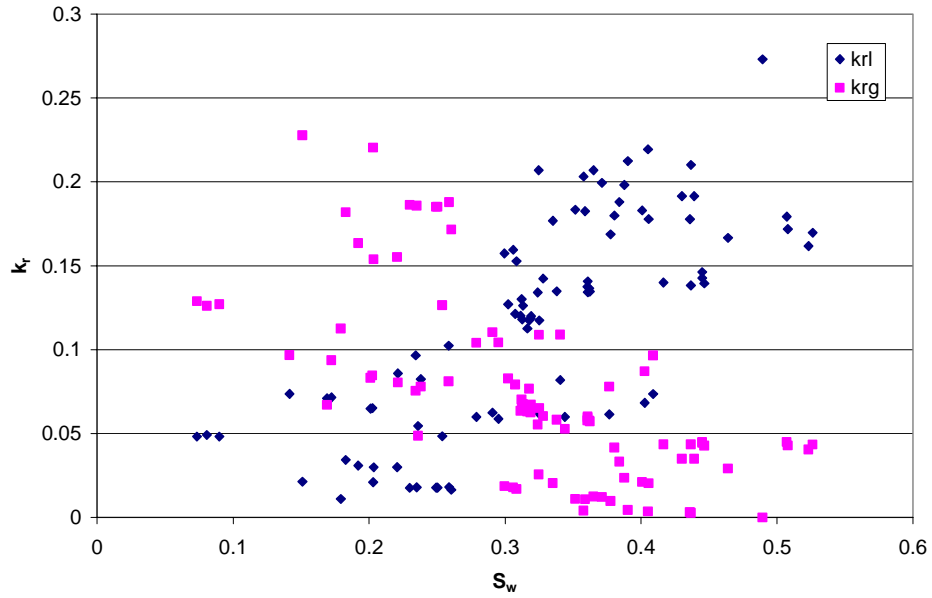


Figure 6.27: Relative permeability data for the rough-walled fracture in the imbibition experiment.

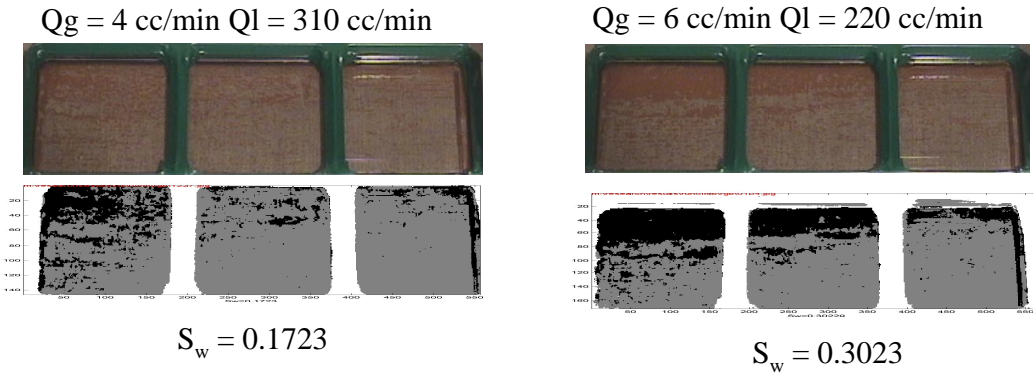


Figure 6.28: Examples of saturation measurement for imbibition experiment with the rough-walled fracture.

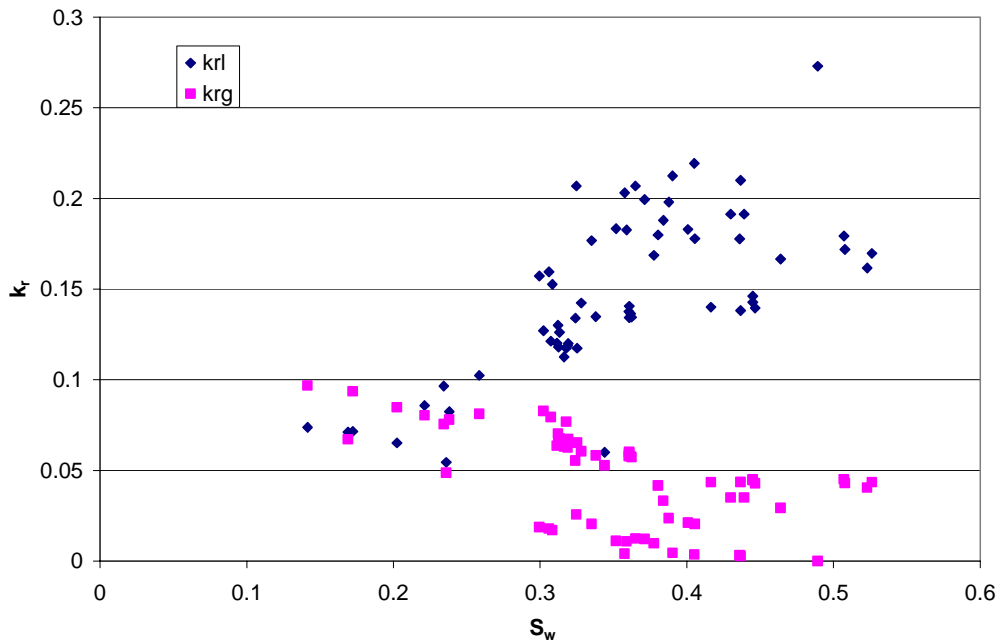


Figure 6.29: Relative permeability for rough wall imbibition experiment for flow with stable phase path.

The Honarpour relation in Eqn. (3.1) and Eqn. (3.2) was fitted to the drainage and imbibition data separately. The resulting fit parameters are tabulated in Table 6.2. As expected, there is a good fit with the drainage data but not with the imbibition data. The exponents of the fitted curves are different for imbibition and drainage and both are far from Corey values.

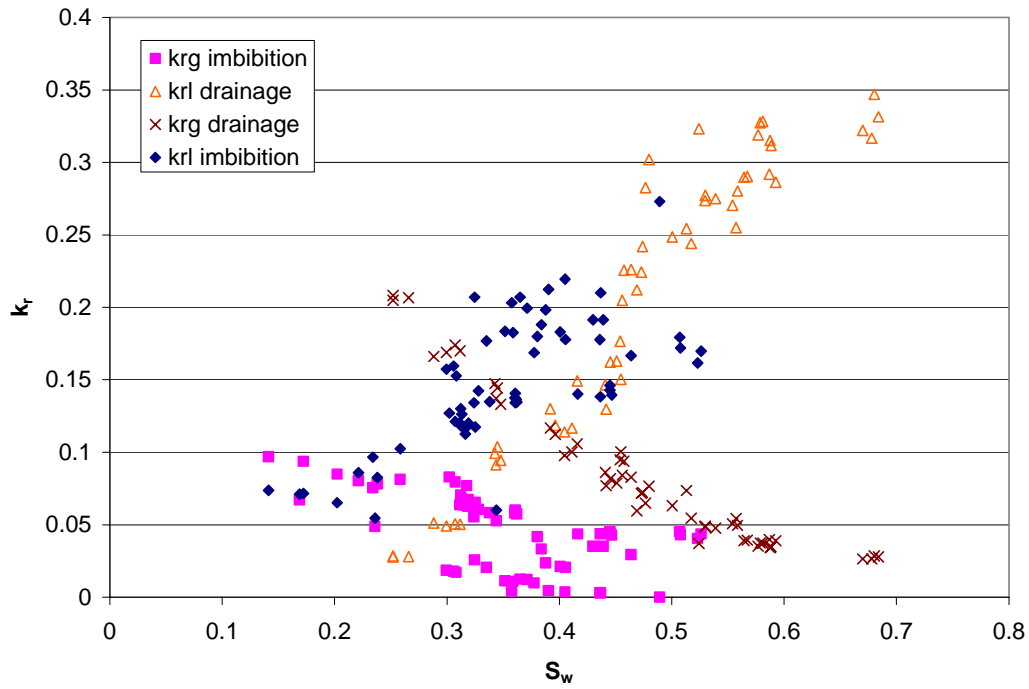


Figure 6.30: Drainage and imbibition data for the rough-walled fracture.

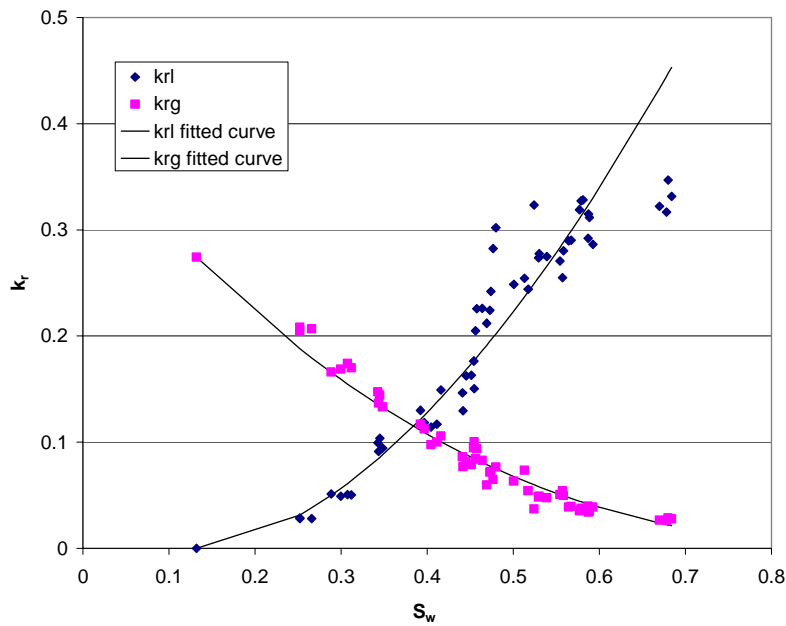


Figure 6.31: Fitted Honarpour curve for drainage data in the rough-walled fracture experiment.

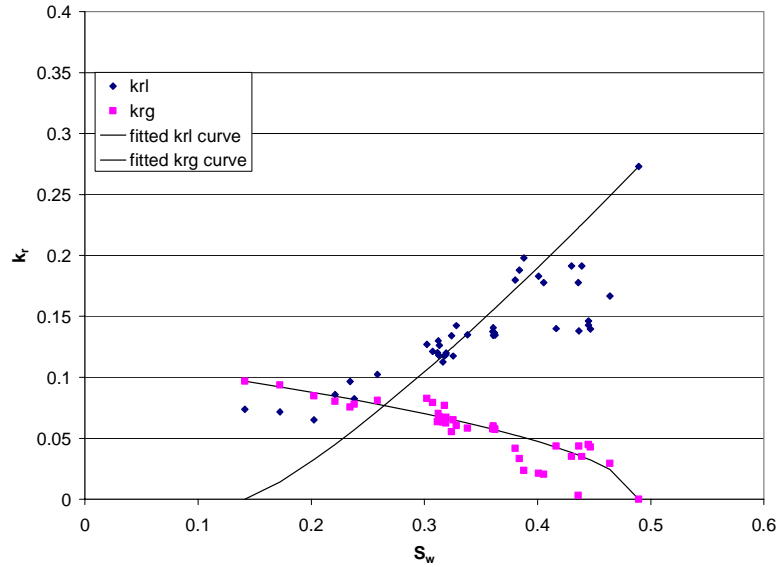


Figure 6.32: Fitted curve for imbibition the rough-walled fracture experiment.

Table 6.2: Honarpour fit parameters for rough wall experiment.

	Drainage	Imbibition
Swr	0.132	0.141
Sgr	0	0.51
krwo	1	0.27
krgo	0.274	0.1
nw	1.75	1.2
ng	2.53	0.52

### *Application of homogeneous model for the rough-walled fracture experiment*

It was discovered in the previous section that the porous medium approach when applied only when flow was characterized by stable phase paths yielded better defined relative permeability curves. This indicates that different flow mechanisms may require different mathematical approaches. Thus in the application of the homogeneous model to the rough-walled fracture experiment, the appropriateness of the model was reviewed for all data and for data corresponding only to unstable surge flow.

The natural logarithm of the calculated friction factor and Reynold's number is seen in Figure 6.33. Graph A includes all the data while graph B consists only of the data corresponding to unstable surge flow. Comparison of graphs A and B shows that removing the stable flow data removed the cluster of data points. The observation that stable flow data tend to cluster in plots of friction factor with Reynold's number suggests that the homogeneous single-phase model is not the appropriate model for this kind of flow. However, considering only the surge data as in graph B of Figure 6.33 also did not improve the goodness of fit. For both graphs, there exist some data points that lie vertically in relation to each other. This can indicate either two things: that the friction

factor may not be solely a function of Reynold's number or that Reynold's number is not a good correlation variable for friction factor in flow through fractures. The calculated friction factor and Reynold's number are compared to other studies in Figure 6.34. Again both data have slopes lower than unity and the data are closer to Romm's expression (Romm, 1966). The values for the constants  $C$  and  $n$  are listed in Table 6.3. The pressure drops calculated from these values are compared to measured data in Figure 6.35. Since the fit of the friction factor with the experimental data was not so good, the computed pressure drop from Eqn. (6.12) was not able to predict the experimental pressure gradient.

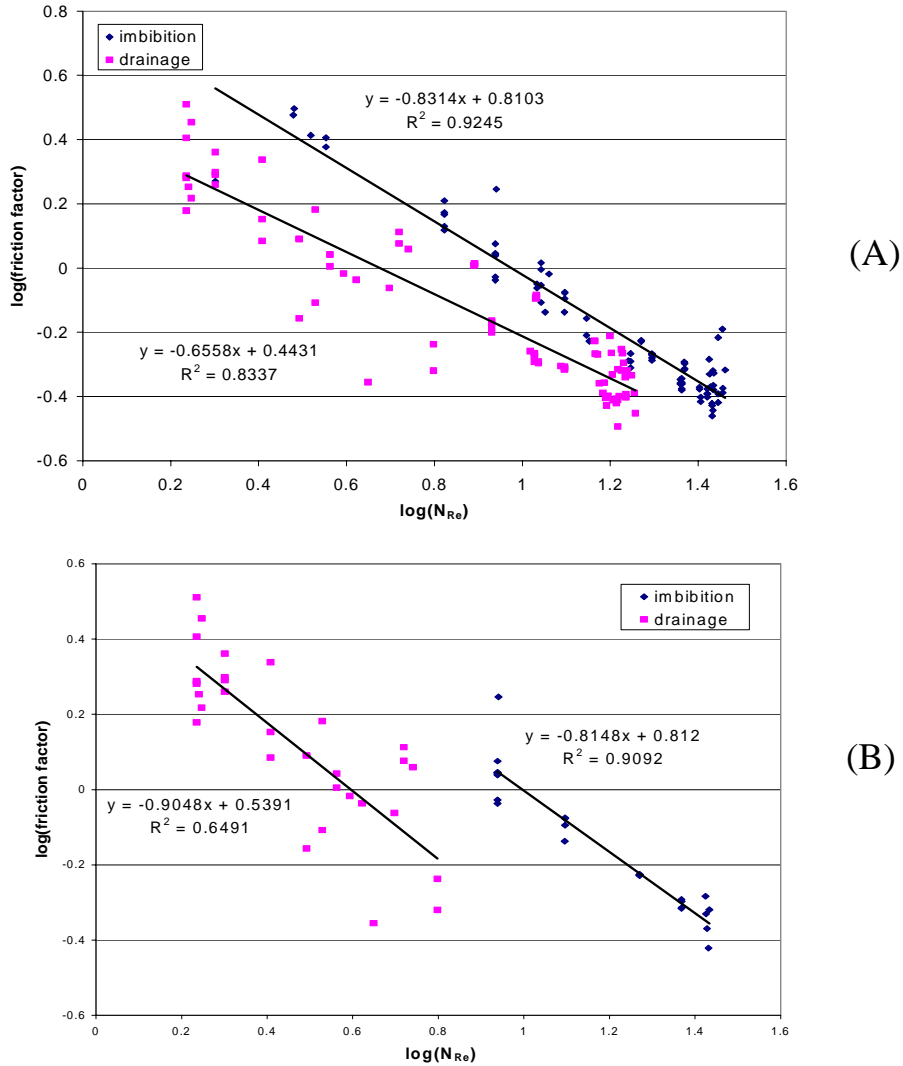


Figure 6.33: Natural logarithm of friction factor with Natural logarithm of Reynold's number for (a) all rough wall data and (b) for data with unstable surge flow.

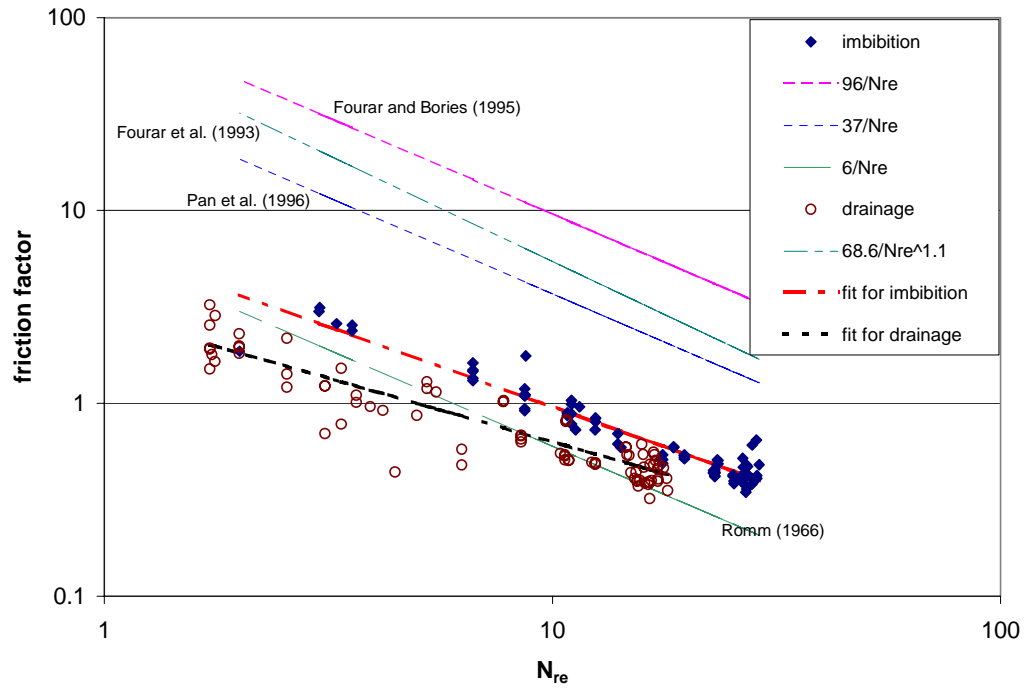


Figure 6.34: Friction factor with modified Reynold's number for rough wall experiment.

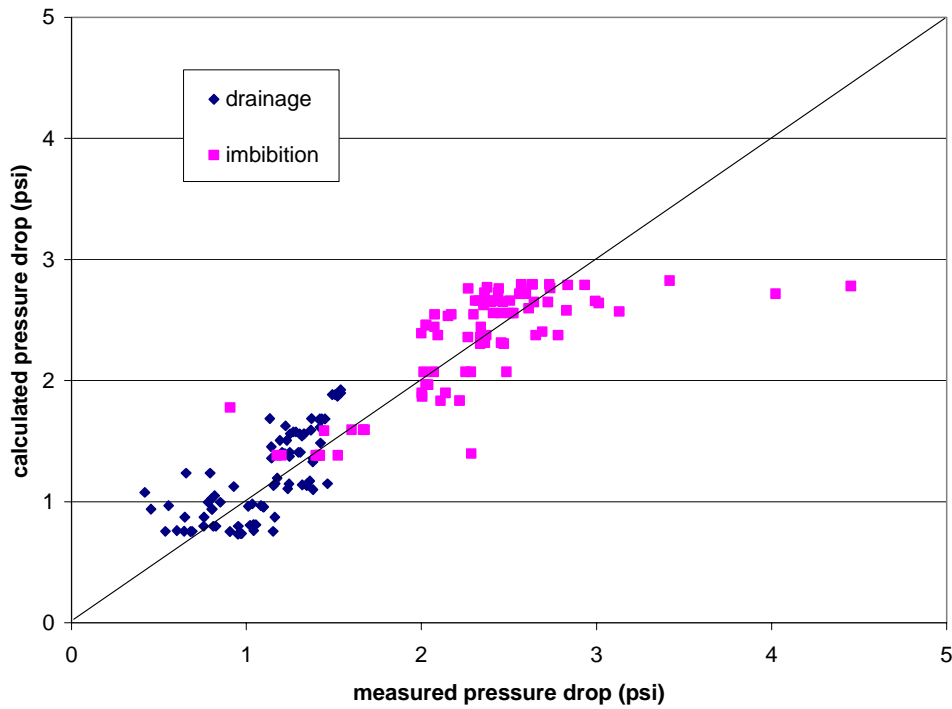


Figure 6.35: Comparison of the measured pressure drop against calculated pressure drop from homogeneous equivalent single-phase model.

Table 6.3: Homogeneous equivalent single-phase fit parameters.

Experiment	C	n
Imbibition rough wall experiment	6.5	-0.83
Drainage for rough wall experiment	2.8	-0.66
Smooth wall experiment	3.23	-0.75

### Comparison of smooth and rough wall experiment to other studies

The data for both smooth and rough wall experiments were compared to previous studies and to known correlations for porous media (see Figure 6.36). Compared to other data, the experimental values in this study were higher than those of Persoff and Pruess (1995) but lower than those of Persoff (1991). With this observation, no apparent conclusion can be made as to whether the data from this study contradict or agree with previous relative permeability experiments. However, more importantly Figure 6.36 shows that the experimental data conform mostly to the Corey type of curve. This suggests that flow through fractures can be analyzed by treating it as a limiting case of porous media flow and by using the relative permeability variable. The relative permeabilities as seen in Figure 6.36 for fractures sum up to less than one and are not in linear relationship with saturation as suggested by the X-curve. This reiterates results from previous studies that phase interference occurs in fractures. Comparing the results for smooth and rough fractures, the relative permeability values for the drainage experiments do not differ much. However, the relative permeability in the imbibition experiment on the rough-walled fracture is lower than these two experiments.

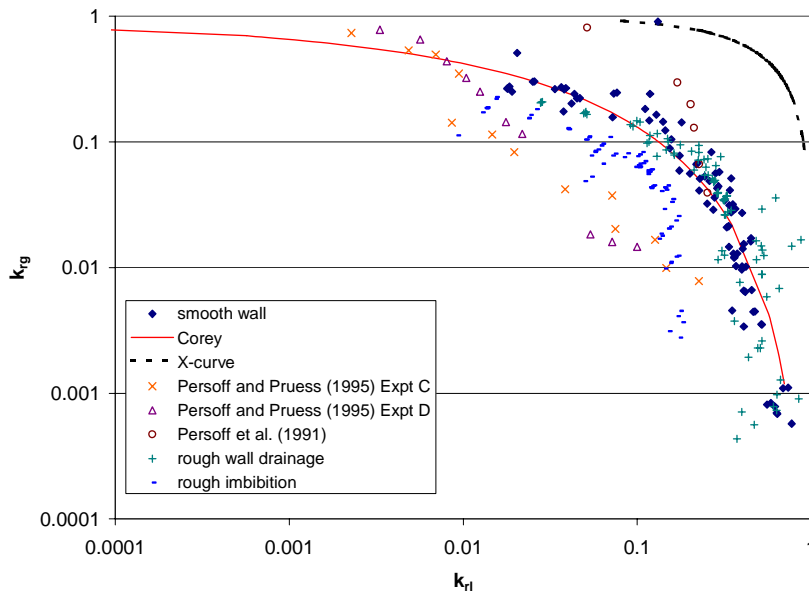


Figure 6.36: Comparison of relative permeability data with previous work on rough walled fractures.

## **6.5 CONCLUSIONS AND RECOMMENDATIONS**

The experiments and analysis presented in this work have led to the following conclusions:

1. Two-phase flow through smooth and rough parallel plate fractures is characterized by each phase establishing localized continuous flow paths. The stability of these flow paths is dependent on the flow rate ratio of the phases. A phase flow path undergoes constant cycles of breakage and reformation as certain points are blocked and unblocked by the other phase. The breaking and reforming of phase paths cause pressure, flow rate and saturation fluctuations even at constant input conditions. This reveals the unsteady nature of flow through fractures.
2. The imbibition process through the rough-walled fracture also undergoes wave like flow similar to flow in pipes at high gas-water ratio. Other than this, flows through the smooth- and the rough-walled fracture are similar to flow in porous media where a phase moves by establishing continuous channels. The flow mechanism of having discontinuous moving flow structures as bubbles or "islands" carried along by another continuous phase was not observed in any of the experiments.
3. Two-phase flow through smooth- and rough-walled fractures can be modeled adequately by a porous medium approach. In this approach, Darcy's law governs flow and phase interference is represented by the relative permeability variable. The resulting relative permeability curve from experimental data shows a clear relationship between relative permeability and phase saturation. The experimental relative permeability values follow the shape of Corey curves and can be fitted to with reasonable accuracy by the Honarpour expression.
4. There is considerable phase interference in flow through fractures. This is deduced from the observation that the sum of the gas and liquid relative permeability for all experiments was less than unity.
5. The equivalent homogenous single-phase approach did not give satisfactory representation of flow through fractures. The graphs of experimentally derived friction factor with the modified Reynold's number do not reveal distinctive linear relationships. This model leads to inadequate pressure drop prediction.

The apparatus and methodology used in this study proved to be an effective means of investigating flow through fractures. However, improvement is needed in ensuring control of fracture aperture i.e. preventing the glass plate from being lifted by the flowing fluids. The method for saturation measurement is dependable when picture quality is good and when distinct boundaries of the phases can be seen. It is recommended to experiment with techniques for enhancing picture color contrast. This would improve the program's accuracy in differentiating phases. This will be useful for cases when small

isolated phases are dispersed throughout such as the case in imbibition for the rough-walled fracture.

It is recommended that further experiments with smooth-walled fractures be done this time with greater certainty as to the absolute permeability of the fracture. This is to establish the magnitude of relative permeability in the smooth-walled fracture. It is also recommended that experiments be conducted to investigate other variables that were not included in this study, such as effect of aperture, viscosity, gravity, degree of roughness etc.



## **7. REFERENCES**

- Amyx, J. W., Bass, D.M, and Whiting, R.L. *Petroleum Reservoir Engineering Physical Properties*, McGraw-Hill Book Co.,New York, 1960, pp 199-200.
- Ambusso, W.J., “Experimental Determination of Steam-Water Relative Permeability Relations,” MS thesis, Stanford University, Stanford, California (1996).
- Anderson, A.W., and Gast, A.P.: "*Physical Chemistry of Surfaces*," 6<sup>th</sup> Edition, A Wiley-Interscience Publication, John Wiley & Sons, New York, 1997.
- Aronofsky, J.S., Masse, L., and Natanson, S.G.: “A Model for the Mechanism of Oil Recovery from the Porous Matrix Due to Water Invasion in Fractured Reservoirs,” *Trans. AIME* (1958) **213**, 17-19.
- Clossman, P.J., and Vinegar, J.J., “Relative Permeability to Steam and Water at Residual Oil in Natural Cores; CT Scan Saturation,” SPE paper 174449.
- Corey, A.T., “The Interrelations Between Gas and Oil Relative Permeabilities,” *Producers Monthly* Vol. 19 (1954), pp 38-41.
- Fatt, I.: "The Network model of Porous Media I," *Petroleum Transactions*, AIME, Vol. 207, 141-159, 1956.
- Fourar, M. and Bories, S.: "Experimental Study of Air-Water Two-Phase Flow Through A Fracture (Narrow Channel)," *Int. J. Multiphase Flow* Vol. 21, No. 4, Toulouse, France (1995) pp. 621-637.
- Fourar, M., Bories., Lenormand, R., and Persoff, P.: "Two-Phase Flow in Smooth and Rough Fractures: Measurement and Correlation by Porous-Medium and Pipe Flow Models," *Water Resources Research* Vol. 29 No. 11. November 1993, pp. 3699-3708.
- Handy, L.L.: “Determination of Effective Capillary Pressures for Porous Media from Imbibition Data,” *Petroleum Transactions AIME*, Vol. 219, 1960, 75-80.
- Hanselman, D. and Littlefield, B.: *Mastering Matlab 5 A Comprehensive Tutorial and Reference*, Prentice-Hall, Inc.,New Jersey, 1998.
- Horne, R.N., Ramey, H.J., Jr., Shang, S., Correa, A., and Hornbrook, J.: "The Effects of Adsorption and Desorption on Production and Reinjection in Vapor-Dominated Geothermal Fields," *Proc. of the World Geothermal Congress*, 1995, Florence, Italy, May, 1995, 1973-1977.
- Horne, R.H., Satik, C., Mahiya, G., Li, K., Ambusso, W., Tovar, R., Wang, C., and Nassori, H.: "Steam-Water Relative Permeability," *Proc. of the World Geothermal Congress 2000*, Kyushu-Tohoku, Japan, May 28-June 10, 2000.
- Kazemi, H., Gilman, J.R., and El-Sharkaway, A.M.: “Analytical and Numerical Solution of Oil Recovery from Fractured Reservoirs Using Empirical Transfer Functions,” paper SPE 19849, presented at the SPE 64<sup>th</sup> Annual Technical Conference and Exhibition, San Antonio, TX, October 8-11, 1989.

- Kneafsy, T. J. and Pruess, K.,: "Laboratory Experiments on Heat-Driven Two-Phase Flows in Natural and Artificial Rock Fractures," *Water Resources Research* Vol. 34, No. 12, December 1998, pp. 3349-3367.
- Li, K., and Horne, R.N., "Accurate Measurement of Steam Flow Properties," *GRC Transactions* 23 (1999).
- Li, K., and Horne R.N.: "Steam-Water Capillary Pressure in Geothermal Systems," *Proc. of 25<sup>th</sup> Workshop on Geothermal Engineering*, Stanford, CA, Jan. 24-26, 2000.
- Li, K., and Horne, R.N.: "An Experimental Method for Evaluating Water Injection into Geothermal Reservoirs," presented at the GRC 2000 annual meeting, September 24-27, 2000, San Francisco, USA; *GRC Trans. V. 24*.
- Li, K., and Horne R.N.: "Differences between Steam-Water and Air-Water Capillary Pressures," *Proc. of 26<sup>th</sup> Workshop on Geothermal Engineering*, Stanford, CA, Jan. 29-31, 2001.
- Li, K., and Horne, R. N.: "Characterization of Spontaneous Water Imbibition into Gas-Saturated Rocks," accepted to be published in *SPEJ* (2001).
- Lockhart, R. W. and Martinelli, R.C.: "Proposed Correction of Data for Isothermal two-phase component flow in pipes," *Chem. Eng. Prog.*, Vol. 45, No. 39, 1949.
- Ma, S., Morrow, N.R., and Zhang, X.: "Generalized Scaling of Spontaneous Imbibition Data for Strongly Water-Wet Systems," paper 95-138, presented at the 6<sup>th</sup> Petroleum Conference of the South Saskatchewan Section, the Petroleum Society of CIM, held in Regina, Saskatchewan, Canada, October 16-18, 1995.
- Mahiya, G., "Experimental Measurement Of Steam-Water Relative Permeability," MS thesis, Stanford University, Stanford, California (1999).
- Mattax, C.C., and Kyte, J.R.: "Imbibition Oil Recovery from Fractured, Water-Drive Reservoir," *SPEJ* (June 1962), 177-184.
- Persoff, P., and Hulen, J.B.: "Hydrologic Characterization of Four Cores from the Geysers Coring Project," *Proc. of 21<sup>st</sup> Workshop on Geothermal Engineering*, Stanford, CA, 1996.
- Satik, C., "A Measurement of Steam-Water Relative Permeability," *Proceedings of 23<sup>rd</sup> Workshop on Geothermal Reservoir Engineering*, Stanford University, Stanford, California (1998).
- Sta. Maria, R.B., and Pingol, A.S.: "Simulation the effects of Adsorption and Capillary Forces in Geothermal Reservoirs," *Proc. of 21<sup>st</sup> Workshop on Geothermal Engineering*, Stanford, CA, 1996.
- Zhang, X., Morrow, N.R., and Ma, S.: "Experimental Verification of a Modified Scaling Group for Spontaneous Imbibition," *SPEJ* (November 1996), 280-285.

- Pan, X., Wong, R.C., and Maini, B.B.: Steady State Two-Phase Flow in a Smooth Parallel Fracture, presented at the 47<sup>th</sup> Annual Technical Meeting of the Petroleum Society in Calgary, Alberta, Canada, June 10-12, 1996.
- Persoff, P. K., Pruess, K. and Myer, L.: "Two-Phase Flow Visualization and Relative Permeability Measurement in Transparent Replicas of Rough-Walled Rock Fractures," Proc. 16<sup>th</sup> Workshop on Geothermal Reservoir Engineering, Stanford University, Stanford, California, January 23-25, 1991
- Persoff, P., and Pruess, K.: "Two-Phase Flow Visualization and Relative Permeability Measurement in Natural Rough-Walled Rock Fractures," Water Resources Research Vol. 31, No. 5, May, 1995, pp. 1175-1186.
- Pruess, K., and Tsang, Y. W.: "On Two-Phase Relative Permeability and Capillary Pressure of Rough-Walled Rock Fractures," Water Resources Research Vol. 26 No. 9, September 1990, pp 1915-1926.
- Scheidegger, A.E. *The Physics of Flow Through Porous Media*, 3<sup>rd</sup> ed., University of Toronto, Toronto. 1974.
- Su, G. W., Geller, J. T., Pruess, K. and Wen, F.:. " Experimental Studies of Water Seepage and Intermittent Flow in Unsaturated, Rough-Walled Fractures," Water Resources Research, Vol. 35, No. 4, April 1999, pp. 1019-1037.